

1996

Analysis of limestone calcination and sulfation using transient gas analysis

Theodore Donald Thiede
Iowa State University

Follow this and additional works at: <https://lib.dr.iastate.edu/rtd>

 Part of the [Chemical Engineering Commons](#), and the [Mechanical Engineering Commons](#)

Recommended Citation

Thiede, Theodore Donald, "Analysis of limestone calcination and sulfation using transient gas analysis " (1996). *Retrospective Theses and Dissertations*. 11495.
<https://lib.dr.iastate.edu/rtd/11495>

This Dissertation is brought to you for free and open access by the Iowa State University Capstones, Theses and Dissertations at Iowa State University Digital Repository. It has been accepted for inclusion in Retrospective Theses and Dissertations by an authorized administrator of Iowa State University Digital Repository. For more information, please contact digirep@iastate.edu.

INFORMATION TO USERS

This manuscript has been reproduced from the microfilm master. UMI films the text directly from the original or copy submitted. Thus, some thesis and dissertation copies are in typewriter face, while others may be from any type of computer printer.

The quality of this reproduction is dependent upon the quality of the copy submitted. Broken or indistinct print, colored or poor quality illustrations and photographs, print bleedthrough, substandard margins, and improper alignment can adversely affect reproduction.

In the unlikely event that the author did not send UMI a complete manuscript and there are missing pages, these will be noted. Also, if unauthorized copyright material had to be removed, a note will indicate the deletion.

Oversize materials (e.g., maps, drawings, charts) are reproduced by sectioning the original, beginning at the upper left-hand corner and continuing from left to right in equal sections with small overlaps. Each original is also photographed in one exposure and is included in reduced form at the back of the book.

Photographs included in the original manuscript have been reproduced xerographically in this copy. Higher quality 6" x 9" black and white photographic prints are available for any photographs or illustrations appearing in this copy for an additional charge. Contact UMI directly to order.

UMI

A Bell & Howell Information Company
300 North Zeeb Road, Ann Arbor, MI 48106-1346 USA
313/761-4700 800/521-0600

Analysis of limestone calcination and sulfation using transient gas analysis

by

Theodore Donald Thiede

A dissertation submitted to the graduate faculty
in partial fulfillment of the requirements for the degree of
DOCTOR OF PHILOSOPHY

Department: Mechanical Engineering

Major: Mechanical Engineering

Major Professor: Robert C. Brown

Iowa State University

Ames, Iowa

1996

Copyright © Theodore Donald Thiede, 1996. All rights reserved.

UMI Number: 9635361

Copyright 1996 by
Thiede, Theodore Donald

All rights reserved.

UMI Microform 9635361
Copyright 1996, by UMI Company. All rights reserved.

This microform edition is protected against unauthorized
copying under Title 17, United States Code.

UMI
300 North Zeeb Road
Ann Arbor, MI 48103

**Graduate College
Iowa State University**

**This is to certify that the Doctoral dissertation of
Theodore Donald Thiede
has met the dissertation requirements of Iowa State University**

Signature was redacted for privacy.

Major Professor

Signature was redacted for privacy.

For the Major Department

Signature was redacted for privacy.

For the Graduate College

DEDICATION

This work is dedicated to the Lord in thanksgiving for all of the guidance, strength, wisdom and knowledge that He supplies. It is also dedicated to my wife, Diane. She has stood by me during this endeavor, and all too often has had to wait patiently for me when I could not be there for her. While I enjoyed the excitement of reaching for my educational goals, she had the hard job of tending to the needs and wants of three children under four years old. From this work I will earn a few initials after my name. She on the other hand, will continue to wait for her reward: the words "Well done thou good and faithful servant" when she finishes her course in this life.

TABLE OF CONTENTS

LIST OF FIGURES	vi
LIST OF TABLES	ix
NOMENCLATURE	x
ACKNOWLEDGMENTS	xv
ABSTRACT	xvi
1. INTRODUCTION	1
2. BACKGROUND	4
2.1 SO ₂ Sorbent Characteristics	4
2.2 Calcination	6
2.3 Sulfation	9
3. MODELING	14
3.1 Overview of Model Types	14
3.2 Modeling of Calcination	17
3.3 Modeling of Sulfation	29
4. EXPERIMENTAL APPARATUS	46
4.1 Laboratory Equipment	46
4.2 Laboratory Instrumentation	48
4.3 Power Plant Equipment	50
4.4 Power Plant Instrumentation	52
4.5 Particle Analysis Equipment	52
5. MATERIALS AND METHODS	54
5.1 Characteristics of Tested Sorbents	54
5.2 Test Procedures	57
5.3 Transient Gas Analysis	60
5.4 Full Scale Boiler Testing	68
5.4 Particle Analysis	68
6. RESULTS AND DISCUSSION	70
6.1 Transient Gas Analysis of Calcination	70
6.2 Particle Analysis of Calcined Particles	86
6.3 Transient Gas Analysis of Sulfation	93
6.4 Particle Analysis of Sulfated Particles	122

6.5	Transient Gas Analysis of Sulfation in Full-Scale Boiler	127
6.6	Particle Analysis of Particles from Full-Scale Boiler	130
7.	CONCLUSIONS	133
7.1	Calcination	133
7.2	Sulfation	134
7.3	Full Scale Boiler Testing	136
7.4	Suggestions for Future Tests	136
	APPENDIX: PROGRAM CODE	138
	REFERENCES	149

LIST OF FIGURES

Figure 3.1	Overview of models used in sorbent reactions	15
Figure 3.2	Schematic of shrinking grain core model for sulfation	32
Figure 4.1	Schematic of laboratory combustor and instrumentation.	47
Figure 4.2	Schematic of boiler #2 at ISU power plant [40]	51
Figure 5.1	Size distribution of power plant limestone.	55
Figure 5.2	Internal structure of Gilmore City formation limestone	56
Figure 5.3	CO ₂ transient.	61
Figure 5.4	SO ₂ transient.	62
Figure 6.1	Comparison of calcination model to transients	71
Figure 6.2	Resistances to reaction for 0.55 mm diameter particle	72
Figure 6.3	Resistances to reaction for 2.58 mm diameter particle	73
Figure 6.4	Transient data changed into the form of Eqn. (3.18) for evaluation of τ_c	74
Figure 6.5	Log plot of calcination time constant vs. particle diameter	75
Figure 6.6	Calcination activation energies for various particle sizes	79
Figure 6.7	Extent of calcination at various temperatures for four particle sizes	83
Figure 6.8	Calcination transients for two other limestones	85
Figure 6.9	SEM photograph of unreacted limestone	88
Figure 6.10	SEM photograph of 2.58 mm limestone particle extracted after 2 minutes of reaction	89
Figure 6.11	Region A of particle in Fig. 6.10	90
Figure 6.12	Region B of particle in Fig. 6.10	90

Figure 6.13	Region C of particle in Fig. 6.10	91
Figure 6.14	Region D of particle in Fig. 6.10	91
Figure 6.15	Comparison of shrinking particle core model vs laboratory SO ₂	95
Figure 6.16	Resistances to sulfation for 0.655 mm diameter particle	99
Figure 6.17	Resistances to sulfation for 1.85 mm diameter particle	100
Figure 6.18	Time constant chart to evaluate chemistry control	102
Figure 6.19	Initial concentration chart used to evaluate film mass transfer control	104
Figure 6.20	Time constant chart to evaluate pore diffusion control	105
Figure 6.21	Time constant chart to evaluate pore plugging control	106
Figure 6.22	Calcium utilization for a range of 16 different particle sizes	108
Figure 6.23	Plot of calcination time constant versus particle diameter	109
Figure 6.24	Calcium utilization as a function of temperature for four particle sizes	110
Figure 6.25	Determination of activation energy for sulfation for four particle sizes	111
Figure 6.26	Calcium utilization as function of temperature for batch tests with lime and limestone	114
Figure 6.27	Determination of activation energy for sulfation comparing batch additions of lime vs. lime	115
Figure 6.28	Predicted CO ₂ flux from various sized particles based on CO ₂ transients	116
Figure 6.29	Normalized SO ₂ transients for lime and limestone	116
Figure 6.30	Comparison of normalized SO ₂ transient for washed and unwashed limestone batch additions	118
Figure 6.31	Transient SO ₂ response for varying concentrations of O ₂	120
Figure 6.32	Comparison of normalized SO ₂ transients for three limestones	121

Figure 6.33	SEM maps of sulfation at various times in the reaction	124
Figure 6.34	Particle linescans at various stages of reaction	125
Figure 6.35	Comparison of transient gas analysis with SEM linescan analysis	126
Figure 6.36	SO ₂ emissions during limestone batch test	127
Figure 6.37	Comparison of laboratory and power plant sulfation transients	128
Figure 6.38	Log-linear time constant chart comparing lab and full scale combustors	129
Figure 6.39	SEM component maps of power plant bottom ash showing sulfur rims	131

LIST OF TABLES

Table 4.1	Gas analyzer equipment and associated accuracies	49
Table 5.1	Chemical analysis of limestones used	54
Table 5.2	Extent of calcination measured for different lengths of time for five runs at the same conditions.	66
Table 6.1	Particle size dependence of τ_c at various temperatures	76
Table 6.2	Calcination activation energies for various particle sizes	79
Table 6.3	Calcination time constant for various background CO ₂ concentrations	84
Table 6.4	Effect of superficial velocity on calcination time constant and extent of calcination	84
Table 6.5	Time constants and reaction extents for two limestone types with various particle sizes	86
Table 6.6	Parameters used in model for Figure 6.15	95
Table 6.7	Time constants and reaction extents for three limestone types with various particle sizes	122
Table 6.8	XRF chemical analysis of ISU boiler ash	132

NOMENCLATURE

a_{cc}	surface area of unreacted CaCO_3 core (m^2)
a_{gc}	surface area of unreacted CaO grain core (m^2)
a_p	surface area of particle (m^2)
a_{sc}	surface area of unreacted CaO particle core (m^2)
b	slope
c_{1c}	constant #1 for calcination = $\{[\text{CO}_2]_E - [\text{CO}_2]_i\} M_{\text{CaCO}_3} / f_{\text{CaCO}_3} \rho_{\text{LS}}$
c_{1s}	constant #1 for sulfation = $[\text{SO}_2]_i M_{\text{CaO}} / f_{\text{CaCO}_3} \rho_{\text{CaO}}$
c_2	constant #2 = $S m / \rho_{\text{LS}} Q$
C_A	concentration of species A (mol/m^3)
C_{Ag}	concentration of species A in reactor (mol/m^3)
C_{Ao}	initial concentration of species A (mol/m^3)
$[\text{CO}_2]$	CO_2 concentration as a function of radial position in the particle (mol/m^3)
$[\text{CO}_2]_E$	equilibrium CO_2 concentration for reversible Eqn. (2.1)
$[\text{CO}_2]_i$	CO_2 concentration at inlet (mol/m^3)
$[\text{CO}_2]_o$	CO_2 concentration, initial (mol/m^3)
$[\text{CO}_2]_R$	CO_2 concentration in reactor (mol/m^3)
$[\text{CO}_2]_s$	CO_2 concentration at particle surface (mol/m^3)
D_{ec}	effective diffusivity of CO_2 in particle pores (m^2/s)
D_{es}	effective diffusivity of SO_2 (m^2/s)
D_{eso}	initial effective diffusivity of SO_2 (m^2/s)
ΔH	heat of reaction (kcal/mol)
d_p	particle diameter, (m)
D_{pl}	product layer diffusivity (m^2/s)

\mathcal{D}_r	reactant diffusivity in the reaction zone (m^2/s)
E_a	activation energy
f_{CaCO_3}	mass fraction of CaCO_3 in limestone
f_{CaO}	mass fraction of CaO in limestone
h_c	film mass transfer coefficient for CO_2 diffusion (m/s)
h_T	film heat transfer coefficient ($\text{kcal}/\text{m}^2\cdot\text{K}$)
K	dimensionless reaction rate coefficient = $k_s S_o/Q$
k^*	reaction rate coefficient for carbonation reaction ($\text{mol}/\text{N}\cdot\text{m}\cdot\text{s}$)
k_c	calcination reaction rate coefficient ($\text{m}^3/\text{mol}\cdot\text{s}$)
k_c^*	thermal conductivity of CaO ($\text{kcal}/\text{m}^2\cdot\text{K}$)
k_d	diffusivity decay rate constant (s^{-1})
k_s	sulfation reaction rate coefficient (m/s)
k_v	volumetric reaction rate ($\text{m}^3/\text{mol}\cdot\text{s}$)
L	dimensionless length (m) = $t/2$ for flat plates, r for cylinders and spheres
M_{CaCO_3}	molecular weight of CaCO_3 (g/mol)
M_L	molecular weight of limestone (g/mol)
m_{LS}	mass of limestone batch (g)
n_p	number of particles per limestone batch
$n_{1,2}$	number of data points on regression line
P	total pressure (Atm)
p_E	equilibrium partial pressure for calcination/carbonation reaction (Atm)
p_R	instantaneous partial pressure of CO_2 (Atm)
Q	volumetric flow rate through the combustor (m^3/s)
r_{cc}	radius of unreacted CaCO_3 core (m)
$R_{\text{chemical reaction}}$	resistance to reaction due to chemical reaction
Re_p	particle Reynolds number = $U_o d_p/\nu$

$R_{\text{film diffusion}}$	resistance to reaction due to film diffusion
r_p	particle radius (m)
$R_{\text{pore diffusion}}$	resistance to reaction due to pore diffusion
r_{sc}	radius of unreacted CaO core (m)
S	external surface area of particles in the batch (m^2)
S	shape factor = 1 for flat plates, 2 for cylinders, 3 for spheres
Sc	Schmidt number = v/\mathcal{D}
S_b	standard deviation of the slope
S_{bc}	combined slope standard deviation
S_{bd}	standard deviation for the difference of the slopes
S_g	material specific surface area (m^2/g)
Sh	Sherwood number = hd_p/\mathcal{D}
S_o	initial external surface area of particles in the batch (m^2)
$S_{y x}$	standard error of y on x
$[\text{SO}_2]_{\text{gc}}$	SO_2 concentration at the CaO grain core (mol/m^3)
$[\text{SO}_2]_i$	combustor inlet SO_2 concentration (mol/m^3)
$[\text{SO}_2]_o$	initial SO_2 concentration in the reactor (mol/m^3)
$[\text{SO}_2]_R$	SO_2 concentration in and leaving the combustor (mol/m^3)
$[\text{SO}_2]_s$	SO_2 concentration at the particle surface (mol/m^3)
$[\text{SO}_2]_{\text{sc}}$	SO_2 concentration at the particle CaO core surface (mol/m^3)
t	reaction time (s), t distribution value
T_{bed}	bed temperature (K)
t_c	time to complete calcination (s)
t_{pl}	product layer thickness (m)
\bar{x}	mean of x values for slope statistical analysis
U_o	bed superficial velocity (m/s)

V_b	volume of the bed (m^3)
V_c	volume of the unreacted $CaCO_3$ core (m^3)
V_{cc}	molar volume of $CaCO_3$ (m^3/mol)
V_F	volume of the SO_2 mass transfer film (m^3)
V_p	volume of the particle (m^3)
X_c	extent of calcination ($100 \cdot mol\ CO_2\ released / mol\ Ca, \%$)
X_s	extent of sulfation ($100 \cdot mol\ SO_2\ absorbed / mol\ Ca, \%$)
y_i	constant mole fraction of CO_2

Greek letters

β	Ca/S ratio
ε_b	bed voidage, volume fluid in bed/ volume of bed
ε_i	residual value
ε_s	effectiveness factor for sulfation
ϕ_r	Thiele modulus in the reaction zone
ϕ_s	product layer diffusion Thiele modulus for sulfation
η_s	fractional reduction in SO_2 emissions vs. no limestone addition
ν	kinematic viscosity (m^2/s)
ρ_{CaO}	density of lime (g/m^3)
ρ_{ls}	density of limestone (g/m^3)
τ_c	calcination time constant (s)
τ_{cb}	calcination time constant for bulk mass transfer-controlled calcination (s)
τ_{cbd}	calcination time constant for bulk mass transfer-controlled calcination with pore diffusion as a secondary resistance (s)
τ_{cbk}	calcination time constant for bulk mass transfer-controlled calcination with chemistry as a secondary resistance (s)

τ_{cd}	calcination time constant for pore diffusion-controlled calcination (s)
τ_{ch}	calcination time constant for film diffusion-controlled calcination (s)
τ_{ck}	calcination time constant for chemistry-controlled calcination (s)
τ_e	elutriation time constant (s)
τ_i	instrument time constant (s)
τ_p	pore plugging time constant (s)
τ_s	sulfation time constant (s)
τ_{sb}	sulfation time constant for bulk mass transfer-controlled sulfation (s)
τ_{sbd}	sulfation time constant for bulk mass transfer-controlled sulfation with pore diffusion as a secondary resistance (s)
τ_{sbk}	sulfation time constant for bulk mass transfer-controlled sulfation with chemistry as a secondary resistance (s)
τ_{sd}	sulfation time constant for pore diffusion-controlled sulfation (s)
τ_{sh}	sulfation time constant for film diffusion-controlled sulfation (s)
τ_{sk}	sulfation time constant for chemistry-controlled sulfation (s)
ξ_c	dimensionless radius of CaCO_3 core during calcination = r_{cc}/r_p
ξ_s	dimensionless radius of CaO core during sulfation = r_{sc}/r_p

ACKNOWLEDGMENTS

I want to thank Dr. Robert Brown for the opportunity to conduct this research. He gave me great freedom to investigate, but also was able to give me consistent guidance when it was needed. He and his research group have made this endeavor an extremely enjoyable one for me.

Invaluable help with particle analysis was given to me from Dr. M. Robert Dawson and Dr. Warren Straszheim. Their knowledge of geochemistry and microscopy were immensely appreciated, as was the extra time they spent assisting me on this project.

Funding for this work was partially provided by The U. S. Department of Energy through Cooperative Agreement N. DE-FC21-91MC28081

ABSTRACT

This study examined the fundamental reaction dynamics associated with calcination and sulfation of limestone particles in fluidized bed combustors. Although this subject has been extensively treated in the literature, investigations to date have been primarily conducted in small laboratory reactors that do not well simulate combustor conditions. A review of the literature shows disagreement as to the controlling mechanisms for the calcination and sulfation reactions. In this investigation, experiments were conducted both on laboratory-scale and full-scale fluidized bed combustors (FBC's).

Transient gas analysis of combustor emissions was used to investigate calcination and sulfation reactions in FBC's. Measurements of carbon dioxide and sulfur dioxide were made continuously after batch additions of limestone for many different operating conditions. Experimental variables included bed temperature, air and fuel flow rates, oxygen and carbon dioxide concentrations, batch size and particle size. Time constants for calcination and sulfation which characterized the reactions were defined. Integration of CO₂ and SO₂ transients gave the extents of calcination and sulfation.

From this study it was revealed that the calcination reaction is controlled by the chemical reaction rate. This result was deduced from the particle size dependence and observed activation energy of the calcination reaction rate. Intra-particle diffusion also influenced the calcination reaction rate at high temperatures in large particles. The sulfation reaction appeared to be controlled by film and bulk mass transfer at early times in the laboratory reactor. At later times pore diffusion and pore-plugging controlled the reaction for the relatively non-porous limestones studied. The type of limestone and the conditions of calcination strongly determined the rate and extent of sulfation.

Particle analysis was done for comparison to transient gas analysis results. Calcination appeared to take place by a shrinking particle core mechanism. Scanning

electron microscopy (SEM) revealed a calcined outer layer for particles extracted during the middle of the CO₂ transient. Evidence of structural changes in the calcine as the reaction proceeded inward was observed. Sulfated particles demonstrated an outer layer that increased in thickness and concentration over the course of the reaction.

1. INTRODUCTION

Fluidized bed combustion (FBC) is a rapidly growing technology in the power industry. Although this technology has been available for many years, recent interest has been sparked by requirements to reduce sulfur dioxide (SO_2) emissions from coal burning power plants. To remove SO_2 emitted from conventional coal burning power plants, huge investments must be made for flue gas desulfurization systems. These systems can cost as much as 20% of the capital cost for new coal-burning power plants [1]. The appealing feature of FBC boilers is in situ removal of SO_2 , without the requirement of this expensive equipment. The high degree of gas-solid contacting that occurs in fluidized beds allows them to be extremely effective at removing this gaseous pollutant. This study focuses on the reactions involved in removing SO_2 from combustion gases in fluidized bed combustors.

Two regimes of fluidization are significant in this study. Bubbling bed fluidization occurs when air is passed upward through a suspended bed of fine particles at velocities that are high enough to suspend the particles, but not so high as to cause elutriation of particles from the bed. In the second regime, circulation fluidization, air flows are high enough to cause continuous elutriation of the particles from the combustion region. Particles are collected by cyclone separators and reintroduced to the bottom of the bed. Because of the higher combustion efficiency possible with circulating FBC, these combustors are the primary type of fluidized bed found in industrial applications. Bubbling FBC reactors are also useful in industrial applications where a uniform temperature is desired. In this investigation, a laboratory bubbling bed is used to investigate limestone reactions. The condition of fluidization in this smaller combustor is similar to the turbulent phase found at the bottom of circulating FBC boilers.

Sulfur dioxide is removed from combustion product gases in coal-burning fluidized beds by the continuous addition of sorbent particles. The most common sorbents used in

FBC are limestones and dolomites, because they are inexpensive and readily available. These sorbents are made up primarily of calcium carbonate (CaCO_3). At combustion temperatures, CaCO_3 rapidly undergoes the process of calcination, in which carbon dioxide (CO_2) is released from the limestone leaving calcium oxide (CaO). The CaO formed is known as calcine or lime. Calcine is characterized by high porosity and large surface areas, which increases its ability to react with SO_2 . The reaction between CaO and SO_2 , referred to as sulfation, involves an increase in molar volume, which causes the plugging of particle pores and limits the extent of reaction that can occur.

The sulfation of limestone has been the subject of extensive study. Much of this research has been performed under well-controlled laboratory conditions that do not necessarily simulate conditions within actual combustors. Tests have been performed on relatively small amounts of limestone in a variety of reactor types. This research has led to several models for these reactions. The models consider the effects of several characteristics of sorbents. Other research, performed on operating FBC boilers, has provided empirical information and overall operating characteristics for full-scale units. Models developed from these studies have a more restricted applicability and tell much less about the limestone characteristics.

The objective of this investigation is to develop methodology for characterizing sorbents from transient emissions from fluidized bed combustors. The scope of this study ranges from the laboratory scale to the full scale. The laboratory FBC analysis diverges from previous laboratory investigations in the literature by being performed under realistic combustion conditions. From this study, a model is proposed to relate the experimental transients to the transport and reaction characteristics of the limestone. Simplification of this model is possible, which leads to analytical methods appropriate to transient experiments. Experiments done in this phase develop the analytical techniques to determine controlling mechanisms. Particle analysis of samples removed after a variety of reaction is

accomplished to compare particle analysis results to the transient emissions data. Full scale tests at the Iowa State University (ISU) power plant are designed to demonstrate the ability to apply laboratory results to an operating boiler.

This investigation begins with a discussion of fundamental mechanisms of calcination and sulfation. This is followed by a review of existing models for both calcination and sulfation. In this section a relatively simple model that explains sorbent reactions is developed. Chapters four and five describe the equipment used during this investigation, the characteristics of the limestones tested, and the methods used for testing and analysis. The results of the experiments are given in chapter six along with comparisons to previous studies. Chapter seven presents conclusions about the sorbent reactions and the analytical methods needed to further the study of limestone calcination and sulfation in boilers.

2. BACKGROUND

2.1 SO₂ Sorbent Characteristics

Limestones and dolomites are naturally occurring sedimentary rocks found throughout the world. These stones generally have their origin in shallow seas where biogenic calcium was deposited in layers over long periods of time. The age of a particular vein of limestone has some impact on its physical characteristics. In their examination of 23 varieties of limestone, Dam-Johansen and Ostergaard [2] were able to group limestones into three distinct categories. Limestones of young geologic age, which constituted the first category, exhibited an open, highly porous texture. Chalk, an example of this type of limestone, exhibits a high degree of purity. Chalk was formed on the floors of broad shallow continental seas at the end of the Cretaceous geological period, which extended from 65 to 130 million years ago [3]. The second category consisted of limestones of an intermediate geological age that have coarse grains and less porosity. The old limestones of the final category are compact and have a non-porous texture.

In their study, Dam-Johansen and Ostergaard found that the porous limestones were much more reactive than the older compact limestones. Some of the older limestones they tested had slightly higher calcined surface areas than chalks, which exhibited higher reactivity [2]. This seems to indicate that pore size may be of greater significance in limestone sulfation than surface area.

Carbonate rocks commonly consist of three minerals: calcite, aragonite and dolomite. Calcite and aragonite are both forms of CaCO₃, but they have different crystal structures and solubilities. Dolomite, CaMg(CO₃)₂, consists of calcium and magnesium in approximately equal proportions. Calcined dolomite usually retains porosity better than calcined calcite. Since SO₂ reacts only at the CaO sites and not at the MgO sites, the reaction is less inhibited by the large molar volume change associated with sulfation.

Greater porosity in dolomite allows SO_2 to diffuse farther into the dolomite particle without plugging pores. Variations of the proportions of dolomite and calcite lead to a variety of carbonate rocks, such as dolomite limestone and calcitic dolomite [4].

Borgwardt and Harvey [5] performed analyses on a broad spectrum of carbonate rocks. SO_2 reactivity in the dolomites and calcites that they tested showed a strong dependence on surface area and pore sizes in the calcine. They tested magnesite, MgCO_3 , and found that it showed virtually no SO_2 reactivity, although it had a significantly greater calcined surface area and equivalent pore volume when compared to the calcines. Marble, which is metamorphic CaCO_3 , showed little reactivity due to a small calcine surface area. Aragonite had the lowest SO_2 reactivity of the eleven stones tested with the exceptions of magnesite and marble. Although aragonite had the largest mean pore diameter, it had the smallest calcined pore volume and surface area [5]. One conclusion from this work is that mean pore diameter, surface area, and pore volume are all important parameters. A small value for any one of these parameters can cause reduced sorbent performance.

The chemical make-up of limestone also is a factor in its ability to react with SO_2 . Dolomites have been shown to allow more CaO to react because the magnesium content causes an increase in surface area. The CaO component in dolomite tends to crystallize independently from MgO during calcination. The small grain size of CaO then results in a large CaO surface area. Increased pore volume upon calcination compensates for the decrease in pore volume that occurs when CaO reacts to form CaSO_4 [5]. This increase in reactivity in dolomites and dolomitic limestones due to magnesium content was also found in the investigation by Mulligan *et al.* [6]. Carello and Vilela [7] studied five Brazilian limestone varieties and did not find that magnesium content aided in the sulfation process. Their tests differed from others in the literature in that they sulfated calcines in pure SO_2 rather than in a simulated combustion atmosphere.

In their study of thirteen limestones, Mulligan *et al.* [6] found that limestones with

high silica content produce high surface area calcines, which in turn improves their sulfation efficiency. Dam-Johansen and Ostergaard [2] found that ferric oxide adversely affects sulfur dioxide capacity, but other researchers [8, 9] have found that in some cases ferric oxide content improves sorbent performance.

2.2 Calcination

Although much has been written about the calcination reaction, there is significant variation in the data reported for reaction kinetics and thermodynamics. In the calcination of limestone, the sorbent releases CO₂ in an endothermic reaction:



The carbonation reaction, which is the reverse of Eqn. (2.1), is also significant at FBC operating temperatures, resulting in a reaction rate that includes the effects of the equilibrium partial pressure. The resulting calcine will vary considerably based on differences in the structure of the parent limestone, the types and magnitude of impurities present, the thermodynamic conditions, and the concentration of gases in the reactor. The variety of test conditions employed by researchers also influences the rate-controlling process reported in their studies.

Since the porosity of uncalcined limestones is negligible, the calcination reaction greatly affects the subsequent sulfation reaction. The degree of calcination and the properties of the CaO matrix determine the ability of the calcine to remove SO₂. High concentrations of CO₂ in the reactor may decrease the degree of calcination in the sorbent due to the reverse reaction of Eqn. (2.1). Additionally, calcium sulfate (CaSO₄) deposits on the outer surface of the limestone particle may restrict the escape of CO₂ from the particle, and thus limit the extent of calcination.

Some researchers [10, 11] have concluded that calcination can be modeled as a shrinking particle core model, an idea that is further explored in chapter three. According to Khraisha and Dugwell [10], the overall reaction process using this model includes at least five steps:

- 1) heat transfer from the surrounding atmosphere to the particle surface
- 2) heat transfer from the particle surface to the reaction site
- 3) chemical reaction at the reaction site
- 4) diffusion of CO₂ from the reaction site through an ash layer to the particle surface, and
- 5) diffusion of CO₂ from the particle surface to the surrounding atmosphere.

For analysis in fluidized beds, step 5 is often subdivided into a film diffusion step from the particle surface to the particulate phase, and an interphase mass transfer step from the particulate phase to the bubbles [12].

The rate-controlling step in the calcination of limestone is the subject of debate. Many researchers [10, 12-14] have determined that the reaction is controlled by the chemical reaction step at the reaction interface. Khraisha and Dugwell [10] report that the reaction is chemically controlled, but that the particle temperature was dependent on heat transfer from the reactor to the particle surface, rather than dependent on internal conduction. Hills [11] demonstrated that for 10 mm diameter spheres, which is a relatively large sorbent particle, the reaction was controlled by heat transfer to the reaction interface and mass transfer away from the reaction interface.

Rajeswara *et al.* [15] abandoned the more traditional shrinking core approach and analyzed the reaction using a grain model. They found that the assumption of an isothermal particle is not valid. In their analysis, the radial temperature variation is considered through the use of a steady state relationship developed by Prater [16]. To validate their analysis, they measured the temperature of a 6 mm diameter pellet at a location 1 mm below its

surface. Temperature at this location dropped from 1150 K to 1090 K during the endothermic calcination reaction. From their analysis they found radial temperature variations of 40 K through the pellet. The use of large (6 mm) manufactured pellets may impact the usefulness of their analysis for FBC boilers, which use raw limestone with smaller particle diameters.

Dennis and Hayhurst [12] argue that interphase mass transfer cannot be controlling since the reaction radius decreases linearly with time. They also calculated the maximum temperature difference by equating conduction heat transfer through the CaO layer to the heat absorbed through the calcination reaction. Using values from the literature for thermal conductivity [17] and heat of calcination [11], they found that the maximum temperature difference across the particle is 11 K. From this they dismissed conduction through the CaO ash layer as a rate-limiting mechanism. Nevertheless, they concede that interphase heat transfer can act as a resistance to reaction. In their model, they include only the chemical reaction step and the pore diffusion step. They develop an expression for the calcination reaction rate, which is a function of the equilibrium and instantaneous partial pressures of CO₂, the total pressure and a fixed mole fraction of CO₂.

Several researchers have shown that the specific surface area of the calcine is reduced at higher temperatures and concentrations of CO₂ and H₂O [18-20]. Stouffer and Yoon [20] calcined 100 mesh limestone samples in air at temperatures of 975 K, 1075 K, and 1175 K. They found that BET surface area is created more quickly at higher temperatures than at lower temperatures. At higher temperatures, however, a rapid reduction in surface area occurs shortly after it is created. The net effect is that limestone calcined at higher temperatures develops less surface area. For limestone calcined at 1175 K, the surface area after two minutes was 50 m²/g, but then it diminished to 33 m²/g after 10 minutes, and 25 m²/g after 30 minutes. Milne *et al.* [18] analyzed data from Borgwardt [21]

and found substantially higher sintering rates in atmospheres containing H₂O and CO₂, than in N₂ atmospheres. They also found that the effects of H₂O and CO₂ were additive.

2.3 Sulfation

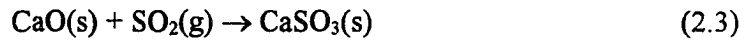
Complete utilization of CaO in the calcined limestone particle is usually not possible because of the buildup of CaSO₄, which limits access to active sites. The molar volumes of CaCO₃, CaO, and CaSO₄ are 36.9, 16.9 and 46.9 cm³/mol, respectively [22]. This results in a theoretical maximum utilization of 69 % without growth of the particle, when starting with a non-porous particle. Actual conversions can be much less due to sintering during calcination and the plugging of pores by CaSO₄. At normal FBC operating conditions the net sulfation reaction is commonly written as:



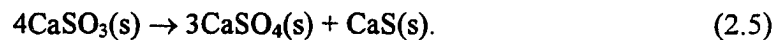
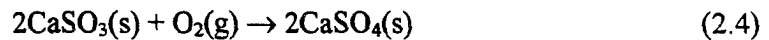
This reaction is generally considered to be first order with SO₂ and zeroth order with oxygen when O₂ is greatly in excess. At higher temperatures, the reverse reaction needs to be considered. Additionally the presence of CO and H₂O at the reaction site may promote reductive decomposition of CaSO₄ [13]. These reactions are significant at temperatures in excess of 1000°C. An optimum temperature of sulfur sorption exists in the range of 800 - 850°C. At temperatures below this range the calcination rate is reduced, which leads to a decrease in surface area for reaction. At temperatures above this range three phenomena contribute to a reduced conversion: more rapid plugging of pores caused by higher reaction rates, sintering of the CaO matrix, which reduces surface area, and participation of reverse and reductive decomposition reactions [6,13,18,19].

Dam-Johansen and Ostergaard [23] present the sulfation reaction more generally as

a reaction which produces calcium sulfite as an intermediary step:



The CaSO_3 then reacts to form CaSO_4 and calcium sulfide (CaS) depending upon the oxygen concentration by the net reactions:



Under reducing conditions such as are found in the dense phase of a circulating FBC, the presence of hydrogen sulfide, H_2S , may cause another reaction in which CaS is formed instead of CaSO_4



This reaction is significant for full scale FBC operations where combustion air is supplied in two stages as a means of nitrogen oxide (NO_x) control. Higher sorbent utilizations can be achieved under these conditions, since the lower molar volume of CaS does not limit the extent of reaction, which is the result when CaSO_4 is the product. When exposed to oxidizing conditions CaS rapidly reacts to form CaSO_4 .

As in calcination, the reaction process takes place in several steps. The following mechanisms are generally thought to be important:

- 1) mass transfer from the particulate phase to the particle surface
- 2) diffusion through particle pores containing some level of CaSO_4 build up

- 3) diffusion at the grain level through a product layer, and
- 4) chemical reaction with CaO.

Unlike calcination, the sulfation reaction is assumed to be isothermal. Mass transfer from the bubble phase to the particulate phase is not usually considered, except that in some cases it is noted that depletion of SO₂ in the emulsion can cause a reduced reaction rate [13]. Another important difference between calcination and sulfation is that the diffusivity through the particle varies considerably during the process as CaSO₄ deposits in the pores.

Chemistry, pore diffusion, and product layer diffusion have all been proposed as rate limiting processes in the literature for different operating conditions, particle sizes, and reaction times. [5,6,13]. Borgwardt and Harvey [5] investigated eleven sorbents and found distinct behaviors that were dependent upon the mean pore size of the calcine. They measured an effectiveness factor, which was defined as the ratio of the reaction rate of a given particle size to that of small 0.096 mm particles of the same sorbent. For sorbents such as marbles and pure calcites, the mean pore diameter of around 0.075 μm caused rapid plugging of pores and low effectiveness factors. In these particles the reaction rate was proportional to 1/d_p². For most of the limestones, which had calcine pore diameters ranging from 0.27 to 0.6 μm, the reaction rate was proportional to 1/d_p for particles larger than 150 μm. For smaller particles, the reaction rate was independent of particle size indicating a shift from diffusion to chemical reaction control. The marl and the aragonite they tested had pore diameters of 1.6 and 4.0 μm, respectively. These two carbonate rocks showed no particle size dependence, indicating that they were controlled exclusively by chemistry control. For these particles, the large pores allowed the reaction to proceed evenly throughout the particle.

Other researchers have found that product layer diffusion is rate limiting [6,24]. In this case the limiting step involves diffusion of reacting species through a product layer that

surrounds CaO grains. The exact nature of this diffusion step is likely to be ionic diffusion, although this is not certain. Mulligan *et al.* [6] obtained a high activation energy for the reaction after an initial period in which the product layer was forming. This led them to conclude that the reaction was controlled by solid state diffusion with the diffusing species probably being Ca^{+2} and O^- ions. Bhatia and Perlmutter [24] similarly found a high activation energy for diffusion of 28.7 kcal/mol, which is in a range of values commonly found for ionic diffusion. However, they do recognize that several other plausible mechanisms could be involved. One such mechanism may be activated crack nucleation of the CaSO_4 layer, which would allow SO_2 and O_2 to diffuse to the unreacted CaO grain core.

Hsia *et al.* [25,26] experimentally determined that ionic diffusion of Ca^{+2} and O^- is indeed the mechanism involved in product layer diffusion. In their first experiment they imbedded inert platinum markers between CaO and CaSO_4 and observed that the product layer thickens by an outward growth mode. In this analysis they observed SEM maps that show the product phase extending away from the platinum in the direction of the CaSO_4 [25]. In further work they confirmed this conclusion using an enriched sulfur isotope to mark the direction of the diffusion process [26].

Determination of the controlling process is crucial to understanding the sulfation reaction. It is clear that the large number of variables such as pore size, surface area, temperature, and particle size all play a role in determining the controlling reaction for a given type of limestone. In addition, the reaction may initially be controlled by one mechanism, such as chemistry control, and then for later times be controlled by another mechanism. For these reasons it is important to evaluate the reactions under realistic conditions. In order to understand the reaction in the course of changing controlling mechanisms, it is necessary to find an appropriate model for the reaction.

The goal of this study is to use transient gas analysis as a tool in characterizing sorbents. The approach to this investigation begins with the development of a model that

realistically represents the mechanisms of the reaction, and simulates the reaction as it occurs in the laboratory combustor. Simplifications to this model under the assumption of specific controlling mechanisms are developed. These simplified models will correspond directly with transient data if the assumed controlling mechanism is valid. Finally, particle analysis is conducted to give a physical interpretation to the transient gas analysis. Upon validation of the transient gas analysis methods, application to full-scale boilers is considered.

3. MODELING

3.1 Overview of Model Types

To develop meaningful interpretation of exhaust gas transients, models were developed for the calcination and sulfation processes. There are several ways of modeling these two reactions in the literature. They range from detailed numerical mechanistic models to more specifically applied empirical models. In this study, the desired model is one that is simple enough to be applied to full scale boilers, and yet detailed enough to give meaningful characterization of sorbents for a broad range of conditions.

Many physical-chemical models have been developed for gas-solid reactions. In a detailed discussion of gas-solid models, Bradley and Doraiswamy [27] discuss several that have been considered for application in sorbent reactions. Figure 3.1 organizes the models used in sorbent reactions into several groups. These mechanistic models can be divided into three main groups: particle models, grain models, and pore models.

In particle models, the focus is on the time-rate-of-change of processes occurring within the particle. These models generally resolve into sets of ordinary differential equations with time differentials, which sometimes may be simplified further. Analysis of how the reaction dynamics change as a function of particle radius is not considered using partial differential equations. In these models, grain and pore sizes are important only in their effect on transport and reaction properties that are characteristic for the particle at a given time.

Two limiting cases of particle models are sharp interface models and volume reaction models. In the sharp interface model, chemical reaction occurs at the interface between a layer of product and the unreacted region within the particle. If a spherical particle is assumed and the reaction interface proceeds from outside to the center, the result is a shrinking core model. Volume reaction models are used for highly porous particles in

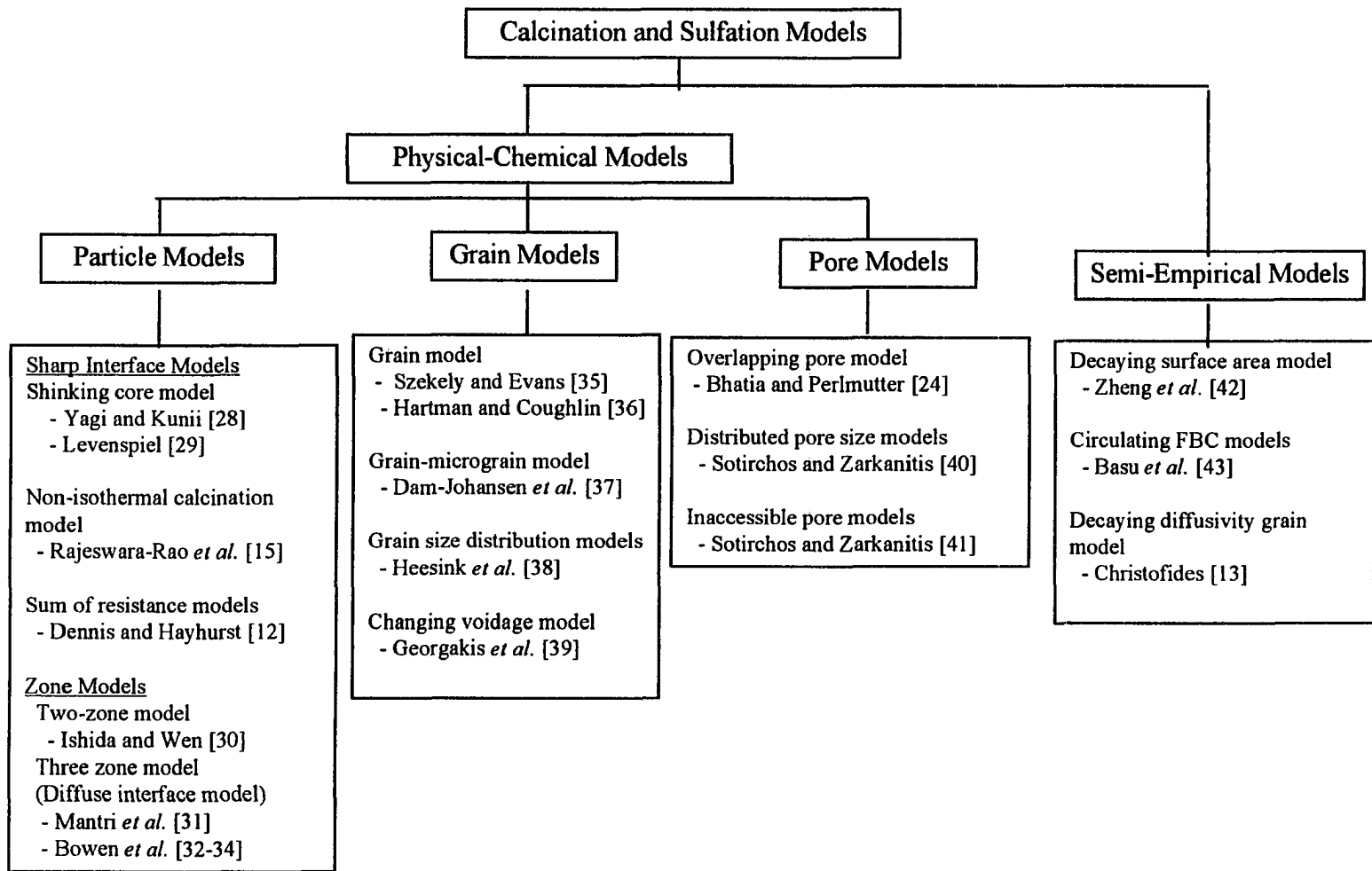


Figure 3.1 Overview of models used in sorbent reactions

which reactant gases can penetrate the solid and react throughout the particle.

Zone models are more general particle models that describe the reaction in zones within the particle. In a two-zone model, as suggested by Ishida and Wen [30], reaction takes place throughout the particle until a zone consisting of only product develops on the exterior and moves inward replacing the reacting core. A more general zone model is a three-zone model, also referred to as a diffuse interface model [31, 32-34]. In these models a reaction zone may exist between an unreacted core and outer product layer. If the particle properties and conditions are such that a large reaction zone develops, the model may reduce to a two-zone model or a volume reaction model. If the reaction zone developed is small, the model becomes a shrinking core model in the limiting case.

In grain models, chemical reaction takes place at the grain level. As with particle models, grain models consider film mass transfer and intraparticle diffusion of reactant gases, but the reaction rate is based on the surface area of the grains. Some of these models also consider volume changes at the grain level and ionic diffusion through a product layer deposited around the grains. Reaction at the grains is often described using a shrinking grain core to describe the reaction area [15, 36]. Since the grain core radius is a function of the particle core radius, these models generally evolve into sets of partial differential equations to account for changes with respect to both particle radius and time.

Several adaptations of the grain model have been developed since its original development by Szekeley and Evans [35]. Dam-Johansen *et al.* [37] developed a grain-micro-grain model to account for the bi-modal pore size distribution found in calcined limestone. The pores developed during calcination are typically much smaller than those in the original stone. The grains in their model consist of a large number of micro-grains that have a uniform size based on the micro-porosity of the limestone. Georgakis *et al.* [39] developed a model that accounts for the growth of grains caused by the product layer building up around them. Since the grains in this model initially have a uniform radius,

conversion values reach a maximum abruptly, which is unlike the asymptotic approach that is seen in actual transients. The use of grain size distributions can modify this result.

Heesink *et al.* [38] measured the pore size distribution of two limestones, and converted this information into a grain size distribution with a variable number of grain size intervals. Increasing the number of size intervals in this distribution gave progressively better fits to experimental data.

The development of pore models has roughly paralleled that of grain models. Pore models in the literature account for overlapping of pores, pore size distribution effects, and formation of inaccessible pore volume during sulfation [24, 40, 41]. Pore models and grain models typically involve partial differential equations, however. A goal of this investigation is to find a model that is simple enough so that it can be linearized to show the characteristics of the sorbent reactions from emissions transients. Consequently, adaptations of the shrinking core model were investigated more fully as they applied to calcination and sulfation.

3.2 Modeling of Calcination

3.2.1 Model development

Most of the calcination models reviewed were variations of the shrinking core model (SCM) introduced by Yagi and Kunii [28] as described in Levenspiel [29]. The basic SCM consists of a chemical reaction at a receding particle core, diffusion through the outer portion of the particle, and diffusion through a gas film surrounding the particle. The time-rate-of-change of the flux of the diffusing species, based on the unchanging exterior surface of the particle, can be written as:

$$-\frac{1}{a_p} \frac{dN_A}{dt} = \frac{C_A}{R_{\text{film diffusion}} + R_{\text{pore diffusion}} + R_{\text{chemical reaction}}}. \quad (3.1)$$

In equation (3.1), the resistances are functions of the film mass transfer coefficient, h ; the chemical reaction rate coefficient, k ; the effective diffusivity through the particle, D_e ; and the radii of the particle and of the core; r_p and r_c , respectively. The SCM is a sum of resistances model, and is analogous to an electrical or heat transfer sum of resistances approach, involving a flux, a potential and a network of resistances in series.

Many investigators have concluded that calcination is controlled by a chemical reaction step at the interface of CaCO_3 and CaO , but some others have suggested control by heat transfer and mass transfer from the interface [11]. Dennis and Hayhurst [12] used a sum-of-resistances model that included ash diffusion and chemical reaction resistances. They developed an equation for the calcination reaction time, t_c , which was simplified by showing that the diffusion resistance is much less than the chemical reaction resistance for pressures up to 3 bar. Their final equation is for chemical control, with chemical reaction rate driven by the difference between CO_2 partial pressure and the equilibrium pressure for the calcination and the carbonation reactions. Their final equation for the time to complete calcination is:

$$t_c = \frac{r_p}{k^* V_{\text{CaCO}_3} (p_E - p_R - y^* P)}, \quad (3.2)$$

where k^* is the chemistry rate constant for the backward, or carbonation, reaction, V_{CaCO_3} is the molar volume of CaCO_3 , p_E is the equilibrium partial pressure, p_R is the instantaneous partial pressure of CO_2 , P is the total pressure, and y^* is a constant mole fraction of CO_2 , which is determined from regression analysis of the data. The rate constant for calcination used for comparison to other values in the literature is the term $k^* p_E$.

Rajeswara Rao *et al.* [15] describe a slightly more complicated model. Their model is a grain model, which accounts for temperature differences within the particle. They use a set of two partial differential equations to describe diffusion and reaction in the solid pellet and in the grain. A relationship for temperature that includes external film resistances, as well as internal conduction and mass transfer, accompanies these equations. This equation for temperature takes on the following form:

$$T = T_o - \frac{h_c \Delta H}{h_T} ([CO_2]_S - [CO_2]_R) - \frac{D_{e_c} \Delta H}{k_c^*} ([CO_2] - [CO_2]_S) \quad (3.3)$$

where h_T is the heat transfer coefficient; k_c^* is the particle thermal conductivity; ΔH is the heat of reaction; and $[CO_2]_R$, $[CO_2]_S$, and $[CO_2]$ are concentrations of CO_2 in the combustor, at the particle surface, and in the particle as a function of radius, respectively.

The approach to the present study assumes an isothermal shrinking particle core model that includes chemical reaction, diffusion of CO_2 through a product layer, film mass transfer away from the particle, and bulk mass transfer in the bed. Assuming a continuously stirred tank reactor (CSTR), mass balances in the reactor result in a set of four differential equations for the core radius and for concentrations of CO_2 in the reactor, at the particle surface and at the unreacted core:

$$V_R \frac{d[CO_2]_R}{dt} = -Q \{ [CO_2]_R - [CO_2]_I \} + h_c a_p \{ [CO_2]_S - [CO_2]_R \} \quad (3.4)$$

$$V_P \frac{d[CO_2]_S}{dt} = -h_c a_p \{ [CO_2]_S - [CO_2]_R \} + 4\pi \frac{\delta_{ec}}{\frac{1}{r_p} - \frac{1}{r_{cc}}} \{ [CO_2]_S - [CO_2]_{CC} \} \quad (3.5)$$

$$V_c \frac{d[CO_2]_{CC}}{dt} = 4\pi \frac{\delta_{ec}}{\frac{1}{r_p} - \frac{1}{r_{cc}}} \{ [CO_2]_{CC} - [CO_2]_S \} + k_c a_{cc} \{ [CO_2]_E - [CO_2]_{CC} \} \quad (3.6)$$

$$\frac{dr_{cc}}{dt} = -\frac{k_c M_L}{\rho_L} \{ [CO_2]_E - [CO_2]_{CC} \} \quad (3.7)$$

where $[CO_2]_I$ and $[CO_2]_{CC}$ are the concentrations of CO_2 at the inlet and at the unreacted $CaCO_3$ core, respectively. This system of ordinary differential equations will be referred to as the “full model” in subsequent discussions. The equilibrium concentration is determined by ideal gas conversion from the equilibrium partial pressure, i.e. $[CO_2]_E = p_E/RT_{bed}$. The equilibrium partial pressure is determined from an analysis by Baker *et al.* [44] which results in the partial pressure for the calcination equilibrium (in atmospheres) equal to:

$$\log_{10} p_E = -\frac{8308}{T} + 7.079. \quad (3.8)$$

If a quasi-steady approximation is applied to this model, time derivatives of $[CO_2]$ are set equal to zero, and the model simplifies to one ordinary differential equation and one algebraic equation:

$$-\frac{dr_{cc}}{dt} = \frac{\{ [CO_2]_E - [CO_2]_I \} \frac{M_{LS}}{f_{CaCO_3} \rho_{LS}}}{\frac{3m_{LS}}{Q\rho_{LS}r_p} \frac{r_{cc}^2}{r_p^2} + \frac{1}{h_c} \frac{r_{cc}^2}{r_p^2} + \frac{(r_p - r_{cc})r_{cc}}{D_{ec}r_p} + \frac{1}{k_c}} \quad (3.9)$$

$$\frac{[CO_2]_E - [CO_2]_R}{[CO_2]_E - [CO_2]_I} = \frac{1}{1 + \frac{3m_{LS}}{Q\rho_{LS}r_p} \left(\frac{1}{\frac{1}{h_c} + \frac{(r_p - r_{cc})r_p}{D_{ec}r_{cc}} + \frac{1}{k_c} \frac{r_p^2}{r_{cc}^2}} \right)} \quad (3.10)$$

This model can be easily extended to non-spherical particles by introducing a shape factor, S , which is equal to 3 for spheres, 2 for cylinders and 1 for flat plates. A characteristic length, L , represents the particle radius for spheres and cylinders, and represents the half-thickness for flat plates. The ratio S/L is the ratio of surface area to volume for these particles. With these modifications, and defining ξ_c equal to r_{cc}/r_p , Eqns. (3.9) and (3.10) become:

$$-\frac{d\xi_c}{dt} = \frac{\{[CO_2]_E - [CO_2]_I\} \frac{M_{LS}}{f_{CaCO_3} \rho_{LS} L}}{\frac{Sm_{LS}}{Q\rho_{LS}L} \xi_c^{(S-1)} + \frac{1}{h_c} \xi_c^{(S-1)} + \frac{L(1-\xi_c)\xi_c^{(S-1)/2}}{D_{ec}} + \frac{1}{k_c}} \quad (3.11)$$

$$\frac{[CO_2]_E - [CO_2]_R}{[CO_2]_E - [CO_2]_I} = \frac{1}{1 + \frac{Sm_{LS}}{Q\rho_{LS}L} \left(\frac{1}{\frac{1}{h_c} + \frac{L(1-\xi_c)}{D_{ec}\xi_c^{(S-1)/2}} + \frac{1}{k_c\xi_c^{(S-1)}}} \right)} \quad (3.12)$$

These equations can also be derived by assuming a sum of resistances model as considered in Levenspiel [29], with the inclusion of a CSTR bed mixing resistance. If one of the resistances in Eqns (3.11) and (3.12) is considerably larger than the others, then limiting behavior is observed.

3.2.2 Model simplification resulting from limiting behavior

An objective of this investigation is to find time constants to characterize sorbent reactions analytically through time series or spectral methods. The shrinking core model of Eqns. (3.11) and (3.12) is useful in analyzing the transients, but comparison must be done numerically. The model can be simplified further by assuming rate-limiting mechanisms. To

simplify the expressions, two constants are defined: $c_{1c} = \{[CO_2]_E - [CO_2]_I\}M_{LS}/f_{LS}\rho_{LS}$, and $c_2 = Sm/\rho_{LS}Q$. For the present discussion, analysis will be for spheres ($S = 3$) unless otherwise indicated. The four possible controlling mechanisms that can be examined by this model are: chemical reaction rate, film diffusion, pore diffusion, and bulk mass transfer. The following analysis addresses each of these possibilities.

3.2.2.a Chemical reaction control

If chemical reaction is the controlling mechanism, the chemical reaction resistance term in Eqns. (3.11) and (3.12) is larger than the other resistances, so that the equations may be rewritten:

$$-\frac{d\xi_c}{dt} = \frac{c_{1c}}{L} k_c \quad (3.13)$$

$$\frac{[CO_2]_E - [CO_2]_R}{[CO_2]_E - [CO_2]_I} = \frac{1}{1 + \frac{c_2}{L} k_c \xi_c^2} \quad (3.14)$$

Equation (3.13) can be integrated directly to yield:

$$\xi_c = 1 - \frac{c_{1c}}{L} k_c t \quad (3.15)$$

which is the first two terms of the Taylor series expansion for the exponential function. Consequently, for short times ξ_c may be approximated by:

$$\xi_c = e^{(-t/\tau_{ck})} \quad (3.16)$$

where $\tau_{ck} = L/k_c c_{1c}$. Substituting this result into Eqn. (3.14) and inverting the equation results in:

$$\frac{[CO_2]_E - [CO_2]_I}{[CO_2]_E - [CO_2]_R} - 1 = \frac{c_2 k_c}{L} e^{-2t/\tau_{ck}} \quad (3.17)$$

Recognizing that $[CO_2]_R$ is equal to $[CO_2]_O$ at time zero, the equation takes on the form:

$$\frac{\{[CO_2]_E - [CO_2]_O\} \{[CO_2]_R - [CO_2]_I\}}{\{[CO_2]_E - [CO_2]_R\} \{[CO_2]_O - [CO_2]_I\}} = e^{-t/\tau_c} \quad (3.18)$$

where $\tau_c = \tau_{ck}/2 = r_p/2k_c c_{1c}$. For equilibrium concentrations substantially larger than the reactor concentrations, Eqn. (3.18) is approximated by:

$$\frac{\{[CO_2]_R - [CO_2]_I\}}{\{[CO_2]_O - [CO_2]_I\}} = e^{-t/\tau_c} \quad (3.19)$$

This approximation gives approximately 5% error in the value of τ_c for atmospheric combustion at 1123 K.

The calcination time constant, τ_c , can be determined graphically from the slope of a log-linear plot of Eqn. (3.18). For chemistry controlled calcination, τ_c is directly proportional to L , which is r_p for the spherical particle shape. Additionally, it is seen that τ_c is inversely proportional to the reaction rate coefficient, k_c , and to $\{[CO_2]_E - [CO_2]_I\}$.

Comparison of the value of τ_c determined in this way for differing particle sizes, temperatures, and concentrations will indicate whether chemistry is the controlling mechanism. If τ_c is plotted versus particle diameter on a log-log plot, the slope will give the particle size dependence. For chemistry control, the slope should be equal to one. A log-

linear plot of $1/\tau_c$ versus $1/T$ will yield the observed activation energy for calcination. If chemistry is controlling the observed activation energy should equal the true activation energy. If particle shapes other than spheres are used, the value of τ_c will also be proportional to $1/(S-1)$. For flat plates this results in an infinite value for τ_c , corresponding to a constant outlet concentration. For every shape, chemistry control results in an interface that recedes at a constant rate.

3.2.2.b Film diffusion control

If calcination is controlled by diffusion through the gas film surrounding the particle, the film diffusion resistances will be much larger than the other resistances. For the film diffusion control case, Eqns (3.11) and (3.12) become:

$$-\frac{d\xi_c}{dt} = \frac{c_{1c}h_c}{L\xi_c^2} \quad (3.20)$$

$$\frac{[CO_2]_E - [CO_2]_R}{[CO_2]_E - [CO_2]_I} = \frac{1}{1 + \frac{c_2}{L}h_c} \quad (3.21)$$

Integration of Eqn. (3.20) yields:

$$\xi_c = \left(1 - \frac{3c_{1c}h_c t}{L}\right)^{1/3} \quad (3.22)$$

and application of the Taylor series expansion of the exponential function results in:

$$\xi_c = e^{-t / \tau_{ch}} \quad (3.23)$$

where $\tau_{ch} = L/h_c c_{1c}$. Equation (3.21) shows that the concentration transient is constant with time for film diffusion control. This response has not been observed in laboratory experiments nor in the literature. Although film diffusion may play a role in the calcination process, it clearly does not act as the controlling mechanism.

3.2.2.c Pore diffusion control

To illustrate the effect of pore diffusion control, analysis is done for flat plates, utilizing the inherently simpler mathematics for this shape. For pore diffusion control Eqn. (3.11) becomes:

$$-\frac{d\xi_c}{dt} = \frac{D_{ec} c_{1c}}{L^2(1-\xi_c)} \quad (3.24)$$

Integration of Eqn. (3.24) yields:

$$(1-\xi_c)^2 = \frac{2D_{ec} c_{1c}}{L^2} t = t/t_c \quad (3.25)$$

where t_c , the time to completely calcine the particle, is $L^2/(2D_{ec} c_{1c})$. The expression for the dimensionless core radius is:

$$\xi_c = 1 - \sqrt{\frac{t}{t_c}} \quad (3.26)$$

If pore diffusion is determined to be the controlling mechanism for calcination, the transient can be analyzed by writing Eqn. (3.12) for pore diffusion control:

$$\frac{[CO_2]_E - [CO_2]_I}{[CO_2]_E - [CO_2]_R} - 1 = \frac{c_2 D_{ec}}{L^2 (1 - \xi_c)} \quad (3.27)$$

Inversion and substitution of Eqn. (3.26) into Eqn. (3.27) yields:

$$\left(\frac{[CO_2]_E - [CO_2]_I}{[CO_2]_E - [CO_2]_R} - 1 \right)^{-1} = \left(\frac{[CO_2]_E - [CO_2]_I}{[CO_2]_R - [CO_2]_I} - 1 \right) = \frac{L^2}{c_2 D_{ec}} \sqrt{t/t_c} = \sqrt{t/\tau_{cd}} \quad (3.28)$$

where $\tau_{cd} = c_2^2 D_{ec} / 2c_{1c} L^2$. By making use of a Taylor series approximation, the linearized equation for short times is:

$$\left(\frac{[CO_2]_E - [CO_2]_I}{[CO_2]_R - [CO_2]_I} \right) = 1 + \left(\frac{t}{\tau_{cd}} \right)^{1/2} \cong e^{\sqrt{t/\tau_{cd}}} \quad (3.29)$$

Inverting once more, results in:

$$\left(\frac{[CO_2]_R - [CO_2]_I}{[CO_2]_E - [CO_2]_I} \right) = e^{-\sqrt{t/\tau_{cd}}} \quad (3.30)$$

The calcination time constant, τ_{cd} , can be determined from the reciprocal slope of a “log-squared”-linear plot:

$$\left\{ -\ln \left(\frac{[CO_2]_R - [CO_2]_I}{[CO_2]_O - [CO_2]_I} \right) \right\}^2 = \frac{1}{\tau_{cd}} t \quad (3.31)$$

Alternatively, Eqn. (3.28) results in a simple expression:

$$\left(\frac{[CO_2]_R - [CO_2]_I}{[CO_2]_E - [CO_2]_R} \right)^{-2} = \frac{1}{\tau_{cd}} t \quad (3.32)$$

which is valid for all times and can be plotted directly to fit a value of τ_{cd} .

3.2.2.d Bulk mass transfer control

If bulk mass transfer is the controlling mechanism, bed mixing resistance ($3m_{LS}/\rho_{LS}Qr_p$) is significantly larger than the other resistances. For this case Eqn. (3.11) can be written:

$$-\frac{d\xi_c}{dt} = \frac{c_{1c}}{c_2\xi_c^2} \quad (3.33)$$

Integrating and using the Taylor series expansion for the exponential function, Eqn. (3.33) becomes:

$$\xi_c = e^{-t / \tau_{cb}} \quad (3.34)$$

where $\tau_{cb} = c_2/c_{1c}$. Simplification of Eqn. (3.12) for bulk mass transfer control results in:

$$\frac{[CO_2]_E - [CO_2]_R}{[CO_2]_E - [CO_2]_I} = \frac{1}{1 + \frac{c_2}{L} K(t)} \quad (3.35)$$

In Eqn. (3.35), $K(t)$ is the overall reaction coefficient from the other resistances. Since the chemical and diffusion resistance terms are time dependent, $K(t)$ is written as a function of time. This allows for consideration of two cases in which bulk mass transfer is the primary

controlling mechanism and either chemical reaction resistance or pore diffusion resistance is the secondary controlling mechanism.

For the case in which chemical reaction is the secondary mechanism, resistances of film mass transfer and pore diffusion are neglected. By substituting $1/R_{\text{chem}}$ into Eqn. (3.35) for $K(t)$, and combining with the expression for ξ_c in Eqn. (3.34), an expression for the transient is written as:

$$\frac{[CO_2]_E - [CO_2]_R}{[CO_2]_E - [CO_2]_I} = \frac{1}{1 + \frac{c_2}{L} k_c e^{-2t/\tau_{cb}}} \quad (3.36)$$

By applying the condition that $[CO_2]_R$ is equal to $[CO_2]_O$ at time zero, the resulting expression can be written:

$$\frac{\{[CO_2]_E - [CO_2]_O\} \{[CO_2]_R - [CO_2]_I\}}{\{[CO_2]_E - [CO_2]_R\} \{[CO_2]_O - [CO_2]_I\}} = e^{-t/\tau_c} \quad (3.37)$$

where $\tau_c = \tau_{cb}/2 = c_2/(S-1)c_{1c}$. This represents a case where the time constant is independent of τ_p and k_c , even though the chemical reaction is the only mechanism considered other than bulk mass transfer.

If pore diffusion is the secondary mechanism, and a flat plate is considered, Eqn. (3.35) becomes:

$$\frac{[CO_2]_E - [CO_2]_R}{[CO_2]_E - [CO_2]_I} = \frac{1}{1 + \frac{c_2}{L^2} \frac{D_{ec}}{(1-\xi_c)}} \quad (3.38)$$

Substitution of the dimensionless core radius from Eqn. (3.34), and use of the Taylor series

approximation for ξ_c , results in:

$$\left(\frac{[CO_2]_E - [CO_2]_R}{[CO_2]_R - [CO_2]_I} \right) = \left(\frac{[CO_2]_R - [CO_2]_I}{[CO_2]_E - [CO_2]_I} \right)^{-1} = \frac{c_{1c}L^2}{c_2^2 D_{ec}} t = \frac{1}{\tau_{cbd}} t \quad (3.39)$$

where $\tau_{cbd} = 2\tau_{cd} = c_2^2 D_{ec} / c_{1c} L^2$.

From these cases it is seen that bulk mass transfer may affect the reaction rate, but its effect will depend upon the relative strengths of the other mechanisms. If calcination is strongly influenced chemical reaction, bulk mass transfer changes the time constant such that it is no longer dependent upon particle size or chemical reaction rate. For pore diffusion, it doubles the time constant and changes the order of the response.

3.3 Modeling of Sulfation

3.3.1 Model development

Many different models for sulfation have been proposed in the literature. The reaction is complex because it involves a 175% increase in molar volume while proceeding from CaO to CaSO₄. This increase in volume, along with the wide variety of pore structures found in sorbents, causes modeling of this reaction to be difficult. Many of the mechanistic models provide an accurate representation of the reaction. The focus of the present study, however, is to characterize sulfation by time constants with time series analytical methods employed in the study. To determine such time constants, simpler models are developed from ordinary differential equations.

Zheng *et al.* [42] developed a semi-empirical model that considers first-order reaction in a CSTR. A mass balance with first order reaction gives:

$$C_{A_0}Q = C_A Q + k_s C_A S \quad (3.40)$$

Where k_s is the reaction rate coefficient based on the particle external surface area, S . Zheng *et al.* observed that progressive pore blocking causes the rate of reaction to decrease exponentially with time. This is modeled by assuming that the particle external surface area decays exponentially with time, taking on the form:

$$S = S_0 e^{-k_d t} \quad (3.41)$$

where $S_0 = 3m_{LS}/\rho_{LS}r_p$. In these equations, k_d is a deactivation rate constant, m_{LS} is the mass of the batch, Q is the flow rate through the combustor, ρ_{LS} is the limestone density, and r_p is the diameter of a spherical particle. For continuous addition of limestone and coal, the fractional reduction in steady state SO_2 emissions compared to expected emissions in the absence of sorbent, η_s , is computed by:

$$\eta_s = \frac{(C_{A_0} - C_A)}{C_{A_0}} = 1 - \frac{1}{1 + K\beta} \quad (3.42)$$

In equation (3.42), β is the calcium-to-sulfur molar ratio, and K depends on particle properties, reactor operating conditions, reaction rate constant (k_s), and deactivation rate constant (k_d).

For transient analysis with batch addition, this model can be expressed as:

$$\frac{C_A}{C_{A_0}} = \frac{1}{1 + \frac{k_s S}{Q}} = \frac{1}{1 + \frac{3m_{LS}k_s}{Q\rho_{LS}r_p} e^{-k_d t}} \quad (3.43)$$

The time dependence for this system is determined by the deactivation rate constant, k_d . This simple model would be attractive, except that preliminary experiments performed in this study did not yield the simple exponential relationship suggested by Eqn. (3.43).

In the present study, a grain model that described sulfation in terms of ordinary differential equations was first attempted. This model, developed by Christofides and Brown [45], considered film diffusion, pore diffusion through the particle, diffusion through a product layer at individual grains, and reaction at a shrinking grain core. These processes are depicted in Fig. 3.2. In this model, pore diffusion is described by a decaying exponential with a time constant of τ_p for pore plugging. An effectiveness factor, ε_s , is defined to relate pore diffusion through the particles and product layer diffusion at the grains. In this way only the grain radius is a parameter and the radial location in the particle is not considered in the model. The model is described by four ordinary differential equations:

$$\frac{d[SO_2]_R}{dt} = \frac{Q}{V_b} \{[SO_2]_i - [SO_2]_R\} - h_s a_p \frac{N_p}{V_b} \{[SO_2]_R - [SO_2]_S\} \quad (3.44)$$

$$\frac{d[SO_2]_S}{dt} = \frac{h_s a_p N_p}{V_b} \{[SO_2]_R - [SO_2]_S\} - \varepsilon_s \frac{\delta_{pl} a_{gc} N_p}{t_{pl} V_b} \{[SO_2]_S - [SO_2]_{gc}\} \quad (3.45)$$

$$\frac{d[SO_2]_{gc}}{dt} = \varepsilon_s \frac{\delta_{pl} a_{gc} N_p}{t_{pl} V_b} \{[SO_2]_S - [SO_2]_C\} - \frac{k_S a_{gc} N_p}{V_b} [SO_2]_C \quad (3.46)$$

$$\frac{dr_{gc}}{dt} = - \frac{k_S M_{CaO}}{\rho_{CaO}} [SO_2]_C \quad (3.47)$$

Where the effectiveness factor is given by:

$$\varepsilon_s = \frac{3}{\phi_s} (\phi_s \coth \phi_s - 1) \quad (3.48)$$

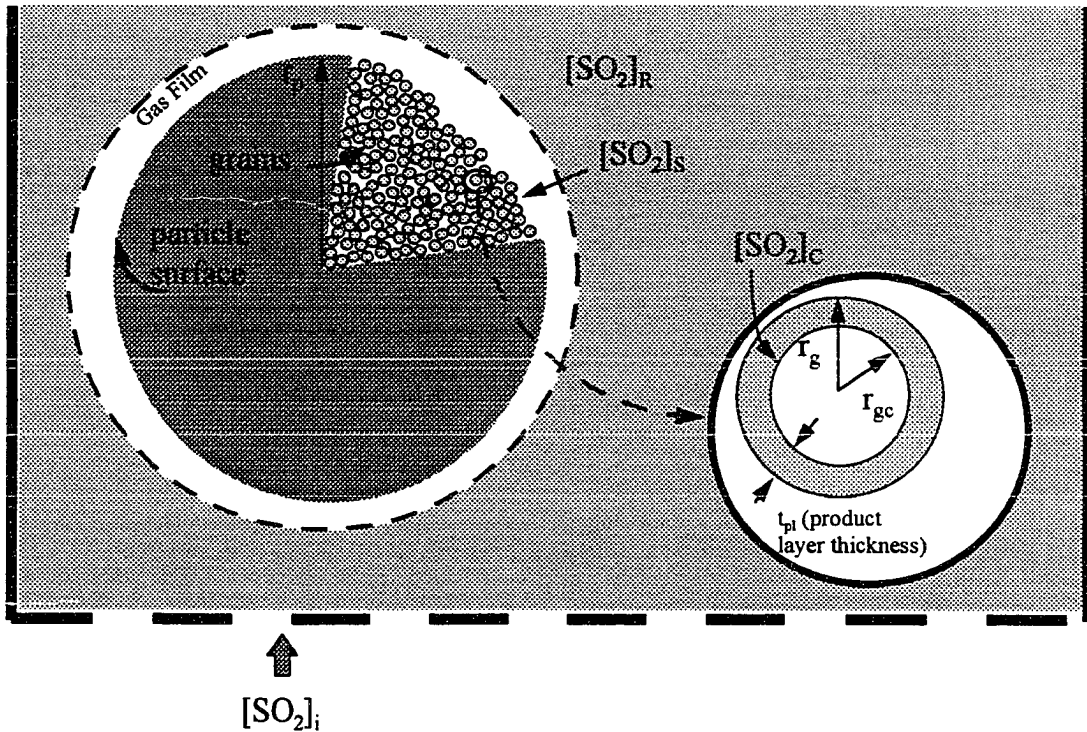


Figure 3.2 Schematic of shrinking grain core model for sulfation.

In equation (3.48) ϕ_s is a Thiele modulus for sulfation, which is expressed by:

$$\phi_s = r_p \sqrt{\frac{d_{pl} \rho_{CaO} S_g}{t_{pl} d_{es} e^{-t/\tau_p}}} \quad (3.49)$$

Pore diffusivity decays exponentially with time according to the time constant, τ_p . As the pore diffusivity becomes smaller, the Thiele modulus becomes larger, and the reaction is controlled by product layer diffusivity at the grain level. In this case the effectiveness factor approaches $3/\phi_s$.

An advantage of this model was that time constants for different rate-limiting conditions could be derived by using quasi-equilibrium assumptions, and applied to experimental data. Unfortunately, this model did not always correlate well with lab scale

experimental data. Part of the problem may have been that it did not include a mechanism for determining conversion to CaSO_4 or SO_2 concentration at a given radius within the particle. The grain core radius should be a function of the radial location within the particle. A more detailed analysis of this model is found in Christofides [13].

The current model being employed in this study is a shrinking particle core model with an exponential decay of diffusivity. The model assumes reaction at particle core surfaces, which is common for reactions that are controlled by diffusion into the particle. It does not consider a mechanism at the grain level, i.e., product layer diffusion. Therefore, the model loses some of the detail of mechanistic models, but retains the simplicity of being solved by a series of ordinary differential equations:

$$\frac{d[\text{SO}_2]_R}{dt} = \frac{Q}{V_b} \{[\text{SO}_2]_I - [\text{SO}_2]_R\} - h_s a_p \frac{N_p}{V_b} \{[\text{SO}_2]_R - [\text{SO}_2]_S\} \quad (3.50)$$

$$\frac{d[\text{SO}_2]_S}{dt} = \frac{h_s a_p}{V_F} \{[\text{SO}_2]_R - [\text{SO}_2]_S\} - \frac{4\pi D_{es} e^{-t/\tau_p}}{V_F \left(\frac{1}{r_{pc}} - \frac{1}{r_p} \right)} \{[\text{SO}_2]_S - [\text{SO}_2]_{SC}\} \quad (3.51)$$

$$\frac{d[\text{SO}_2]_{SC}}{dt} = \frac{4\pi D_{es} e^{-t/\tau_p}}{V_L \left(\frac{1}{r_{sc}} - \frac{1}{r_p} \right)} \{[\text{SO}_2]_S - [\text{SO}_2]_{SC}\} - \frac{k_S a_{pc}}{V_L} [\text{SO}_2]_{SC} \quad (3.52)$$

$$\frac{dr_{sc}}{dt} = - \frac{k_S M_{\text{CaO}}}{\rho_{\text{CaO}}} [\text{SO}_2]_{SC} \quad (3.53)$$

As in calcination, a quasi-steady approximation is applied to this model and time derivatives of $[\text{SO}_2]$ are set equal to zero. The model then simplifies to one ordinary differential equation and one algebraic equation:

$$-\frac{dr_{sc}}{dt} = \frac{[SO_2]_I \frac{M_{CaO}}{f_{CaO} \rho_{LS}}}{\frac{3m_{LS}}{Q\rho_{LS}r_p} \frac{r_{sc}^2}{r_p^2} + \frac{1}{h_s} \frac{r_{sc}^2}{r_p^2} + \frac{(r_p - r_{sc})r_{sc}}{D_{es}e^{-t/\tau_p} r_p} + \frac{1}{k_s}} \quad (3.54)$$

$$\frac{[SO_2]_R}{[SO_2]_I} = \frac{1}{1 + \frac{3m_{LS}}{Q\rho_{LS}r_p} \left(\frac{1}{\frac{1}{h_s} + \frac{(r_p - r_{sc})r_p}{D_{es}e^{-t/\tau_p} r_{sc}} + \frac{1}{k_s} \frac{r_p^2}{r_{sc}^2}} \right)} \quad (3.55)$$

This model, like that for calcination, can be extended to non-spherical particles with a shape factor, S , and a characteristic length, L . With these modifications, and defining ξ_s equal to r_{sc}/r_p , Eqns. (3.54) and (3.55) become:

$$-\frac{d\xi_s}{dt} = \frac{[SO_2]_I \frac{M_{CaO}}{f_{CaO} \rho_{LS} L}}{\frac{Sm_{LS}}{Q\rho_{LS}L} \xi_s^{(S-1)} + \frac{1}{h_s} \xi_s^{(S-1)} + \frac{L(1-\xi_s)\xi_s^{(S-1)/2}}{D_{es}e^{-t/\tau_p}} + \frac{1}{k_s}} \quad (3.56)$$

$$\frac{[SO_2]_R}{[SO_2]_I} = \frac{1}{1 + \frac{Sm_{LS}}{Q\rho_{LS}L} \left(\frac{1}{\frac{1}{h_s} + \frac{L(1-\xi_s)}{D_{es}e^{-t/\tau_p} \xi_s^{(S-1)/2}} + \frac{1}{k_s \xi_s^{(S-1)}}} \right)} \quad (3.57)$$

If one of the resistances in Eqns (3.56) and (3.57) is considerably larger than the others, then limiting behavior is observed. At time zero, the pore diffusion resistance is zero, since r_p and r_{sc} coincide. Accordingly, for early times in the transient, sulfation is controlled either by the chemical reaction or film diffusion. At later times the pore diffusion

resistance becomes infinite and pore diffusion is rate-limiting. For cases where the film diffusion and chemical reaction resistances are small throughout the reaction, Eqn. (3.55) becomes:

$$\frac{[SO_2]_R}{[SO_2]_I} = \frac{1}{1 + \frac{3m_{LS}}{Q\rho_{LS}r_p} \left(\frac{r_{sc}D_{es}}{(r_p - r_{sc})r_p} \right) e^{-t/\tau_p}} \quad (3.58)$$

which is similar to the result derived by Zheng *et al.* [42], except the chemical reaction rate is replaced by a pore diffusion term.

3.3.2 Model simplification resulting from limiting behavior

An objective of this investigation is to find time constants to characterize sorbent reactions analytically through time series or spectral methods. The shrinking core model with decaying diffusivity as shown in Eqns. (3.56) and (3.57) is useful in analyzing the transients, but comparison must be done numerically. The model can be simplified further by assuming rate-limiting mechanisms. To simplify the expressions, two constants are defined: $c_{1s} = [SO_2]_I M_{CaO} / f_{CaO} \rho_{CaO}$, and $c_2 = 3m_{LS} / \rho_{LS} Q$. For the present discussion, analysis will be for spheres unless otherwise indicated.

3.3.2.a Chemical reaction control

If chemical reaction is the controlling mechanism, the chemical reaction resistance term in Eqns. (3.56) and (3.57) is larger than the other resistances so that the equations may be rewritten:

$$-\frac{d\xi_s}{dt} = \frac{c_{1s}}{L} k_s \quad (3.59)$$

$$\frac{[SO_2]_R}{[SO_2]_I} = \frac{1}{1 + \frac{c_2}{L} k_s \xi^2} \quad (3.60)$$

Equation (3.59) can be integrated directly to yield:

$$\xi_s = 1 - \frac{c_1 s}{L} k_s t \quad (3.61)$$

which is the first two terms of the Taylor series expansion for the exponential function.

Consequently, for short times ξ_s may be approximated by:

$$\xi_s = e^{-t / \tau_{sk}^*} \quad (3.62)$$

where $\tau_{sk}^* = L/k_s c_1 s$. Substituting this result into Eqn. (3.60) and inverting the equation results in:

$$\frac{[SO_2]_I}{[SO_2]_R} - 1 = \frac{c_2}{L} k_s e^{-2t / \tau_{sk}^*} \quad (3.63)$$

Recognizing that $[SO_2]_R$ is equal to $[SO_2]_O$ at time zero, the equation takes on the form:

$$\frac{\frac{[SO_2]_I}{[SO_2]_R} - 1}{\frac{[SO_2]_I}{[SO_2]_O} - 1} = e^{-t / \tau_{sk}} \quad (3.64)$$

where $\tau_{sk} = \tau_{sk}^* / 2 = r_p / 2 k_s c_1 s = L / (S-1) k_s c_1 s$.

The sulfation time constant, τ_s can be determined graphically from the slope of a log-linear plot of Eqn. (3.64). If chemistry is rate limiting, τ_s will vary directly with particle size and inversely with the chemical reaction rate coefficient and inlet SO_2 concentration. A plot of $1/\tau_s$ versus $1/T$ will yield the true activation energy for chemistry reaction controlled sulfation. If particle shapes other than spheres are used, τ_s will be proportional to $\tau_{sk}/(S-1)$. For flat plates this results in an infinite value for τ_s , corresponding to a constant outlet concentration. For every shape, chemistry control results in an interface that recedes at a constant rate.

3.3.2.b Film diffusion control

If sulfation is controlled by diffusion through the gas film surrounding the particle, the film diffusion resistances will be much larger than the other resistances. For the film diffusion control case, Eqns (3.56) and (3.57) become:

$$-\frac{d\xi_s}{dt} = \frac{c_{1s} h_s}{L \xi_s^2} \quad (3.65)$$

$$\frac{[\text{SO}_2]_R}{[\text{SO}_2]_I} = \frac{1}{1 + \frac{c_2}{L} h_s} \quad (3.66)$$

Integration of Eqn. (3.65) and application of the Taylor series expansion of the exponential function result in:

$$\xi_s = e^{-t/\tau_{sh}} \quad (3.67)$$

where $\tau_{sh} = L/h_s c_{1s}$. Equation (3.66) shows that the concentration transient is constant with

time for film diffusion control. This response has not been observed in laboratory experiments nor in the literature. Although film diffusion may play a role in the sulfation process, it does not act as the sole controlling mechanism.

3.3.2.c Pore diffusion control

Up to this point the model under consideration has had an exponentially decaying diffusivity. To illustrate the effect of pore diffusion control, the sulfation mechanism will be examined first with a constant diffusivity, and then a decaying term will be incorporated in section 3.3.2.d. Analysis for pore-diffusion control and pore-plugging control is done for flat plates, utilizing the inherently simpler mathematics for this shape. Flat plate analysis is a particularly reasonable approach if pore-plugging occurs before a large shell of CaSO_4 builds up.

For pore diffusion control with an effective diffusivity which is constant with time and radius, Eqn. (3.56) becomes:

$$-\frac{d\xi_s}{dt} = \frac{D_{es}c_{1s}}{L^2(1-\xi_s)} \quad (3.68)$$

Integration of Eqn. (3.68) yields:

$$(1-\xi_s)^2 = \frac{2D_{es}c_{1s}}{L^2}t = t/t_s \quad (3.69)$$

where t_s , the time to completely sulfate the particle, is $L^2/(2D_{es}c_{1s})$. The expression for the dimensionless core radius is:

$$\xi_s = 1 - \sqrt{\frac{t}{t_s}} \quad (3.70)$$

The sulfation transient for pore diffusion limitation can be analyzed by writing Eqn. (3.57) for pore diffusion control:

$$\frac{[SO_2]_I}{[SO_2]_R} - 1 = \frac{c_2 D_{es}}{L^2 (1 - \xi_s)} \quad (3.71)$$

Inversion and substitution of Eqn. (3.70) into Eqn. (3.71) yields:

$$\left(\frac{[SO_2]_I}{[SO_2]_R} - 1 \right)^{-1} = \left(\frac{[SO_2]_I}{[SO_2]_I - [SO_2]_R} - 1 \right) = \frac{L^2}{c_2 D_{es}} \sqrt{\frac{t}{t_s}} = \sqrt{\frac{t}{\tau_{sd}}} \quad (3.72)$$

where $\tau_{sd} = c_2^2 D_{es} / 2c_{1s} L^2$. By making use of a Taylor series approximation, the linearized equation for short times is:

$$\left(\frac{[SO_2]_I}{[SO_2]_I - [SO_2]_R} \right) = 1 + \left(\frac{t}{\tau_{sd}} \right)^{1/2} = e^{\sqrt{t/\tau_{sd}}} \quad (3.73)$$

Inverting once more results in:

$$1 - \frac{[SO_2]_R}{[SO_2]_I} = e^{-\sqrt{t/\tau_{sd}}} \quad (3.74)$$

The sulfation time constant, τ_{sd} , can be determined from the reciprocal slope of a “log-squared”-linear plot:

$$\left\{ \ln \left(1 - \frac{[SO_2]_R}{[SO_2]_I} \right) \right\}^2 = \frac{1}{\tau_{sd}} t \quad (3.75)$$

Alternatively, Eqn. (3.72) results in a simple expression:

$$\left(\frac{[SO_2]_I}{[SO_2]_R} - 1 \right)^{-2} = \frac{1}{\tau_{sd}} t \quad (3.76)$$

which is valid for all times and can be plotted directly to fit a value of τ_{sd} .

3.3.2.d Pore plugging control

The model described in Eqns. (3.56) and (3.57) incorporates an exponential decay in the effective diffusivity. Sulfation may be limited, not by the initial pore diffusion resistance, but by the effects of pore plugging. An exponential decay in diffusivity is used as an empirical model to describe pore plugging. Other investigators [36, 37] have used the local conversion at the grain or micro-grain level to drive the change in effective diffusivity. In this investigation, the pore-plugging time constant, τ_p , is an empirical parameter useful in assessing the rate-limiting mechanism of sulfation. For pore-plugging control of flat plates, Eqn. (3.56) can be written as:

$$-\frac{d\xi_s}{dt} = \frac{c_{is} D_{es} e^{-\nu \tau_p}}{L^2 (1 - \xi_s)} \quad (3.77)$$

Integration of Eqn. (3.77) yields:

$$(1 - \xi_s)^2 = \frac{\tau_p}{t_s} \left(1 - e^{-\frac{t}{\tau_p}} \right) \quad (3.78)$$

so that the dimensionless core radius is:

$$\xi = 1 - \sqrt{\frac{\tau_p}{t_s} \left(1 - e^{-\frac{t}{\tau_p}} \right)} \quad (3.79)$$

The significance of Eqn. (3.79) is that it predicts a final sulfation layer thickness. At late times, the thickness of the layer is $L\sqrt{\tau_p/t_s}$. Since the time for total sulfation, t_s , is a function of L^2 , the ultimate layer thickness for pore-plugging control is independent of particle size.

Analysis of the sulfation transient for pore plugging control can be made by assuming that pore-plugging is the limiting resistance in Eqn. (3.57). This results in the expression:

$$\frac{[SO_2]_I}{[SO_2]_R} - 1 = \frac{c_2 D_{es} e^{-\frac{t}{\tau_p}}}{L^2 (1 - \xi_s)} \quad (3.80)$$

Direct substitution of Eqn. (3.79) into Eqn. (3.80) gives:

$$\frac{[SO_2]_I}{[SO_2]_R} - 1 = \frac{c_2 D_{es} e^{-\frac{t}{\tau_p}}}{L^2 \left\{ 1 - \left[1 - \sqrt{\frac{\tau_p}{t_s} \left(1 - e^{-\frac{t}{\tau_p}} \right)} \right] \right\}} \quad (3.81)$$

For early times, the Taylor series expansion for e^{-t/τ_p} allows the simplification of Eqn. (3.81) to:

$$\frac{[SO_2]_I}{[SO_2]_R} - 1 = \frac{c_2 D_{es} e^{-\frac{t}{\tau_p}}}{L^2 \sqrt{\frac{t}{t_s}}} \quad (3.82)$$

At early times in the reaction, e^{-t/τ_p} is close to unity and the equation then becomes the parabolic equation for pore diffusion control, Eqn. (3.76). At very late times in the reaction, the denominator of Eqn. (3.82) becomes a constant relative to the numerator. At these late times the transient approaches the background exponentially with the pore-plugging time constant. Thus, at long times, a log-linear plot of Eqn. (3.82) will give the pore-plugging time constant.

The end of the transient presents some experimental difficulties, however. Small fluctuations are magnified on a log-linear plot as the background concentration is approached. Additionally, small changes in background concentration affect the analysis by changing the estimated value of $[SO_2]_I$. An alternative method is to measure τ_p early in the transient by plotting:

$$-\ln\left\{\left(\frac{[\text{SO}_2]_I}{[\text{SO}_2]_R} - 1\right)\sqrt{t}\right\} = \frac{1}{\tau_p}t - \ln\left\{\frac{c_2}{L}\sqrt{\frac{D_{es}}{2c_{1s}}}\right\} = \frac{1}{\tau_p}t - \ln\sqrt{\tau_{sd}} \quad (3.83)$$

which gives a line with a slope of $1/\tau_p$. The intercept of this line can be used to find the constant diffusivity time constant, τ_{sd} , and also the value of D_{es} .

3.3.2.e Bulk mass transfer control

If bulk mass transfer is the controlling mechanism, the bed mixing resistance ($3m_{LS}/\rho_{LS}Qr_p$) is significantly larger than the other resistances. For this case Eqn. (3.56) can be written:

$$-\frac{d\xi_s}{dt} = \frac{c_1 S}{c_2 \xi_s^2} \quad (3.84)$$

Integrating and using the Taylor series expansion for the exponential function, Eqn. (3.84) becomes:

$$\xi_s = e^{-t/\tau_{sb}} \quad (3.85)$$

where $\tau_{sb} = c_2/c_{1s}$. Simplification of Eqn. (3.57) for film diffusion control results in:

$$\frac{[\text{SO}_2]_R}{[\text{SO}_2]_I} = \frac{1}{1 + \frac{c_2}{L}K(t)} \quad (3.86)$$

In Eqn. (3.86), $K(t)$ is the overall reaction coefficient from the other resistances. Since the chemical and diffusion resistance terms are time dependent, $K(t)$ is written as a function of

time. This allows for consideration of two cases in which bulk mass transfer is the primary controlling mechanism and either chemical reaction resistance or pore diffusion resistance is the secondary controlling mechanism.

For the case in which chemical reaction is the secondary mechanism, resistances of film mass transfer and pore diffusion are neglected. By substituting $1/R_{\text{chem}}$ into Eqn. (3.86) for $K(t)$, and combining with the expression for ξ in Eqn. (3.85), an expression for the transient is written as;

$$\frac{[SO_2]_R}{[SO_2]_I} = \frac{1}{1 + \frac{c_2}{L} k e^{-2t/\tau_{sb}}} \quad (3.87)$$

By applying the condition that $[SO_2]_R$ is equal to $[SO_2]_O$ at time zero, the resulting expression can be written:

$$\frac{\frac{[SO_2]_I - 1}{[SO_2]_R} - 1}{\frac{[SO_2]_I - 1}{[SO_2]_O}} = e^{-t/\tau_s} \quad (3.88)$$

where $\tau_s = \tau_{sb}/2 = c_2/(S-1)c_{1s}$. This represents a case where the time constant is independent of r_p and k_s , even though the chemical reaction is the only mechanism considered other than bulk mass transfer.

If pore diffusion is the secondary mechanism, and a flat plate is considered, Eqn. (3.86) becomes,

$$\frac{[SO_2]_R}{[SO_2]_I} = \frac{1}{1 + \frac{c_2}{L^2} \frac{D_{es}}{(1-\xi_s)}} \quad (3.89)$$

Substitution of the dimensionless core radius from Eqn. (3.58) results in:

$$\left(\frac{[SO_2]_I}{[SO_2]_R} - 1 \right)^{-1} = \frac{c_1 S L^2}{c_2^2 D_{es}} t \quad (3.90)$$

For early times, the equation may be written as:

$$-\ln \left(\frac{[SO_2]_I - [SO_2]_R}{[SO_2]_I - [SO_2]_O} \right) = \frac{1}{2\tau_{sd}} t \quad (3.91)$$

If a decaying value of diffusivity is considered, the equation becomes:

$$\left(\frac{[SO_2]_I}{[SO_2]_R} - 1 \right) = \frac{c_2 D_{es} e^{-t/\tau_p}}{L^2 (1 - e^{-t/\tau_{sb}})} \quad (3.92)$$

which for early times reduces to the pore diffusion case of (3.91). For later times the response approaches background at the pore-plugging time constant.

As in calcination, bulk mass transfer may affect the reaction, but its effect will depend upon the relative strengths of the other mechanisms. For sulfation ordinarily controlled by chemical reaction, bulk mass transfer changes the time constant such that it is no longer dependent upon particle size or chemical reaction rate. For pore diffusion, it doubles the sulfation time constant, and changes the order of the response. For pore plugging, the difference is only in the initial part of the transient. At early times the transient is described by the linear pore diffusion response of Eqn. (3.90).

4. EXPERIMENTAL APPARATUS

4.1 Laboratory Equipment

A diagram of laboratory scale equipment is given as Fig. 4.1. The laboratory scale fluidized-bed combustor (FBC) has a diameter of 20 cm. Five liters of sand with particle diameters ranging from 0.6 to 1.2 mm were used to make a bed approximately 15 cm in height. For sulfation experiments the sand was a 99% pure silica sand obtained from the Badger Mining Corporation of Fairwater, Wisconsin. This was obtained to eliminate any possible effects due to carbonates in the local river sand. A mixture of fuel and air fluidized the sand after passing through a diffuser plate consisting of 166 holes of 2.4 mm diameter, spaced 1.4 cm apart in a square grid.

The primary fuel was methane from the building natural gas lines, but propane from 20 pound cylinders was used initially and during some of the later sorbent testing. Combustion air was provided from the building compressed air lines. Pressure upstream of the air flow meter was regulated to 60 psia during flow meter calibration and operation. Air flow is measured via a Shaevitz p3061 linear-variable-differential transformer (LVDT) differential pressure transducer. Compensation for the zero shift on the pressure transducer is available within the data acquisition code. Air flow is controlled either by a manual valve or by the data acquisition system via a pneumatically-controlled Fisher Design air flow valve with a Fisher Type 513 R reversible diaphragm actuator. Calibration was done using a standard wet test flow meter manufactured by the American Meter Co. of New York. The error for this calibration is approximately 5% of full scale.

For sorbent testing SO_2 is introduced to the air upstream of the distributor plenum. Ignition of the air and natural gas is achieved above the bed via two electrodes connected to a 10 kV transformer. Temperatures are measured by type K thermocouple probes in the center and side of the bed. Thermocouples also were used to record

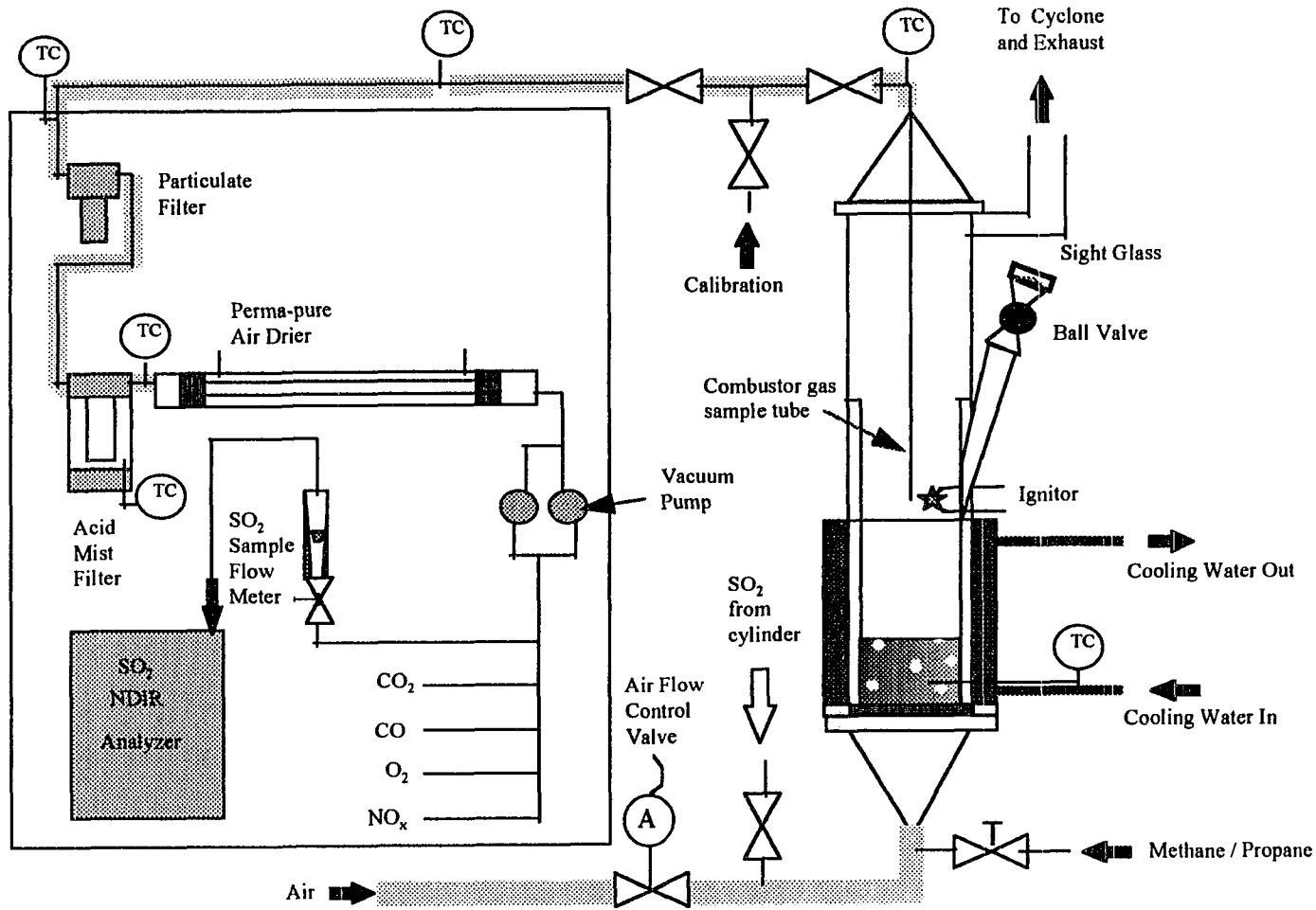


Figure 4.1 Schematic of laboratory combustor and instrumentation

temperatures in the lower and upper sections of the freeboard. The thermocouples provide an accuracy of $\pm 6^\circ$ C. Exiting combustion gases passed through a cyclone separator where elutriated particles were removed.

4.2 Laboratory Instrumentation

The gas was sampled at two locations and drawn through one of two sample lines by a common double diaphragm vacuum pump. The initial sample location was in the exhaust line after the cyclone separator. This sample passed through a Balston 30/12 microfibre filter to remove small particulates and a Perma-Pure F-275-EG acid mist filter. Water vapor is removed from the sample gas by a Perma-Pure PD625-24APS membrane dryer. The sample gas flows through fifty 0.5 mm diameter organic semi-permeable membrane tubes. Dry air from a Perma-Pure HD202-b heatless zeolite dryer passes over the outside of the membranes inside the stainless steel tube. Because of a differential water vapor pressure gradient, moisture from the gas flows through the semi-permeable tubes into the dry purge air. This sample line is used when coal combustion is the means of steady-state combustion. A condensing tar trap is used in this situation to remove tars from the gas before it contacts the sample cart equipment.

The second sample line is the same as the first except that it draws from the freeboard of the combustor. It also uses a smaller Balston model 9556 filter and a smaller Perma-pure model FF-250-SG-2.5G acid mist filter. The Perma-Pure PD1000 membrane dryer has two hundred 0.5 mm diameter membranes for increased moisture removal. This sample line is used for long-term combustion of methane or propane due to the higher water vapor content in the product gases. Both sample lines are heated electrically with heat tapes to maintain combustion gases well above local dew point temperatures.

The sample system has type K thermocouples that are connected to the data acquisition system to monitor sample system component temperatures. The pump and heat

tapes are programmed to shut down if temperatures at the Perma-pure or acid mist filter exceed 200°F in order to protect the Perma-pure gas dryer elements.

The gas is directed from the vacuum pump to five gas analysis instruments. Measurements for SO₂ and NO_x are made on Horiba VIA-500 and VIA-300 non-dispersive infrared instruments. Compensation for water vapor interference is available in the VIA-500 instrument. The CO and CO₂ instruments are Beckman 870 infrared analyzers. The oxygen instrument is a paramagnetic instrument. Instruments were calibrated against certified blend gases obtained from Air Products, Inc. of Allentown, PA. These gases are certified to be within ±2% of the calibration value. Analyzer drifts and calibration gas concentrations are given in Table 4.1.

Table 4.1 Gas analyzer equipment and associated accuracies

Gas	Analyzer	Full scale conc.	Drift (on a 24 hour basis)	Calibration gas	Repeatability
O ₂	Beckman 755 O ₂ analyzer	25%	1% of full scale	8.10% O ₂ in nitrogen	1% of full scale
CO ₂	Beckman 870 CO ₂ analyzer	20%	1% of full scale	15.0% CO ₂ in nitrogen	1% of full scale
CO	Beckman 870 CO analyzer	1.2%	1% of full scale	0.80% CO in nitrogen	1% of full scale
NO _x	Horiba VIA-300 NO _x analyzer	1000 ppm	1% of full scale	800 ppm NO in nitrogen	1% of full scale
SO ₂	Horiba VIA-500 SO ₂ analyzer	2000 ppm	1% of full scale	1490 ppm SO ₂ in nitrogen	1% of full scale

The data acquisition system consists of an HP Vectra 386 SX-16 computer configured with a Metrabyte 8 channel type DAS-8 A/D converter. Temperatures, gas concentrations air flow and bed differential pressure are monitored by the system. The type-K thermocouples are connected to two Metrabyte Model EXP-16 sub-multiplexer boards provided with a cold junction compensation. These signals are amplified to provide a 0-5 VDC signal to the DAS-8 converter. The DAS-8 also receives 0-5 V DC signals

directly from the gas analyzers and from the air flow transducer. Control functions such as air flow and feed flow control, and automatic shutdown of gas analysis equipment are used as needed. The operating code is written in QuickBASIC 7 and converted into executable files. Data was recorded at a rate appropriate to the transient being measured. The maximum data rate was 7 data points per second.

4.3 Power Plant Equipment

Tests were conducted on Boiler #2 at the ISU Power plant. A schematic of this boiler is shown in Fig. 4.2. This boiler is a coal-burning, circulating FBC which is approximately 5 m by 5 m square in cross section with a furnace section 23 m tall. Coal is fed at a design feed rate of 24,000 lb/hr (10.9 metric tons/hr). Limestone is also continuously supplied at a design rate of 8000 lb/hr (3.6 metric tons/hr). Total air flow can exceed 200,000 lb/hr (90.8 metric tons/hr) resulting in superficial velocities between 4 and 5 m/s. Temperatures in the bed range from 1123 K to 1173 K.

Air is divided between primary air, which enters at the bottom of the combustor, and secondary air which enters about 2 m above the primary air nozzles. Solids with a diameter smaller than approximately 250 μm enter the cyclone separator. Those smaller than approximately 100 μm pass on with the combustion gases through the heat exchangers, and are trapped in the bag house before the gases exit through the stack. Particles between 100 and 250 μm are returned to the combustor via a loop seal.

A tank to hold batches of coal and limestone was added at the coal addition port that emptied directly into the bed. Coal from this addition port enters the combustor about 1.5 m above the nozzles. A knife valve can be quickly opened to allow up to 100 lb (45 kg) of limestone to instantaneously enter the bed as a batch. Further details of the power plant, including economic analysis and the start up history can be found in Miller *et al.* [46].

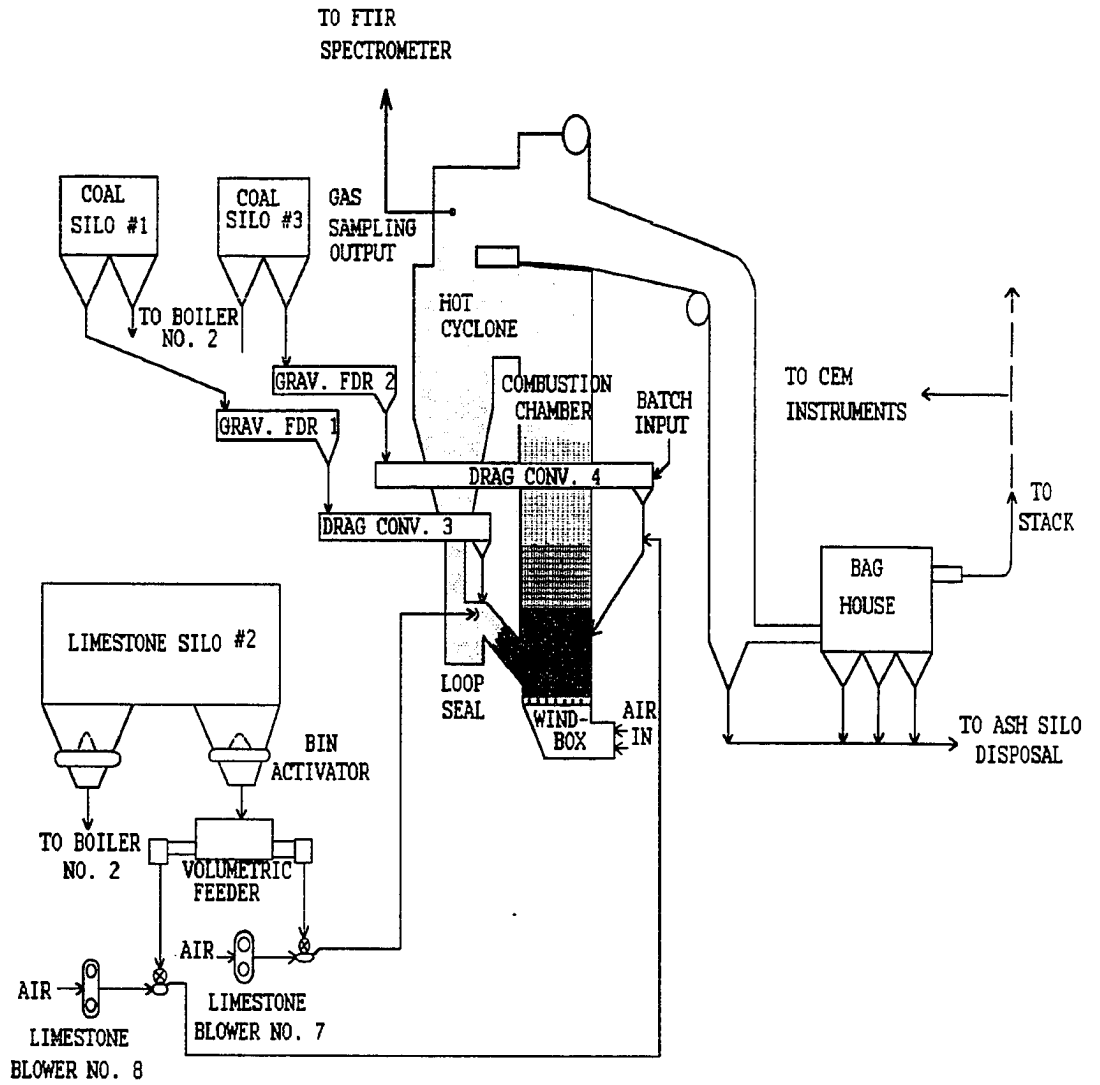


Figure 4.2 Schematic of boiler #2 at ISU power plant [47]

Raines [47] presents a detailed description of the equipment for conducting batch testing and the operation of power plant instrumentation.

4.4 Power Plant Instrumentation

Continuous gas sampling was conducted during tests at the power plant using a Magna 550 Fourier Transform Infrared (FTIR) analyzer from Nicolet Instrument Systems, Inc. This instrument was chosen to provide a continuous measurement of multiple gases. Detection is made through a Infrared Analysis, Inc. model G-2-4-H-BA-Au 20-pass gas cell. This cell has a short 1.7 m pathlength and a volume of 275 ml. This design has a somewhat lower sensitivity than other models, but allows for rapid data collection. A data rate of 1 data point every 1.03 seconds is used to provide a resolution of 2 cm^{-1} with 2 scans per second.

A 1.2 m long, 1.27 cm diameter sample probe extends through a port in the cyclone outlet duct. Gas is extracted from the cyclone using a Thomas model 2737-CM vacuum pump, located downstream of the sample line and FTIR instrument. The sample line contains Balston particulate filters and a perma-pure gas dryer similar to those in the laboratory. The cell temperature is maintained at $82.2\text{ }^{\circ}\text{C}$ by a Barnant model 621-8600 temperature controller with a type J thermocouple. Pressure in the cell was maintained by a needle valve on the vacuum pump to a cell pressure of $600 \pm 6\text{ mm Hg}$.

4.5 Particle Analysis Equipment

Samples were analyzed on a Hitachi model S-2460N Scanning Electron Microscope (SEM). This SEM produced particle concentration maps which were used to evaluate the location of calcined and sulfated regions in the limestone particles. Microprobe line scanning was also done using this instrument to measure sulfation layer thicknesses and concentration gradients. Sulfated particles were made into thin sections for transmitted-

light microscopy. This analysis provided an indication of particle grain size. Chemical analyses were performed on limestone and sulfated samples by X-ray fluorescence (XRF) for comparison of actual conversion to that determined from transient gas analysis.

5. MATERIALS AND METHODS

5.1 Characteristics of Tested Sorbents

Sorbent testing was done on three limestones. A large majority of the testing was done using limestone from the Gilmore City formation which was obtained from the I.S.U. power plant. This limestone is a coarse, moderately porous limestone of an intermediate to old geological age, i.e. the Mississippian, or lower Carboniferous geological period. A chemical analysis of the three limestones is given in Table 5.1. Chemical analyses were done on two sizes of Gilmore City formation limestone to check for any differences attributable to the crushing process. Limestone was sized using Tyler U.S.A. series sieves into sizes ranging from 0.125 to 4.75 mm. A size distribution analysis for the Gilmore City limestone as delivered to the power plant is shown in Fig. 5.1. The Gilmore City limestone

Table 5.1 Chemical analysis of limestones used

	Gilmore City Formation 1993	Gilmore City Formation 1995, Dp = 1.85 mm	Gilmore City Formation, 1995, Dp = 0.328 mm	Cedar Bay #1, 1995 Dp = .55 mm	Nova Scotia, 1995 Dp = 0.55 mm
SrO		0.02	0.02	0.07	0.03
MgO	1.15	0.78	0.42	0.35	0.52
Fe ₂ O ₃	0.24	0.21	0.15	0.01	0.27
K ₂ O	0.01	0.02	0.02	0.01	0.24
SO ₃	0.56	0.01	0.01	0.03	0.04
TiO ₂	0.03	0.01	0.01	0.01	0.05
MnO	0.01	0.02	0.02	0.01	0.07
SiO ₂	1.17	0.96	0.34	0.13	4.17
CaO	53.86	54.00	55.12	54.72	50.71
P ₂ O ₅	0.06	0.01	00.00	0.01	0.01
Al ₂ O ₃	0.60	0.06	0.07	0.07	0.98
Sum	57.69	56.10	56.18	55.42	57.09
% calcite	96.17	96.42	98.42	97.71	90.55

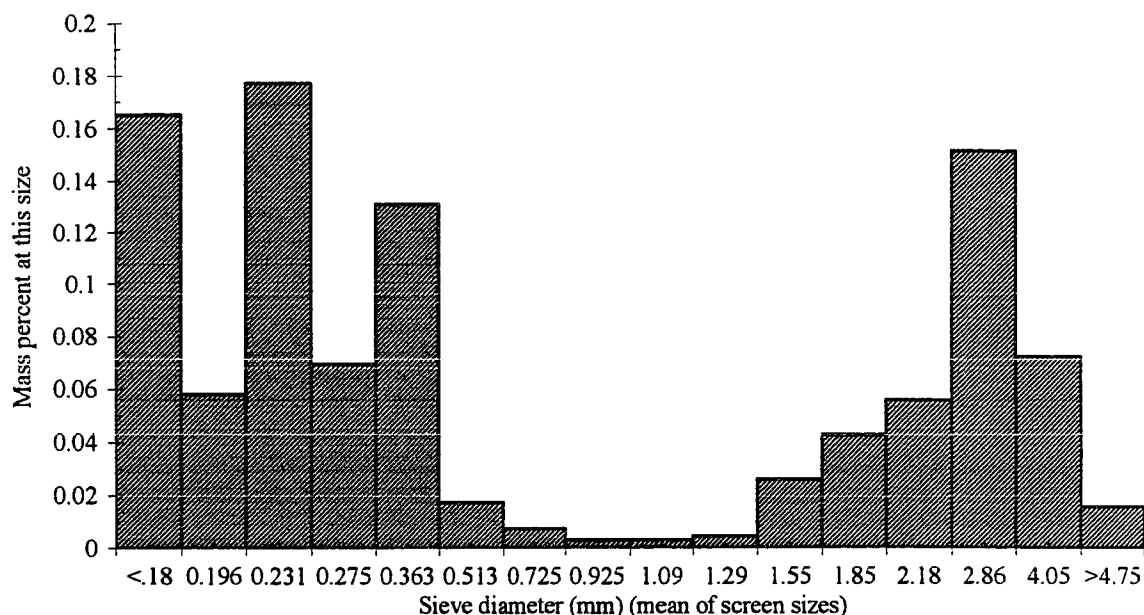


Figure 5.1 Size distribution of power plant limestone.

was also separated into three color groups to compare the variation in sorbent performance within a single limestone type.

Transmitted light reveals some of the unique structure of the Gilmore City limestone. Figure 5.2 shows the grain structure of unreacted limestone in cross-polarized light. The concentric ellipses, which are about 0.5 mm in diameter, are not particles, but oolites within the particle. Oolites are formed by deposits of aragonite and calcite over a grain nucleus in the turbulence of ancient shallow sea beds. At some point these structures were cemented together by a calcite deposit which can be seen in the interstices of the oolites.

In Fig. 5.2.b the platform of the microscope is slightly rotated from its position in Fig. 5.2.a. When this occurs some of the regions of the cementing calcite change from white to black. This extinction phenomenon indicates that the crystal structure in the extinguishing area is aligned, and that the region behaves as a large grain. It is hypothesized that this oolitic structure could be the cause of the gap in the particle size distribution



a. Oolites in cross polarized light before rotation of microscope platform



b. Oolites after rotation of platform in cross polarized light. Circle highlights extinction.

Figure 5.2 Internal structure of Gilmore City formation limestone

shown in Fig. 5.1. Additionally, SEM maps show that SO₂ diffuses in cracks around the oolites near the surface of the particle.

A set of tests were run for particle analysis with the Gilmore City limestone separated into color groups. Limestone was sifted to a 2.58 mm size, washed to enhance its color, and then separated by hand. Batches of 150 g. were tested in the laboratory combustor, with particles extracted after 2, 8, 16, 40, and 80 minutes. Transient emissions were analyzed during this procedure and samples were polished in epoxy rings.

5.2 Test Procedures

In general, limestone was used for the tests, but for several testing applications calcined limestone (lime) was used. To prepare the lime, limestone particles of substantially larger size than the sand were batched into the bed. The laboratory combustor was at the prescribed operating temperature and burning natural gas in the absence of SO₂ injection. After calcination was complete the bed was quickly cooled and the bed material was removed from the combustor. The particles were removed from the bed using a size 14 USA standard sieve. Some of these calcined particles were analyzed for surface area and pore size distribution of the calcine. After weighing the recovered mass, the limestone particles were used for sulfation tests.

Two methods were used for drawing calibration gases. In the first method samples were drawn from a break in the sample line via Tygon tubing from the cylinders. A plastic bag was placed in series with the Tygon tubing to ensure that the samples were drawn from approximately atmospheric pressure. In the second method, Tygon tubing was placed at a hose barb at the start of the sample line. Cylinder regulators were adjusted to ensure that the flow rate from the cylinders was the same as when the system was drawing sample gases. It was assumed that equal flows into the instruments resulted in equal pressure in the instruments. The second method had the advantage that step tests could be performed

through an installed valve manifold by instantaneously switching between calibration gases. This provided a reliable way of determining instrument delay time.

Instrument time constants for the analyzers were determined by performing step tests of the calibration gas and nitrogen. Gas flow into the instruments was controlled by flow meters to the recommended rates of 1.0 l/min for the CO₂, CO, SO₂, and NO_x instruments, and 0.5 l/min for the O₂ instrument. An increased flow rate of 3 l/min was used in later experiments for the SO₂ instrument to decrease the instrument lag time. Lag times for the CO₂, CO, and O₂ gas analyzers were matched to an exponential step change; e.g. for a step decrease:

$$C_A = C_{A_{\max}} e^{-t/\tau_i} \quad (5.1)$$

For CO and CO₂ the instrument lag time, τ_i , was roughly 2 seconds, while for O₂ it was around 10 seconds.

For most of the sorbent data, SO₂ instrument flow was the recommended 1 l/min. The instrument lag time under this condition was best represented by the following expression:

$$\frac{[SO_2]_R}{[SO_2]_I} = 0.96e^{-t/6.5} + 0.04e^{-t/200} \quad (5.2)$$

This unusual response is presumed to be due to adsorption and subsequent desorption of SO₂ in materials of the filter elements. This representation of the instrument lag time was used in the form of two differential equations to fit transient emission data to the sulfation model during computer simulations. An appreciation of the long time to reach a steady background was also important in properly calibrating the SO₂ instrument. For later tests

the flow rate through the SO₂ instrument was increased to 3 l/min. With the decreased residence time in the sample system, the instrument response was best described by Eqn (5.1) with an instrument lag time of 2 seconds.

Batch tests were conducted by heating the bed to the desired temperature and then adjusting fuel and air flow to obtain the flow rate desired. For coal tests the standard baseline conditions were a bed temperature of 850°C and a flow rate of 1 m/s. At these conditions, using propane, the oxygen level measured in the analyzer was 6-7% and the background CO₂ level measured by its analyzer was 7-8%. When using methane, the background oxygen concentration was 4-5%. An analytical compensation for water vapor removed during the sampling process was made to the concentrations measured by the instruments. This was accomplished by assuming complete combustion of methane and 100% water removal in the perma-pure. Using these assumptions and the mole fraction of CO₂ measured at the instrument, the correction factor is expressed as,

$$X_{\text{gas, actual}} = \frac{X_{\text{gas, measured}}}{1 + 2X_{\text{CO}_2, \text{measured}}}, \quad (5.3)$$

This correction typically equated to a 15% difference in the magnitude of the gas concentrations, and extents of reaction. The assumptions of complete combustion and complete water vapor removal were used, along with an ideal gas compensation for temperature, to estimate actual concentrations and superficial velocity. These compensations were less critical when measuring concentration ratios for the time constants, but were important in the determination of extents of calcination and sulfation.

For sulfation tests pure SO₂ was injected via a small needle valve to control SO₂ background levels to within ±10 ppm as read on the data acquisition computer. Fuel, air, and SO₂ flows were then left to steady for 30 minutes to an hour prior to the start of the

first test on a given day. This time period was the minimum required to bring temperature and SO₂ concentration to steady-state. A wide variety of conditions were used for these tests but a baseline condition was a bed temperature of 850°C, a superficial velocity of 1 m/s, and a background SO₂ concentration of 1500 ppm as measured by the SO₂ instrument. Nitrogen and CO₂ were sometimes added to the air line to test the effects of variations in oxygen and CO₂ concentrations.

The data acquisition program was initiated prior to starting the test. At least 30 seconds of data was recorded to verify that the background was steady. For sulfation tests 2 minutes of data were recorded prior to batching in the limestone. The samples were weighed using a Fisher Scientific Model XT-660-KT balance which has a range of 0 to 660 grams and a sensitivity of 0.01 grams. For coal tests the standard sample mass was 5 grams. A 20 or 30 gram sample was typically used for sorbent tests, but other batch sizes were used when samples were to be extracted from the bed in the middle of the test, or for extremely small or large particle sizes. The sample was placed in the batch addition port with the ball valve shut. To initiate the transient, the ball valve was opened to let the sample fall into the bed. When small particles were analyzed, the fly ash collection jar was cleaned prior to the transient, and removed ten minutes into the transient. The mass of the jar's contents was measured to estimate mass of elutriated limestone. The test was continued until the transient returned to the background concentration of SO₂. During this time no adjustments were made to fuel, oxygen, or SO₂ flows into the reactor.

5.3 Transient Gas Analysis

Typical CO₂ and SO₂ profiles from limestone tests are shown in Fig. 5.3 and Fig. 5.4. The background concentration was subtracted from the CO₂ profile. These profiles were used to find time constants for calcination and sulfation, and to determine extents of calcination and sulfation.

Figure 5.3 shows the change in the outlet CO₂ concentration during a test of 30 grams of 0.925 mm Gilmore City limestone at a temperature of 1123 K and superficial velocity of 1.1 m/s. The profile shows an initial rise due to the instrument lag time. The CO₂ concentration then decays roughly exponentially back

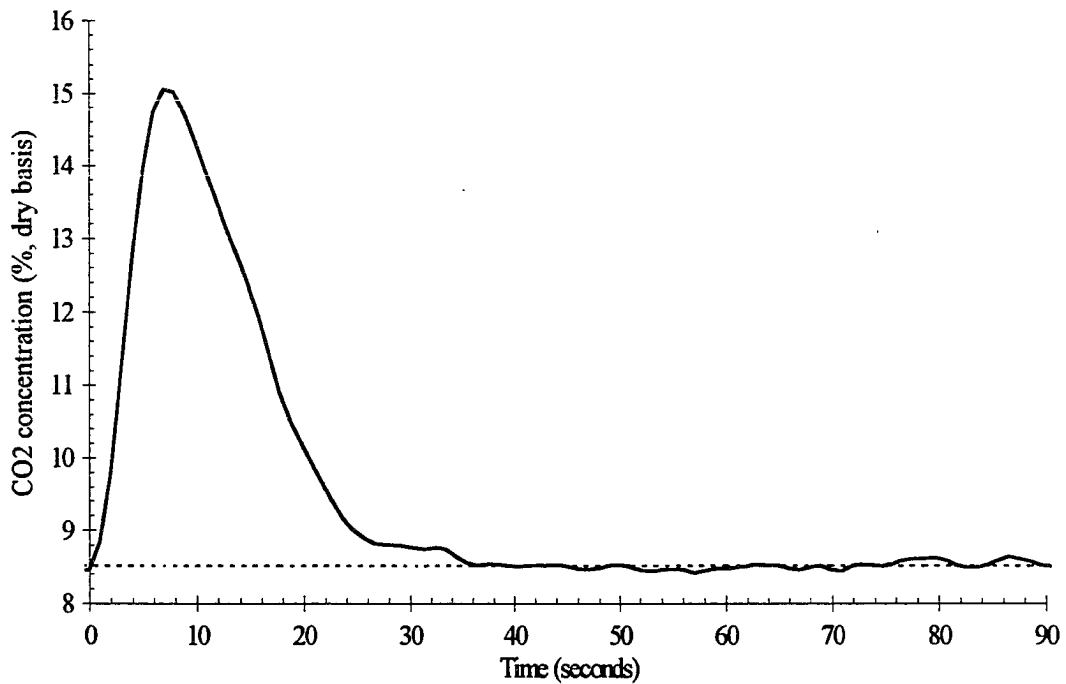


Figure 5.3 CO₂ transient. (T = 1124 K, U_o = 1.12 m/s, m_{LS} = 30 g., d_p = 0.55 mm, O₂ = 5.0%, Gilmore City formation limestone, [SO₂]_i = 1478 ppm)

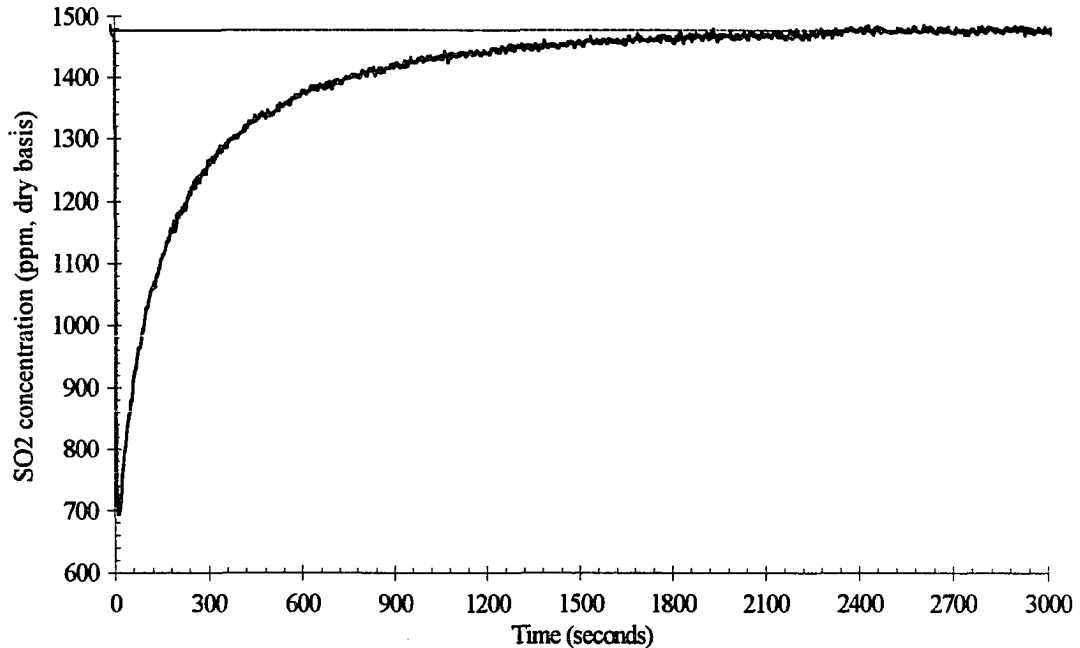


Figure 5.4 SO₂ transient. (T = 1124 K, U_o = 1.12 m/s, m_{LS} = 30 g., d_p = 0.55 mm, O₂ = 5.0%, Gilmore City formation limestone, [CO₂]_i = 8.4%)

to its background value. The initial part of this decrease in concentration is used to determine the calcination time constant. The data is analyzed by one of several equations, depending on the presumed controlling mechanism.

For calcination analysis, only chemical control and diffusion control were considered. The film-mass-transfer control response would be a constant line, which did not correspond to preliminary results. Preliminary analysis showed that the experimental set points for sample mass, air and fuel flow rates, and initial concentrations were such that bulk-mass-transfer would not control the reaction.

To evaluate whether chemical-reaction controlled calcination, the data was transformed into a form of Eqn. (3.18)

$$\frac{\{[CO_2]_E - [CO_2]_O\}\{[CO_2]_R - [CO_2]_I\}}{\{[CO_2]_E - [CO_2]_R\}\{[CO_2]_O - [CO_2]_I\}} = e^{-t / \tau_c} \quad (3.18)$$

In actual computation, the equation was evaluated in the logarithmic form,

$$-\ln \left[\frac{\{[CO_2]_E - [CO_2]_O\} \{[CO_2]_R - [CO_2]_I\}}{\{[CO_2]_E - [CO_2]_R\} \{[CO_2]_O - [CO_2]_I\}} \right] = \frac{1}{\tau_{ck}} t, \quad (5.4)$$

where the inverse of the slope of the line plotted equals τ_{ck} for chemical reaction controlled calcination. The measurement period was taken from t equals 0.1 to 3.0 times τ_{ck} , which corresponds to 90% to 5% of the peak concentration difference, $[CO_2]_O - [CO_2]_I$.

To evaluate whether pore diffusion controlled calcination, the data was put into the form of Eqn. (3.32),

$$\left(\frac{[CO_2]_R - [CO_2]_I}{[CO_2]_E - [CO_2]_R} \right)^{-2} = \frac{1}{\tau_{cd}} t, \quad (3.32)$$

where $[CO_2]_O$ is taken to be a point on the curve shortly after the peak. A plot of this function after this point is expected to give a straight line, the inverse slope of which is the calcination time constant for pore-diffusion control, τ_{cd} .

Figure 5.4 shows the change in SO_2 concentration for the same batch test of limestone shown in Fig. 5.3. The SO_2 concentration drops rapidly after the batch addition of limestone. There is a delay time in the response of both CO_2 and SO_2 , which is the dead-time associated with plug flow through the sampling tube. There is negligible difference in the lag time for the two responses. The initial drop in SO_2 concentration follows a slope which is the same for all of the limestone tests and is the result of the instrument time constant. After reaching a minimum value after about 20 seconds, the SO_2 concentration begins to rise, indicating a decreasing reaction rate for sulfation. The rate at which the

concentration returns to background decreases with time and approaches the background concentration asymptotically.

With a method similar to that used for determining the calcination time constant, the sulfation time constant, τ_s , can be determined for the sulfation transient. For sulfation, analysis was made assuming either chemical reaction control, pore diffusion control, or pore-plugging control. Film diffusion control would result in a constant outlet concentration, which is not seen in the experimental data. Film diffusion needs to be considered as it might effect the sulfation process in combination with the other mechanisms. As for calcination analysis, experimental parameters resulted in a small value of τ_{sb} relative to other time constants, such that bulk mass transfer control is unlikely.

Assuming chemical reaction control, sulfation is expected to follow:

$$\frac{\frac{[SO_2]_I - 1}{[SO_2]_R} - 1}{\frac{[SO_2]_I - 1}{[SO_2]_O} - 1} = e^{-t / \tau_{sk}}, \quad (3.64)$$

A plot of the data based on this equation on semi-log coordinates is expected to give a straight line for early times. The slope of this line is used to determine τ_{sk} . The values of τ_{sk} used to determine particle size and temperature dependence in this investigation is found using Eqn. (3.64), although these time constants only have meaning if chemistry is the controlling mechanism. If another mechanism is determined to control sulfation, the time constant developed for that mechanism should be used in analyzing particle size and temperature dependence. Examination of the data for pore-plugging control was also done by plotting the data according to Eqn. (3.83):

$$-\ln\left\{\left(\frac{[SO_2]_I}{[SO_2]_R} - 1\right)\sqrt{t}\right\} = \frac{1}{\tau_p}t - \ln\left\{\frac{c_2}{L}\sqrt{\frac{D_{es}}{2c_{1S}}}\right\}. \quad (3.83)$$

Estimates of the extents of calcination and sulfation were done by numerically integrating the CO₂ profile and the difference between the SO₂ profile and the background SO₂ concentration. These integrals were multiplied by the volumetric flow rate through the combustor and divided by the theoretical mass of CO₂ and SO₂ released to give the extents of reaction. The resulting expressions for the extent of calcination is

$$\text{Extent of calcination} = X_c = \frac{Q \int_0^{\infty} \{[CO_2]_R - [CO_2]_i\} dt}{\frac{f_{CaCO_3} m_{LS}}{M_{CaCO_3}}}, \quad (5.5)$$

where [CO₂]_R and [CO₂]_i have dimensions of mol/m³, rather than mole fraction as is measured.

At lower temperatures, the larger particles give CO₂ profiles that do not rise substantially above background and return to background very slowly. Changes in the background concentration affect the results from these transients significantly. Additionally, it is difficult to determine the time at which the CO₂ concentration returns to background.

Table 5.2 shows the results for a series of five tests using the same operating conditions and limestone size and mass. These tests were used to determine 95% confidence intervals for the extent of calcination when various time intervals were used for analysis. In these five tests the CO₂ concentration returned to background in around 50 seconds. When the extent of calcination was measured after 50 seconds the extent of calcination was accurate to within of $\pm 1.69\%$ of its value as determined by a 95% confidence interval calculation. The accuracy for the extent of calcination from analysis

Table 5.2 Extent of calcination measured for different lengths of time for five runs at the same conditions. ($T_{bed} = 1123$, $d_p = 1.09$ mm, $U_o = 1.0$ m/s, $m_{LS} = 20$ g., Gilmore City formation limestone, $[SO_2]_i = 1510$ ppm)

Time of measurement of CO ₂ transient (s)	Mean extent of calcination (%)	Lower 95% confidence limit (%)	Upper 95% confidence limit (%)
50	79.91	78.22	81.60
300	79.18	76.81	81.55
600	75.63	65.01	86.26
1200	71.07	35.18	106.96

done at the 5 minute point was $\pm 2.37\%$, which is not substantially worse. If a time period of 600 or 1200 seconds is used for the integration to find the extent of calcination, the accuracy decreases dramatically. This is because the background level changes slowly over these long time periods. For the larger particles the CO₂ transient is close to the background for the entire transient and calcination may take more than five minutes to complete. Because of this, a five minute interval was selected as a compromise. The extent of calcination may be somewhat underpredicted for larger particles after five minutes, but if a longer time is analyzed the accuracy of the extent of calcination is poor.

The expression for extent of sulfation, which is also referred to as calcium utilization, is

$$\text{Extent of sulfation} = X_s = \frac{Q \int_0^{\infty} \{[SO_2]_i - [SO_2]_R\} dt}{\frac{f_{CaCO_3} m_{LS}}{M_{CaCO_3}}}, \quad (5.6)$$

where $[SO_2]_i$ and $[SO_2]_R$ have dimensions of mol/volume, rather than the measured quantity of parts per million (ppm).

The change in volume between product and reactant gases is considered when computing the volumetric flow rate. For conversion results, compensation for the water vapor removed in the perma-pure dryer is considered when determining the concentration values. It is assumed that 100% of the water vapor resulting from complete combustion is removed. Complete combustion stoichiometry is determined from the baseline CO_2 concentration prior to the transient. Results in the figures in this report show the CO_2 and SO_2 concentrations as measured by the instruments, without compensation for water vapor removal.

In the laboratory, several series of experiments were conducted to determine time constants and extents of calcination and sulfation under a variety of conditions. This data was analyzed using the full and the simplified models. An initial series of tests was accomplished at 1123 K for seventeen particle sizes to examine the effect of particle size on the extent of sulfation, and to validate the full sulfation model. A series of tests was conducted to investigate temperature and particle size effects on both calcination and sulfation. This series consisted of testing four sizes of limestone and one size of pre-calcined limestone at seven temperatures. The effect of temperature on calcination was evaluated through a series of eleven tests at a variety of temperatures without SO_2 in the bed.

Other possible causes of variation were also examined. One series of tests, which consisted of five batch tests with no SO_2 background, examined the effects of superficial bed velocity on calcination. In another series, additional CO_2 was added to the bed to analyze the effect of CO_2 concentration on the calcination reaction. A series of four tests with a varied background oxygen level was run to test the effects of the O_2 baseline on sulfation. Two different types of limestone were examined using different particle sizes. Gilmore City formation limestone was further analyzed by separating large particles out by color to examine the variation within a limestone type.

5.4 Full Scale Boiler Testing

Testing on full scale boiler involved several steps. Liquid nitrogen needed to be supplied to the Nicolet FTIR bench unit. The sample system was connected to the sample port on the cyclone. Particulate filters were checked for fly ash build up. The cooling system air filter was changed and the vacuum pump was lined up. The boiler control personnel placed the boiler in manual control. This allowed for a constant feed rate of coal and limestone. Additionally the O₂ control was placed in manual.

A background run was made on the FTIR to ensure accurate readings. This background spectra eliminated signals due to the spectrometer and its environment from the sample. The background spectrum was the result of the output of the source; the response of the beamsplitter, optics, and detector; and any atmospheric gases inside the FTIR bench. Instrument settings were adjusted to determine the run time of the test, the background file to which the signal was compared, and the time interval between data points. After setting the vacuum level by throttling the suction to the vacuum pump, the run was started on the computer. A sufficient background of at least 20 minutes of data was taken before the batch addition. The limestone was then dumped into the boiler by opening a knife valve.

After the run time had expired, the data was prepared for analysis. As the reaction progressed, a chart called a Graham-Schmidt chart, which described changes in chemical concentrations generally, was available to the operator. Chemigrams, which describe the changes in specific chemicals, were then produced. After the chemigrams were completed the data was quantified. The quantification routine compared the chemigram data to sets of calibration data that had been put in a matrix form.

5.5 Particle Analysis

Samples of bed material were also withdrawn from the combustor for particle analysis. A sample extractor was made to extract samples of hot bed material through the

valve used to batch samples into the combustor. The purpose of extracting samples was to compare transient gas analysis results to measurements made on the particles and to develop additional insight into the reaction processes. Extracted samples were bathed in nitrogen to ensure no interaction with water vapor before testing. The samples were sealed in epoxy rings and then polished to provide a cross-sectional view. Samples extracted from bottom ash from the ISU power plant were also prepared for analysis.

Particles were viewed by reflected light microscopy to gather visual trends and to prepare for analysis using the SEM. Microprobe linescanning was done to measure sulfation rim thicknesses and relative local conversions through the rims. Some of the samples were sent to Spectrum Petrographics, Inc. to be made into thin sections. These were then examined under a polarized reflected light microscope.

Gilmore City formation limestone that had been calcined in the laboratory combustor at temperatures of 1123 K and 1200 K were prepared for surface area analysis. These samples were analyzed for pore volume distribution and surface area by Micromeritics, Inc. using single point and multi-point nitrogen adsorption methods.

6. RESULTS AND DISCUSSION

6.1 Transient Gas Analysis of Calcination

In this study, experiments were done to examine the change in calcination time constants and in the extent of calcination under various conditions. The effects of particle size, CO₂ concentration, temperature and flow velocity were all examined. Additionally, testing was conducted in the lab using two additional types of limestone provided by Ahlstrom Pyropower. Analysis was made by comparing simplified results for controlling mechanisms as discussed in section 3.2.

6.1.1 Comparison of transients to the calcination model

The full model developed to describe calcination is a shrinking particle core model, as described by Eqns. (3.4) through (3.7). These four differential equations were solved numerically using the program code listed in the appendix. This calcination model was also simplified into Eqns. (3.9) and (3.10):

$$-\frac{dr_{cc}}{dt} = \frac{\{[CO_2]_E - [CO_2]_I\} \frac{M_{LS}}{f_{CaCO_3} \rho_{LS}}}{\frac{3m_{LS}}{Q\rho_{LS}r_p} \frac{r_{cc}^2}{r_p^2} + \frac{1}{h_c} \frac{r_{cc}^2}{r_p^2} + \frac{(r_p - r_{cc})r_{cc}}{D_{ec}r_p} + \frac{1}{k_c}} \quad (3.9)$$

$$\frac{[CO_2]_E - [CO_2]_R}{[CO_2]_E - [CO_2]_I} = \frac{1}{1 + \frac{3m_{LS}}{Q\rho_{LS}r_p} \left(\frac{1}{\frac{1}{h_c} + \frac{(r_p - r_{cc})r_p}{D_{ec}r_{cc}} + \frac{1}{k_c} \frac{r_p^2}{r_{cc}^2}} \right)}. \quad (3.10)$$

Figure 6.1 shows how the full model was fit to the transient data for two different particle sizes. Curve fitting was not successful using a single value for k_c and D_{ec} for a range of particle sizes. The curve fits shown in Fig. 6.1 were made by varying D_{ec} between the particle sizes. This result either indicates that the model predictions do not satisfactorily describe calcination, or that the effective diffusivity varies between particle sizes. Particle analysis suggests that sintering early in the reaction may actually cause this decrease in diffusivity for the larger particle sizes. As the particle radius increases, the time to complete calcination increases. This allows more time for sintering to occur. Examination of four particle sizes using the model requires D_{ec} to be increasingly smaller as the particle size increases.

The values obtained by curve fitting do not correspond well to those found in the

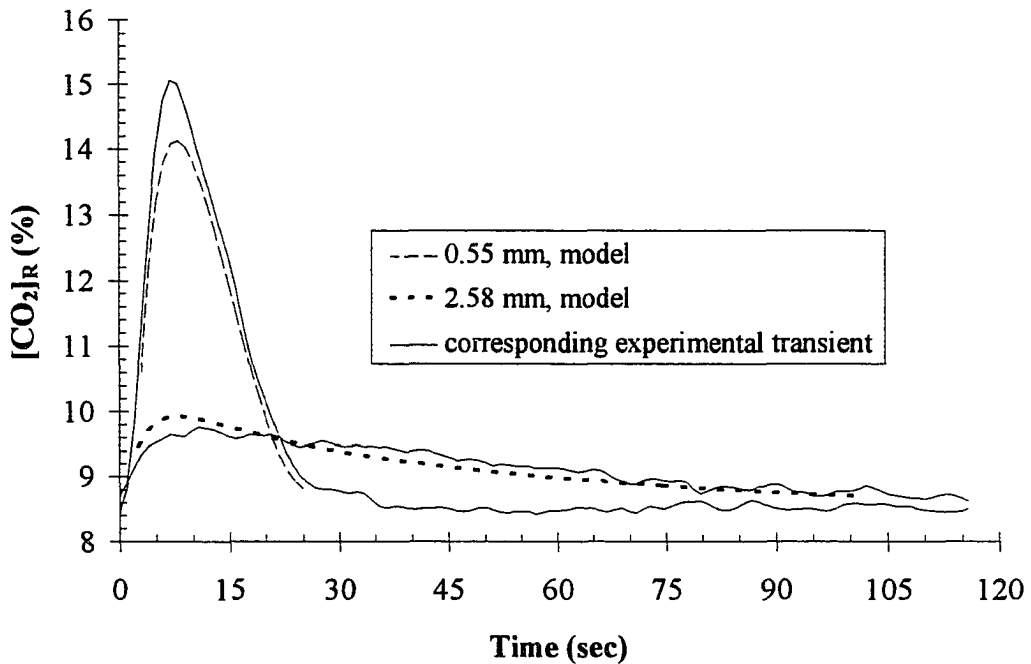


Figure 6.1 Comparison of calcination model to transients. ($T_{bed} = 1123$ K, $m_{LS} = 30$ grams, $U_o = 1.1$ m/s. Fit parameters are: $k_c = 0.1$ m/s (both cases), and $D_{ec} = 1.67 \times 10^{-4}$ m²/s (0.55 mm test) and 3×10^{-5} m²/s (2.58 mm test)).

literature. Borgwardt [48] and Dennis and Hayhurst [12] found values of k_s around 0.01 m/s. Milne *et al.* [12] found that the shrinking core mechanism did not accurately describe calcination. Values for D_{ec} were high when compared to theoretical calculated values. The value of D_{ec} equal to $1.67 \times 10^{-4} \text{ m}^2/\text{s}$ as shown in Fig. 6.1 for the 0.55 mm particle size is the value found for bulk diffusivity of CO_2 in nitrogen. This is much higher than expected. It must be presumed that diffusivity in the freshly calcined layer is not controlled by Knudsen diffusivity, which would result in a much lower value of D_{ec} .

The numerical solution allows for the evaluation of the controlling resistances during the transient. Figure 6.2 shows the solution for the batch addition of 0.55 mm limestone shown in Fig. 6.1. The chemistry resistance is much higher than any of the other

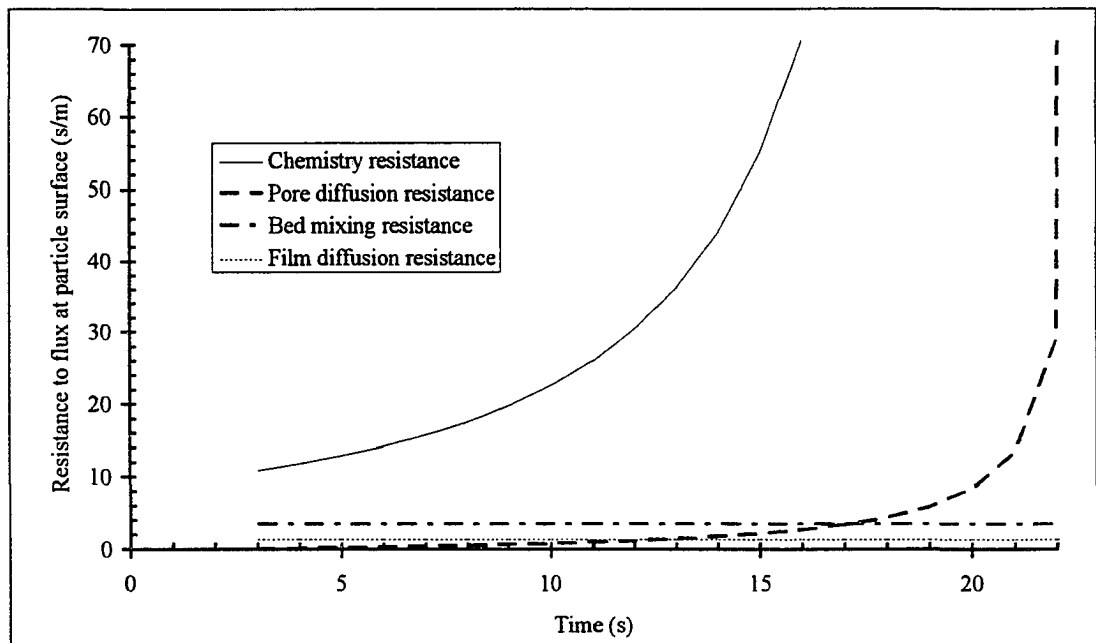


Figure 6.2 Resistances to reaction for 0.55 mm diameter particle. ($T_{bed} = 1123 \text{ K}$, $m_{LS} = 30 \text{ grams}$, $U_o = 1.1 \text{ m/s}$. Fit parameters are: $k_c = 0.1 \text{ m/s}$ (both cases), and $D_{ec} = 1.67 \times 10^{-4} \text{ m}^2/\text{s}$).

resistances. At a temperature of 1123 K this particle size is controlled by the chemical reaction rate. There is some bed mixing resistance early in the reaction, but it is not significant. In contrast to this, Fig. 6.3 shows the resistance plot for the 2.58 model run shown in Fig. 6.1. Since diffusivity is much lower, the pore diffusion resistance is equal in significance in the latter part of the transient. Thus, for larger particles, the lower predicted diffusivity leads to a situation where both chemical reaction and diffusion are involved in limiting the reaction rate.

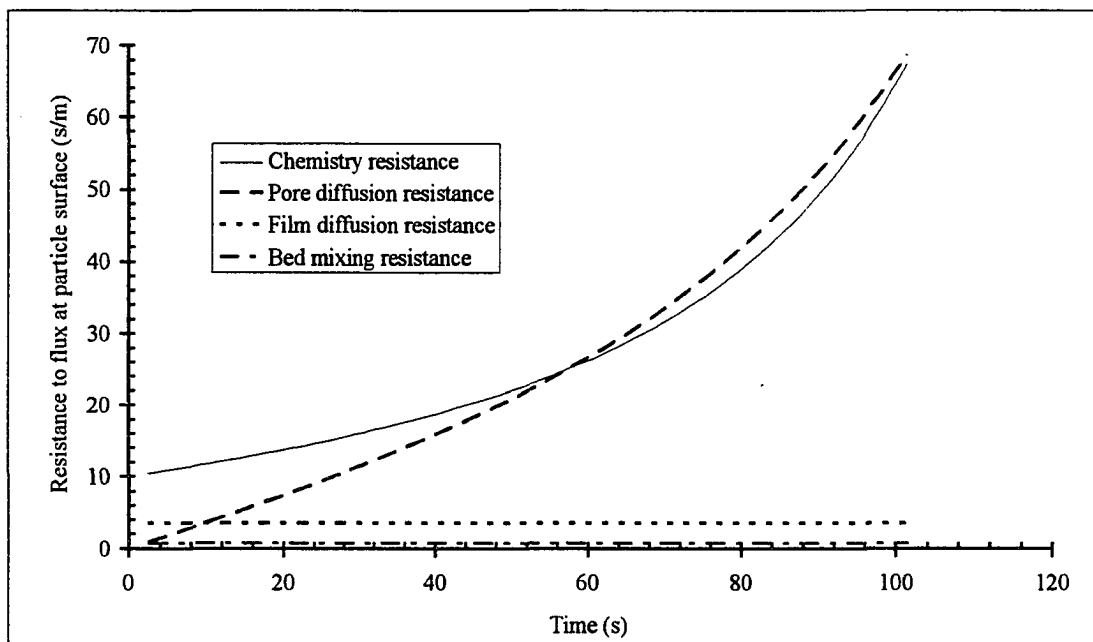


Figure 6.3 Resistances to reaction for 2.58 mm diameter particle. ($T_{bed} = 1123$ K, $m_{LS} = 30$ grams, $U_o = 1.1$ m/s. Fit parameters are: $k_c = 0.1$ m/s, and $D_{ec} = 3 \times 10^{-5}$ m²/s).

6.1.2 Effect of particle size

The effect of particle size on the calcination time constants and the extent of calcination was investigated. In chapter three, the full calcination model was reduced to

simplified expressions for the calcination time constant. These expressions help to indicate the controlling mechanism for calcination. In this investigation, chemical-reaction and pore-diffusion control were considered directly using equations from section 3.2.

Data from tests with four particle sizes at seven temperatures were changed into the form of Equation (3.18) for analysis of τ_c :

$$\frac{\{[CO_2]_E - [CO_2]_O\}\{[CO_2]_R - [CO_2]_I\}}{\{[CO_2]_E - [CO_2]_R\}\{[CO_2]_O - [CO_2]_I\}} = e^{-t/\tau_c}. \quad (3.18)$$

Results from four of these tests are shown in Fig. 6.4. In this figure τ_c can be determined from the reciprocal of the slope. The data should plot as a straight line for early times if calcination is chemistry-controlled. The lines for the data in Fig. 6.4 are fairly straight

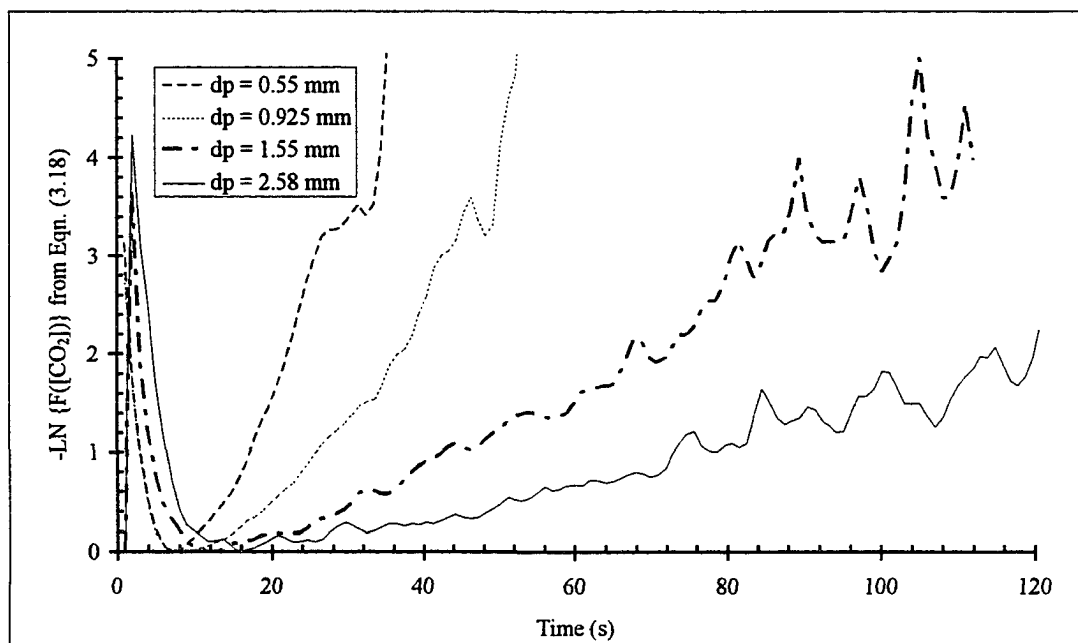


Figure 6.4 Transient data changed into the form of Eqn. (3.18) for evaluation of τ_c . ($T_{bed} = 1123$ K, $m_{LS} = 30$ grams, $U_o = 1.1$ m/s).

over the length of the data. A slight upward curvature is apparent in these data and in most of the results. Least squares lines were calculated for the region where the log function equaled 0.1 to 3.0. This analysis should have been done for shorter times. The region from 0.1 to 1.0 for the log function would have been a better region to take data. Nevertheless, the curves do form fairly straight line throughout.

If chemical reaction controls calcination, τ_c should vary directly with particle diameter. Results for tests conducted with 30 gram batches of four particle sizes are shown in Fig. 6.5. These tests were conducted at seven different temperatures. In these tests the value of τ_c was determined using Eqn. (3.18) for chemical reaction controlled calcination. Figure 6.5 shows that τ_c is proportional to particle size at lower temperatures,

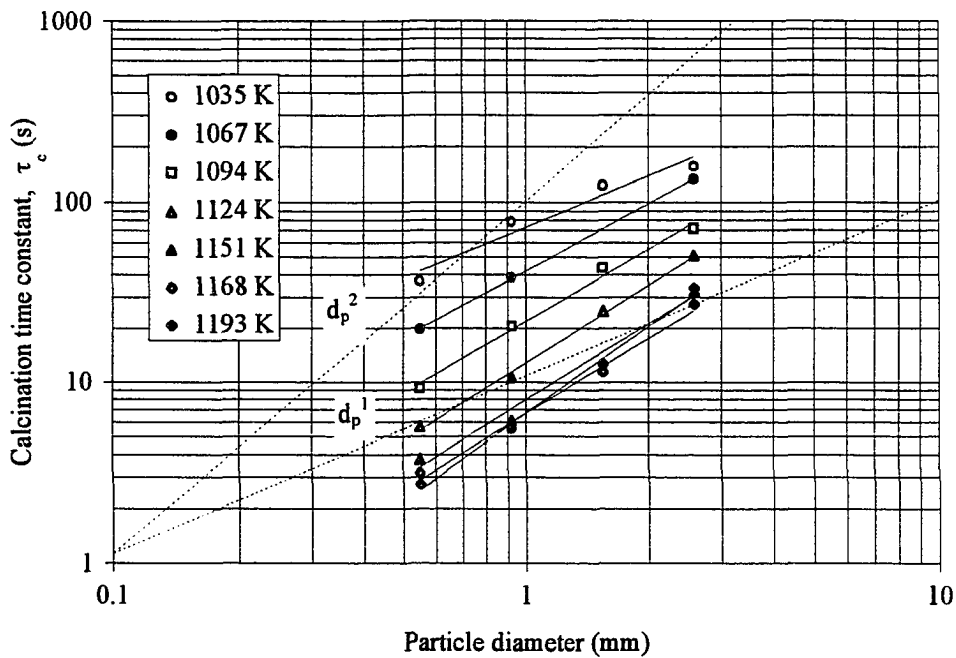


Figure 6.5 Log plot of calcination time constant vs. particle diameter ($U_o = 1.12$ m/s, $[CO_2]_i$ varies with temperature $[SO_2]_i = 1500$ ppm.. Tests run at $T = 1123$ K used 20 g batches and had no SO_2 injection. Lines shown are regression lines.)

but has an increasing power law dependence as temperature is increased. The regressions shown in Fig. 6.5 show a particle size dependence of from $d_p^{.91}$ to $d_p^{1.62}$, with the particle size dependence increasing with temperature. The values of the particle size dependence for each temperature are shown in Table 6.1.

Table 6.1 Particle size dependence of τ_c at various temperatures. ($U_o = 1.12$ m/s, $[\text{CO}_2]_i$ varies with temperature, $m_{LS} = 30$ g. Tests at 1123 K were conducted with $m_{LS} = 20$ g and in the absence of SO_2 injection.)

Bed temperature, K	Particle size dependence, r^n
1035	0.91
1067	1.20
1094	1.31
1123	1.04
1124	1.44
1151	1.42
1168	1.40
1193	1.62

The deviation from d_p^1 dependence in the tests could be caused by one of two factors. Both film diffusion and pore diffusion could possibly result in higher particle diameter power laws. Analysis for the time constant associated with the rate of change of the dimensionless core radius for film diffusion control, as developed in Eqn. (3.22), is $\tau_{sh} = d_p / c_{1c} h_c$. However, h_c also has a particle size dependence between $1/d_p^{1/2}$ to $1/d_p$. This is evident by analysis of the two correlations used in the model. The first was a correlation for the Sherwood number, Sh , developed by Froessling for isolated spheres [49]:

$$Sh = \frac{h_s d_p}{D_{es}} = 2 + 0.6 \text{Re}^{\frac{1}{2}} \text{Sc}^{\frac{1}{3}}, \quad (6.1)$$

where Re is the Reynolds number, ud_p/v , and Sc is the Schmidt number, D_{AB}/v . The other correlation used was developed by La Nauze for char combustion in fluidized beds [50]:

$$Sh = \frac{h_s d_p}{D_{es}} = 2\varepsilon_b + 0.69 Re^{\frac{1}{2}} Sc^{\frac{1}{3}}, \quad (6.2)$$

where ε_b is the bubble voidage in the bed. This makes the overall size dependence of the film diffusion time constant $d_p^{1.5}$ to d_p^2 . Since film diffusion cannot be the controlling mechanism based on a non-constant transient, the overall time constant would have a smaller dependence. Additionally, the effect of film mass transfer would diminish over time, since the other resistances are increasing while film diffusion resistance is decreasing in Eqn. (3.11) and constant in Eqn. (3.12). The effect of superficial velocity on the reaction was conducted and will be discussed in section 6.1.5.

Pore diffusion could also play a role in the result of time constants which are greater than one. An exact particle size dependence cannot be extracted for the value of τ_c since it is based on chemistry-controlled calcination from Eqn (3.18). It is believed that a particle size dependence greater than one could indicate pore diffusion control because the time for complete conversion for this case equals two. This is shown in Levenspiel [29], and corresponds to a chemistry-controlled time for complete conversion size dependence of one. Use of Eqns. (3.31) and (3.32) which describe pore-diffusion controlled calcination for flat plates was analyzed, but the data in these forms did not form a straight line which could be systematically measured. Numerical solution of the full model indicates that pore diffusion may give a significant resistance to reaction.

Deviation from a d_p^1 relationship for τ_c becomes more apparent at higher temperatures. At these temperatures, chemistry is no longer rate limiting, and transition to the "d-squared" dependence of diffusion becomes apparent. This might indicate that

diffusion resistance may become significant at the higher chemical reaction rates associated with these temperatures. It is also interesting to note how the curves for the three highest temperatures begin to coincide. The chemical reaction rate temperature dependence is governed by an Arrhenius relationship, i.e. k is proportional to $e^{-E/RT}$. This temperature dependence is greater than that for diffusion control, e.g. bulk diffusivity is proportional to $T^{3/2}$. An observed activation energy determined for a $T^{3/2}$ dependence would be the value for species transport, approximately given by $E_a = 3RT/2$, which is around 3 kcal/mol for these temperatures. The fact that the τ_c vs. particle diameter curves of Fig. 6.1 begin to coincide at higher temperatures may be explained by the lower temperature dependence for diffusion. This strengthens the argument for diffusion control at higher temperatures which is evidenced by a higher particle size dependence.

6.1.3 Effect of temperature

The same data which were considered for particle size effects are plotted in Fig. 6.6 as $1/\tau_c$ vs. $1/T$. Fitting straight lines through this data on a log-linear scale gives activation energies for calcination ranging from 29.5 to 45.5 kcal/mol. The fit is relatively good considering the small number of data points for these regressions, which consist of five to seven points per particle size. Table 6.2 shows the activation energies and the 90% confidence interval associated with the data. Activation energies range 29.5 to 45.4 kcal/mol. The activation energy decreases as the particle size increases. Within the uncertainty supported by 90% confidence intervals, the difference in activation energies between adjacent particle sizes is not significant. However, when the largest particle size (2.58 mm) is compared to the two smallest sizes, there does appear to be a significant difference in activation energies.

This conclusion is confirmed by performing a t-test on the slopes of these activation energy curves. The null hypothesis in this case was: "There is no significant

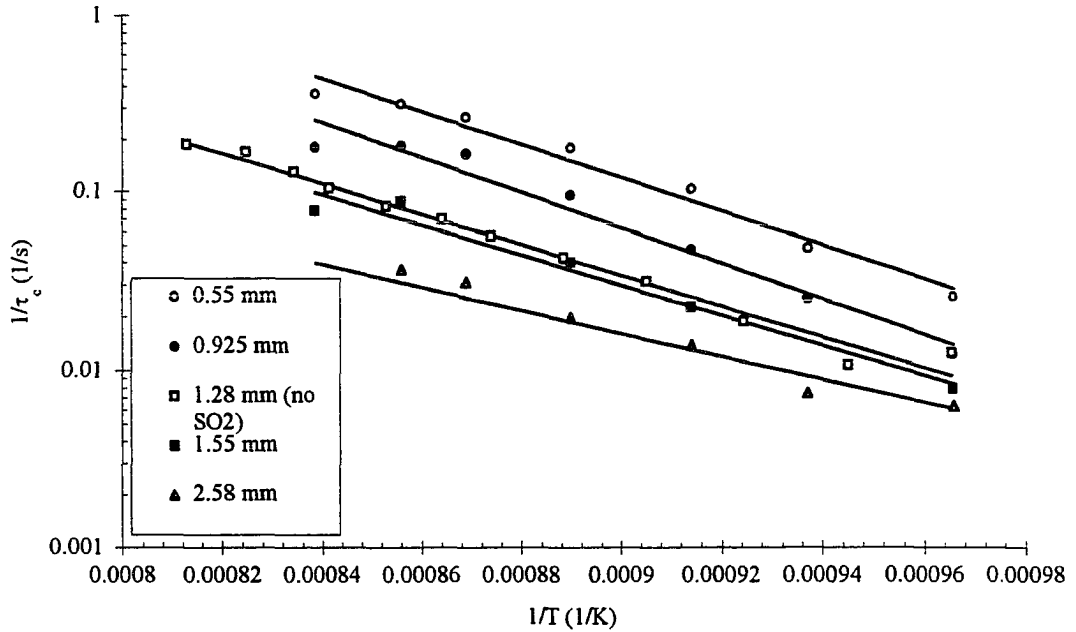


Figure 6.6 Activation energy plot for calcination. (30 grams of Gilmore City formation limestone, $U_o = 1.12$ m/s, $[SO_2] = 1500$ ppm except as noted)

Table 6.2 Calcination activation energies for various particle sizes. ($U_o = 1.12$ m/s, $[CO_2]_i$ varies with temperature, $m_{LS} = 30$ g. Tests done with $d_p = 1.28$ mm were conducted in the absence of SO_2 injection.)

Particle diameter, mm	Activation energy, kcal/mol	90% confidence limits for activation energy, kcal/mol
0.550	43.4	± 6.09
0.925	45.5	± 7.94
1.28	39.4	± 3.05
1.55	38.6	± 9.11
2.58	29.5	± 7.45

difference between the slopes (activation energies) for different particle sizes.” The alternate hypothesis is: “The slope (activation energy) for the larger particle size is less than that for the larger particle size.” The statistical analysis for this t-test is corresponds to the t-test for two means given in Kennedy and Neville [51], and the t-test to find the significance of the slope found in the same reference. It involves finding the variance of the residuals for each line, which is determined by:

$$s_{y|x}^2 = \left(\frac{\sum \varepsilon_i^2}{n-2} \right), \quad (6.3)$$

where ε_i^2 represents the square of the residuals. The combined variance of the two slopes being compared, $s_{y|xc}$, is computed from:

$$s_{y|xc}^2 = \frac{s_{y|x1}^2(n_1 - 2) + s_{y|x2}^2(n_2 - 2)}{(n_1 - 2) + (n_2 - 2)}. \quad (6.4)$$

The standard deviation for the difference of the slopes is then determined by:

$$s_{bd} = s_{y|xc} \sqrt{\frac{1}{s_{x1}^2(n_1 - 1)} + \frac{1}{s_{x2}^2(n_2 - 1)}} \quad (6.5)$$

The t-statistic is then found from:

$$t = \frac{|b_1 - b_2|}{s_{bd}} \quad (6.6)$$

This t-statistic is compared to the one tailed t-distribution value for (n_1-2+n_2-2) degrees of

freedom to determine the validity of the null hypothesis.

In these t-tests the slope (activation energy) of the 0.55 mm particles was higher than the 1.55 mm particle activation energy at a 6% level of significance. The 0.55 mm slope was higher than the 2.58 mm slope with 1% level of significance. Statistically, the activation energy is decreasing as particle size increases.

This trend of decreasing activation energy with increasing size is not unexpected. Observed activation energies may differ from the true chemical rate activation energy due to diffusion processes. Pore diffusion in catalyst particles gives observed activation energies which are 1/2 of the true value for uni-modal pore distributions and 1/4 of the true value of bimodal distributions. Film diffusion processes will give low activation energies (1-3 kcal/mol) due to temperature effects on bulk or Knudsen diffusivities [52].

Analysis of the effect of temperature for gas-solid reactions as considered by the shrinking core model is significantly different than the results for catalyst pellets. In the shrinking core model the reaction does not occur in the volume of a pellet, but at a receding interface. Thus, the activation energy varies between the chemical activation energy and the low activation energy associated with film diffusion.

The activation energies for the smaller particles approach results in the literature for chemically controlled calcination. Borgwardt [5] estimated activation energies for small particles (1-10 μ m) of 48-49 kcal/mol. Powell and Searcy [53] also estimated activation energies for calcination of 49 ± 3 kcal/mol.

Khraisha and Dugwell [10,54] determined activation energies in a thermogravimetric analyzer (TGA) and in a suspension reactor for 40-90 μ m Cauldron limestone particles. In the TGA they obtained activation energies between 98 and 350 kcal/mol depending upon sample mass and heating rate in a simulated combustion atmosphere. When using a suspension reactor they obtained 47 kcal/mol. The conclusion they draw is that TGA analysis may give misleading values for activation energy due to

they draw is that TGA analysis may give misleading values for activation energy due to slow mass transfer.

All of the aforementioned investigators, who used smaller particle sizes than were used in the present study, concluded that calcination rates were chemically controlled. In the laboratory FBC experiments, the smaller particles exhibited chemically-controlled calcination; however, the larger particles had reduced activation energies, and may be controlled by processes other than chemical reaction.

Both particle size and temperature appear to have relatively little impact on the extent of calcination. The extent of calcination is determined from Eqn. (5.7)

$$\text{Extent of calcination} = X_c = \frac{Q \int_0^{\infty} \{[CO_2]_R - [CO_2]_i\} dt}{\frac{f_{CaCO_3} m_{LS}}{M_{CaCO_3}}} \quad (5.5)$$

Figure. 6.7 shows the extent of calcination five minutes into the transient for the data which was discussed for particle size dependence and activation energy calculation. The extent of calcination shown is around 80% for a large portion of the data. In Fig. 6.7, calcination reaches its greatest extent at around 1123 K, which is often cited as the optimum temperature for sulfur sorption. A carbonation reaction, the reverse of Eqn. (2.1), is the most conceivable mechanism to limit the extent of calcination to less than 100%, since pore plugging due to sulfation does not occur until later times in the reaction.

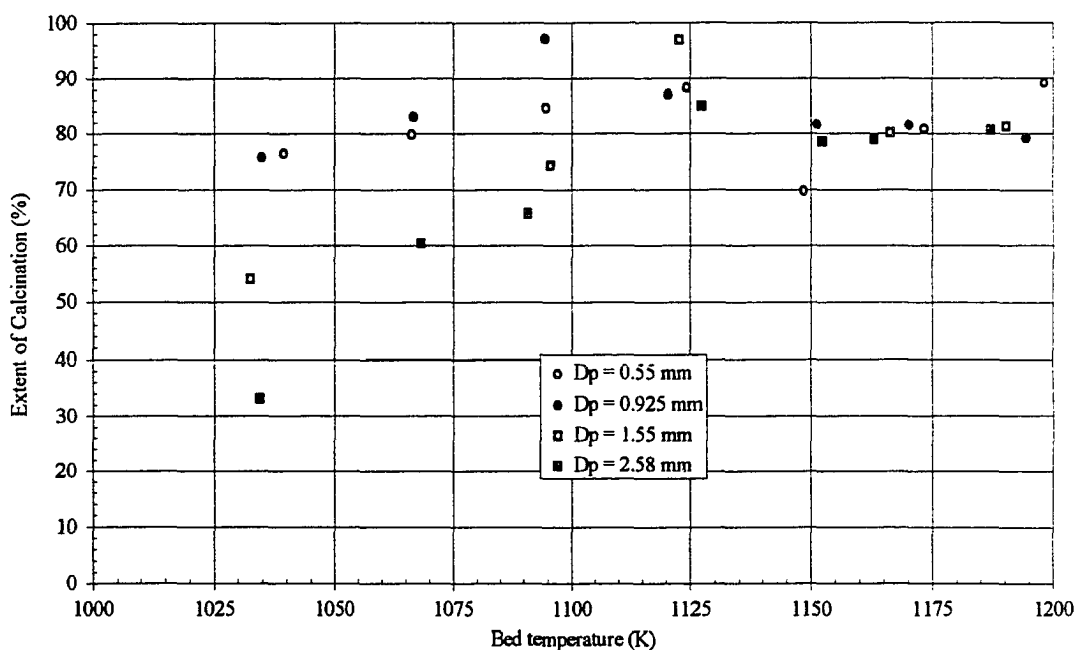


Figure 6.7 Extent of calcination at various temperatures for four particle sizes ($U_o = 1.12$ m/s, $m_{LS} = 30$ g of Gilmore City formation limestone, $[SO_2]_i = 1480$ ppm.)

6.1.4 Effect of CO₂ concentration

Five experiments were run to determine the effect of background CO₂ concentration, $[CO_2]_i$, on the reaction rate. In Table 6.3, the calcination time constant, τ_c , as reported for five different values of $[CO_2]_i$. These tests were conducted by flowing CO₂ from a cylinder and reducing air flow to maintain a temperature of 1123 K and a superficial velocity of 1.5 m/s. SO₂ was not added in these experiments. The calcination time constant increases slightly with increasing background CO₂ concentration, a result consistent with the work of other researchers [10,12,15]. This result is also consistent with the analysis for τ_c found for chemistry-controlled calcination. In Eqn. (3.18) it was determined that τ_c should be inversely proportional to $\{[CO_2]_E - [CO_2]_i\}$, which it is.

Table 6.3 Calcination time constant for various background CO₂ concentrations. (m_{LS} = 25 g. of Gilmore City formation limestone, d_p = 1.29 mm, U_o = 1.5 m/s, T_{bed} = 1123 K)

[CO ₂] _i (%)	[CO ₂] _E -[CO ₂] _i (mol/m ³)	τ _c (s)
7.78	4.36	28.2
10.23	4.10	30.3
12.16	3.89	36.5
15.10	3.57	34.1
17.48	3.31	38.7

6.1.5 Effect of superficial velocity

A series of experiments were done to examine whether superficial velocity in the bed affected τ_c. Table 6.4 shows the results of five experimental runs which were

Table 6.4 Effect of superficial velocity on calcination time constant and extent of calcination. (Gilmore City limestone, d_p = 1.55 mm, m_{LS} = 30 g., T_{bed} = 1123 K)

Superficial velocity (m/s)	[CO ₂] background (%)	τ _c (seconds)
0.95	7.95	32.9
1.19	6.96	32.9
1.43	6.48	30.7
1.66	6.12	42.1
1.92	5.92	31.3

conducted at different flow velocities. In this experiment τ_c was around 32 seconds for most of the runs. The calcination time constant of 42.1 seconds for the run at 1.66 m/s appears to be an outlier. Neglecting this point, a 95% confidence interval on the mean of the remaining four points gives a value for τ_c of 32.0 ± 1.1 seconds. More runs would be required to validate this value. If film diffusion had an important role in calcination, an

increase in superficial velocity would cause τ_c to decrease. Thus, it is unlikely that film diffusion resistance is significant in the calcination process within a fluidized bed. The effect of u_o on the mass transfer coefficient is small at the low values of Re_d used (approximately 6 to 9). In these correlations, that is Eqns. (6.1) and (6.2), velocity is raised to the 1/2 power in the Reynolds number term.

6.1.6 Results for different limestone types

Transient analysis experiments were also conducted on two other types of limestone beside the Gilmore City Formation limestone from the I.S.U. power plant. Figure 6.8 plots the CO_2 concentration above background vs. time for the Nova Scotia and Cedar Bay #1 limestones. The transients shown are typical of results for other particle sizes in that the Nova Scotia limestone has a lower peak CO_2 concentration, and returns more slowly to background than the other limestones. Table 6.5 shows calcination and

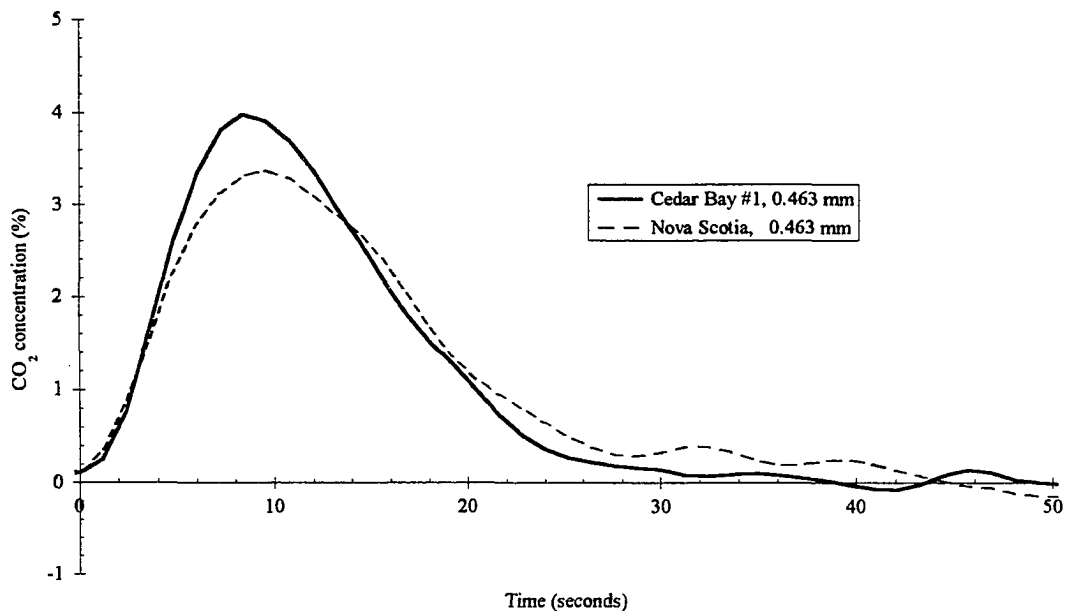


Figure 6.8 Calcination transients for two other limestones. ($T_{bed} = 1123$ K, $U_o = 1.1$ m/s, $m_{LS} = 20$ grams, $[SO_2]_f = 1480$ ppm.)

Table 6.5 Time constants and reaction extents for two limestone types with various particle sizes. ($T_{bed} = 1123$ K, $U_o = 1.1$ m/s, $m_{LS} = 20$ g.)

	Mean particle diameter (mm)	τ_c (s)	Extent of Calcination (%)
Cedar Bay #1	0.231	4.59	92.8
	0.328	4.95	75.8
	0.463	5.02	77.8
	0.655	8.73	80.3
	0.925	12.3	85.3
Nova Scotia	0.328	4.17	75.4
	0.463	9.83	84.4
	0.655	11.0	88.7

sulfation results for 25 tests done with varied particle sizes at $T_{bed} = 1123$ K, $U_o = 1.06$ m/s, and a batch size of 20 grams of limestone. The Nova Scotia limestone generally has a higher extent of calcination and a higher calcination time constant than the Cedar Bay #1 limestone. The reason for this is not clear. It may involve the magnesium content of the stone, and its effect on diffusion characteristics and particle sintering. Calcination data for the Gilmore City formation limestone was invalidated by excessive drift in the CO_2 meter for the 20 gram batch mass used in this comparison.

6.2 Particle Analysis of Calcined Particles

6.2.1 Scanning Electron Microscope (SEM) analysis

Another phase of this study involved analysis of particles which were extracted in the middle of the calcination process. Reflected and transmitted light microscopy and SEM analysis of particle cross sections reveal an inner core for particles removed during the calcination transient. Some particles also reveal two zones within the outer calcined

ring. The calcination process can be illustrated fairly thoroughly by examination of SEM photographs for a single particle extracted in the middle of the reaction.

To fully appreciate the structural changes that take place during calcination, it is important to see the physical nature of the limestone being calcined. Figure 6.9 is an SEM photograph of a thin section of Gilmore City formation limestone. The SEM photograph does not show the oolitic formation in the same detail as is seen using the transmitted light microscope. Nevertheless, with a close examination circular structure of the oolites can be observed. The limestone is seen to have a featureless compact structure. There appears to be little porosity in the limestone prior to reaction.

Figure 6.10 is an SEM photograph of a particle extracted two minutes after addition of 150 grams of 2.58 mm limestone. The appearance is very different from that of the unreacted limestone. The center region, which has a light color, contains CaCO_3 which is in the process of calcining. The compact structure of the limestone is giving way to a coarse, broken structure. The darker intermediate region and the outer bright region have undergone calcination. The darker region has been calcined more recently and the outer region has undergone some further structural changes.

Further detail of this particle is shown in Figs. 6.11 - 6.14. Within the calcination core there is a region that has retained a compact structure. The section identified as Region A in Fig. 6.10 is shown in greater detail in Fig. 6.11. An interesting feature of this region are the holes that are present in the center of the picture. This appears to be outgassing at the start of the structural transformation that occurs during calcination. Another location within the CaCO_3 core is shown in Fig. 6.12. In this region the limestone structure has become broken and jagged. It is apparent from these pictures that although the shrinking core model assumes a reaction at the surface of an unreacted core, some reaction is taking place within the core.

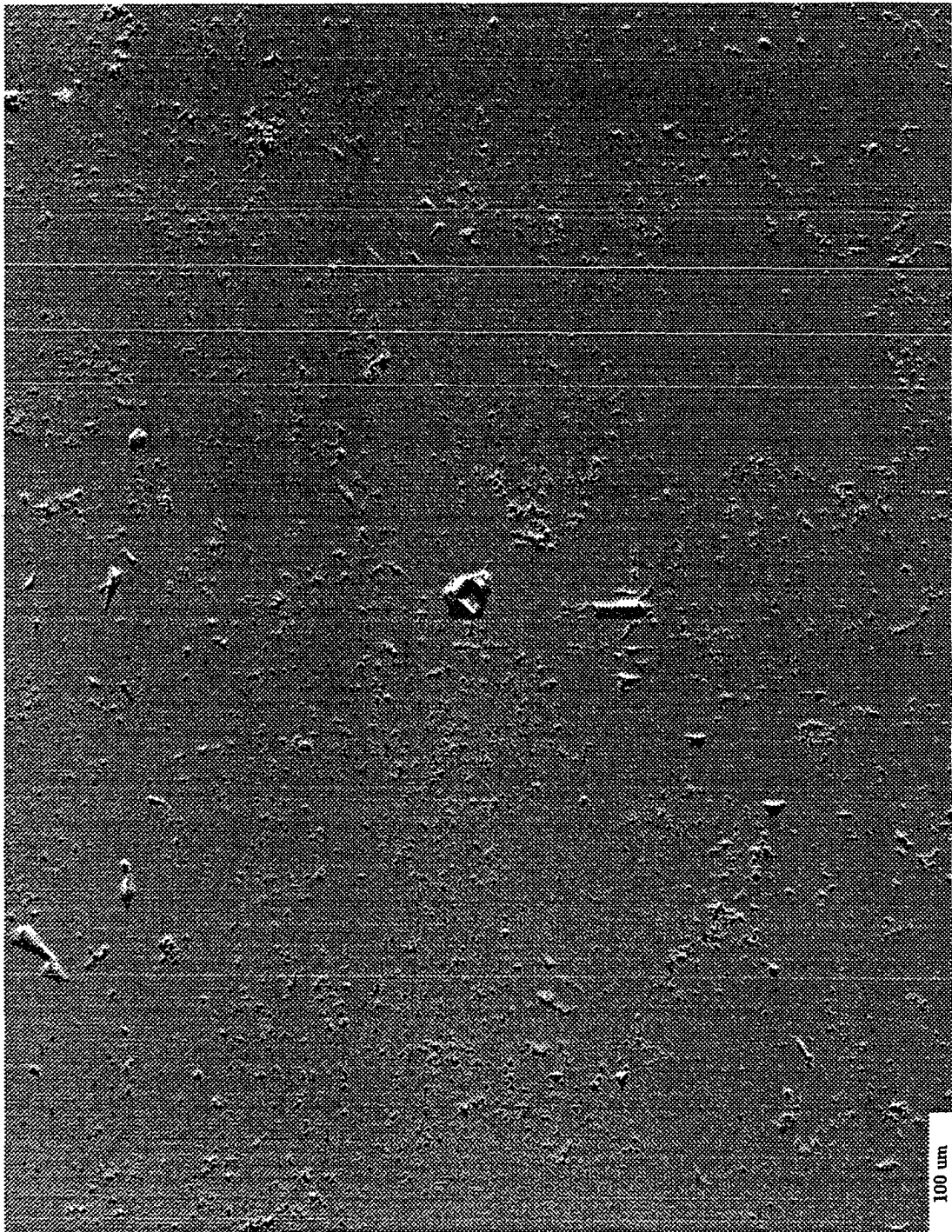


Figure 6.9 SEM photograph of unreacted limestone



Figure 6.10 SEM photograph of 2.58 mm limestone particle extracted after 2 minutes of reaction

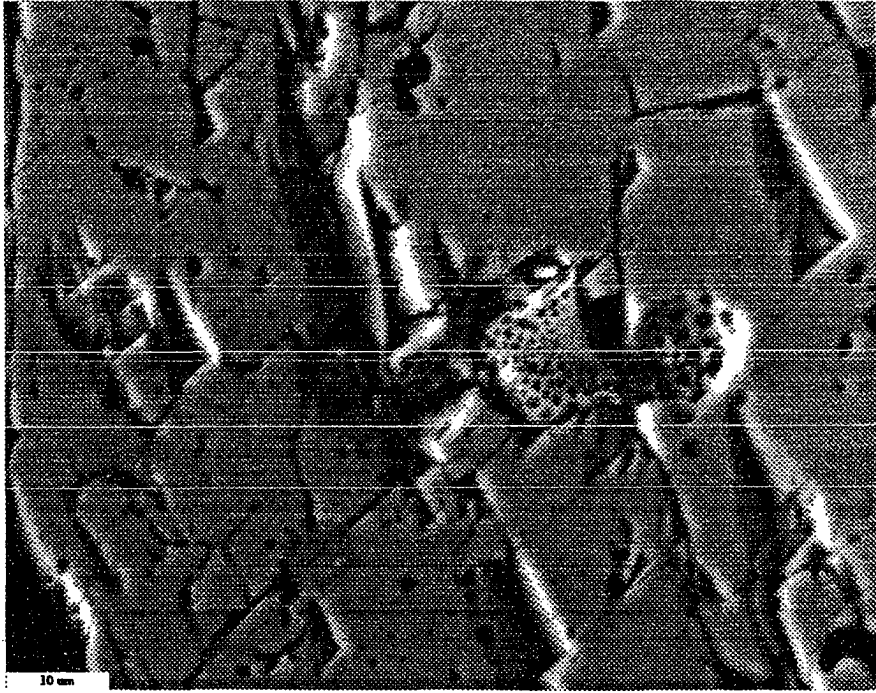


Figure 6.11 Region A of particle in Fig. 6.10

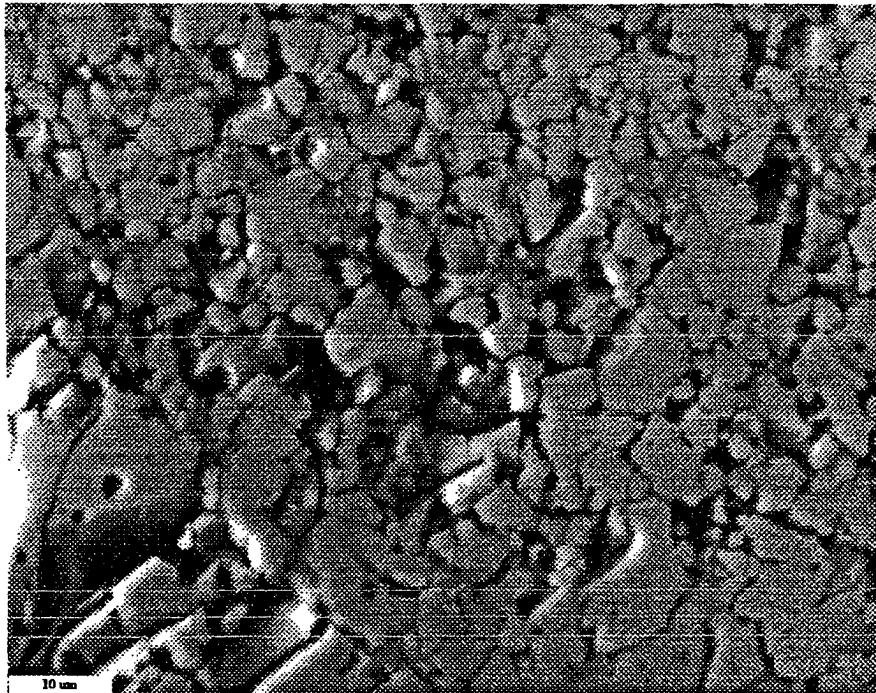


Figure 6.12 Region B of particle in Fig. 6.10

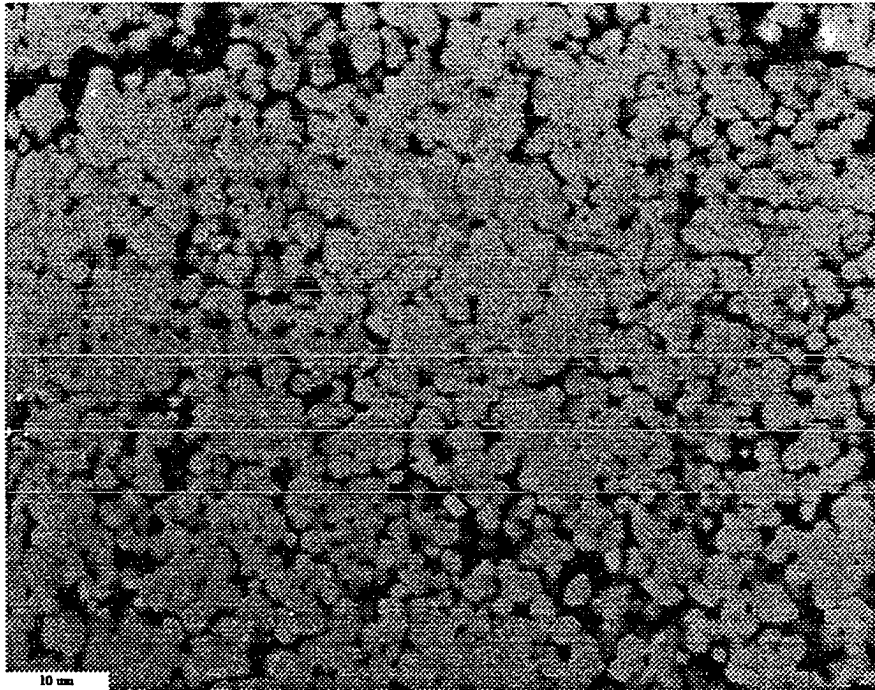


Figure 6.13 Region C of particle in Fig. 6.10

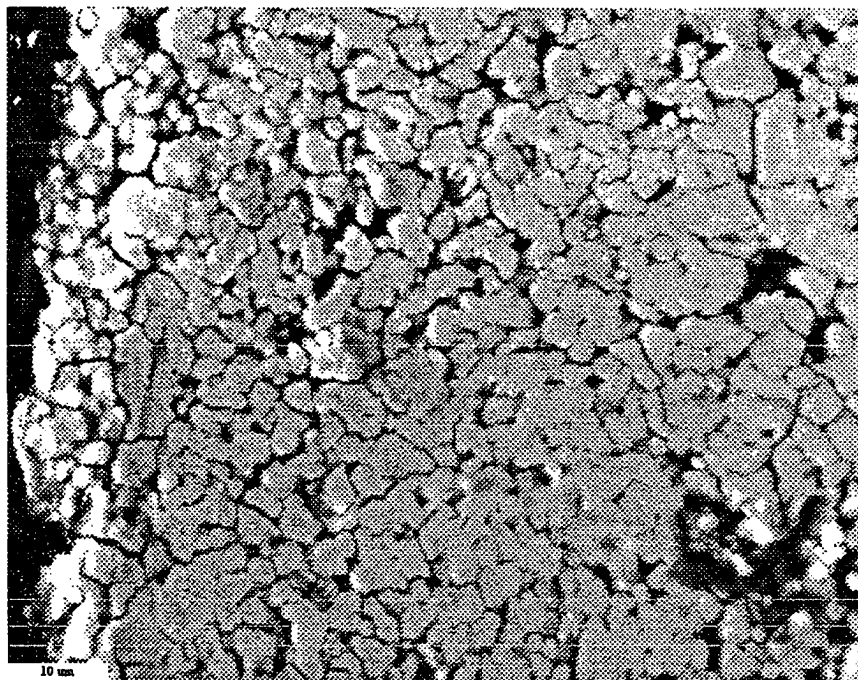


Figure 6.14 Region D of particle in Fig. 6.10

Structural changes also appear to be taking place within the calcined regions. The section of Fig. 6.10 identified as Region C is shown more fully in Fig. 6.13. In this region the sub-particles have become smaller and apparently smoother. This change in size and structure of the particle makes focusing the SEM more difficult. The structure seems highly porous. Near the center of the picture it appears that some of the small particles are sticking together. The sintering effect is noticeably more complete near the surface of the particle. Fig. 6.14 shows Region D of Fig. 6.10. In this region the pores have become smaller and the sub-particles seem to be conformed to one another. The bright region to the left of the particle is a result of sulfation beginning to take place at the particle surface.

This analysis suggests that initially during calcination a large surface area is formed. After a period of time the calcine sinters and loses much of its surface area. Several investigators [18-20] have studied the effects of calcination time and temperature on surface area. Higher temperatures in the outer portion of the particle may cause increased sintering rates. The importance of this finding is that increased surface area near the particle surface may cause higher sulfation reaction rates early in the transient. It is assumed that initially calcination takes place on the outer surface of the particle, and it produces the high surface area calcine that is characteristic of the intermediate region of Fig. 6.10. This would affect the size and formation of a sulfation reaction zone.

6.2.2 Surface area analysis

Surface area measurements were made on Gilmore City formation limestone calcined in the laboratory FBC at temperatures of 1200 K and 1123 K. These measurements were made on particles from 150 gram batches of limestone which were calcined in the combustor for 12 minutes. By the time of their extraction, the CO₂ concentration had returned to background for several minutes. Calcination at 1200 K resulted in a specific surface area of 11.32 m²/g using a nitrogen adsorption method, and

14.03 m²/g using a nitrogen desorption method. The surface area of the lime calcined at 1123 K was measured to be 13.86 m²/g and 15.28 m²/g for nitrogen adsorption and desorption methods, respectively. This result suggests that sintering is more significant at higher temperatures.

Pore volume distributions for both samples show that the most of the pore volume generated in calcination surface area is created in pores with diameters of less than 0.1 μm. At higher temperatures the pores created have a larger diameter than those created at lower temperatures. The average pore diameter from BET analysis for the 1123 K particles was 0.0576 μm, while particles calcined at 1200 K exhibited a mean pore diameter of 0.0760 μm. The sintering process is clearly temperature dependent. Quantitative analysis of the differences in surface area within a single partially-calcined particle is probably not possible. However, Figs 6.13 and 6.14 seem to indicate that the calcine near the CaCO₃ core has a higher surface area than the calcine near the particle surface. Thus early in the sulfation transient the outer surface has a higher surface area but a smaller mean pore diameter. This may result in increased sulfation reaction rates early in the transient.

6.3 Transient Gas Analysis of Sulfation

An aim of this study was to develop methods to use transient gas analysis to characterize the sulfation process. As a first step toward this goal, a numerical model was developed to analyze the mechanisms of sulfation. This model was used to characterize the sorbent by fitting experimental data to the numerical solutions. The reaction rate coefficient, the effective diffusivity and the pore plugging time constant were determined by fitting this model to data from the laboratory combustor. After the numerical model results were validated, the simplifications discussed in chapter three were made in order to analyze data analytically for controlling mechanisms. Many transient batch tests were

conducted with a range of particle sizes, temperature, oxygen concentrations, and types of limestone. The simplified expressions for controlling mechanisms were applied to these data.

6.3.1 Comparison of transients to the sulfation model

The model developed to describe sulfation is a shrinking particle core model, modified to include a pore diffusivity that decays exponentially. The model solved Eqns. (3.50) - (3.53) numerically. The program code for this model is contained in the appendix. This model was also simplified first into equations (3.54) and (3.55).

$$-\frac{dr_{sc}}{dt} = \frac{[SO_2]_I \frac{M_{CaO}}{f_{CaO} \rho_{LS}}}{\frac{3m_{LS}}{Q\rho_{LS}r_p} \frac{r_{sc}^2}{r_p^2} + \frac{1}{h_s} \frac{r_{sc}^2}{r_p^2} + \frac{(r_p - r_{sc})r_{sc}}{D_{es}e^{-t/\tau_p} r_p} + \frac{1}{k_s}} \quad (3.54)$$

$$\frac{[SO_2]_R}{[SO_2]_I} = \frac{1}{1 + \frac{3m_{LS}}{Q\rho_{LS}r_p} \left(\frac{1}{\frac{1}{h_s} + \frac{(r_p - r_{sc})r_p}{D_{es}e^{-t/\tau_p} r_{sc}} + \frac{1}{k_s} \frac{r_p^2}{r_{sc}^2}} \right)} \quad (3.55)$$

Figure 6.15 shows how the full model was fit to transient results for four different particle sizes. Parameters used to fit these curves are tabulated in Table 6.6. For the three larger particle size tests shown in the Fig. 6.15, the model gives good correspondence to the experimental transient. The 0.328 mm particle size is affected by elutriation, which causes the experimental transient to return to background sooner than the model predicts.

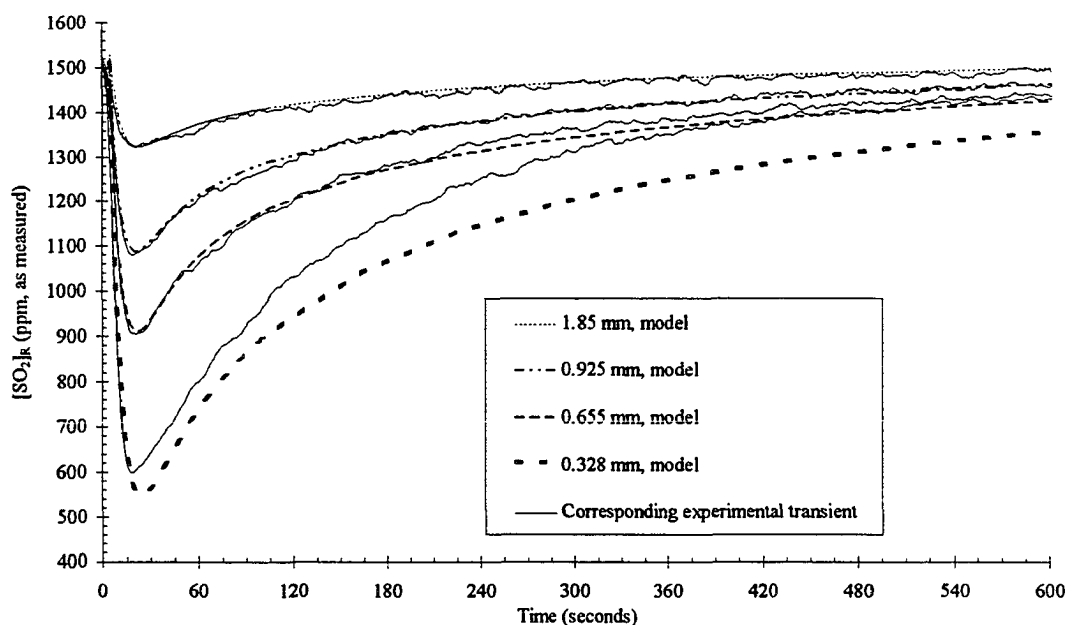


Figure 6.15 Comparison of shrinking particle core model vs laboratory SO_2 transients ($U_o = 1$ m/s, $T_{\text{bed}} = 1123$ K, $m_{\text{LS}} = 20$ grams, $[\text{SO}_2]_i = 1510$ ppm)

Table 6.6 Parameters used in model for Figure 6.15. (Gilmore City limestone, $m_{\text{LS}} = 20$ g., $T_{\text{bed}} = 1123$ K, $U_o = 1$ m/s)

Parameter	Value	Method of determination
k_s	1.9 m/s	fit (depends on h_s , correlation used)
D_{es}	$1.7 \times 10^{-6} \text{ m}^2/\text{s}$	fit
τ_p	760.0 s	fit
h_s	0.53 m/s (0.925 mm)	Froessling correlation

Elutriation can be considered in the model through the use of an elutriation time constant, τ_e . To account for elutriation, the batch mass, m_{LS} , in Eqns. (3.54) and (3.55) should be multiplied by $\exp(-t/\tau_e)$. The resulting expressions are:

$$-\frac{dr_{sc}}{dt} = \frac{[\text{SO}_2]_I \frac{M_{\text{CaO}}}{f_{\text{CaO}} \rho_{\text{LS}}}}{\frac{3m_{\text{LS}} e^{-t/\tau_e} r_{sc}^2}{Q \rho_{\text{LS}} r_p} + \frac{1}{h_s} \frac{r_{sc}^2}{r_p^2} + \frac{(r_p - r_{sc}) r_{sc}}{D_{es} e^{-t/\tau_p} r_p} + \frac{1}{k_s}} \quad (6.7)$$

$$\frac{[SO_2]_R}{[SO_2]_I} = \frac{1}{1 + \frac{3m_{LS}e^{-t/\tau_e}}{Q\rho_{LS}r_p} \left(\frac{1}{\frac{1}{h_s} + \frac{(r_p - r_{sc})}{D_{es}e^{-t/\tau_p}} \frac{r_p}{r_{sc}} + \frac{1}{k_s} \frac{r_p^2}{r_{sc}^2}} \right)} \quad (6.8)$$

Colokyan and Levenspiel [55] give a correlation for the elutriation rate constant which is useful in analyzing the results of these experiments. This correlation is strongly dependent upon the sphericity of the particle, however.

Because of the limits of flow and chemical conditions available when performing testing in a laboratory combustor, analysis of the smaller particles which elutriate is problematic. The low velocities used to eliminate elutriation also result in lower bed temperatures, which inhibit calcination and sulfation. For smaller particles, diffuse interface models may be needed to correctly model behavior in the particle. A diffuse interface model developed by Mantri *et al.* [31] provides a test for the applicability of a shrinking core model vis-à-vis a zone model. Analysis using this model suggests that the shrinking core model is strictly valid for all particle sizes greater than 700 microns if the effective diffusivity does not change. With an exponentially decaying effective diffusivity, the shrinking core model should be valid for all particle sizes tested in this study.

One reason for the good fit on the remaining transients is that three important model parameters were adjustable. The chemical reaction rate coefficient, k_s ; the pore diffusivity, D_{es} ; and the pore plugging time constant, τ_p , were adjusted to allow the model to fit the data. Constant values for these three parameters were found so that multiple transients of varying particle diameter would all fit the model. Normally, fitting a model to curves by adjusting three parameters would not be a sufficient validation of a model. In

this case, the simultaneous fitting of several transients, together with supporting particle analysis, assists in substantiating the model.

Two correlations for the film mass transfer coefficient, h_s , were used in the model. The first was a correlation for isolated single spheres given by Froessling [49]:

$$Sh = \frac{h_s d_p}{D_{es}} = 2 + 0.6 Re^{\frac{1}{2}} Sc^{\frac{1}{3}}. \quad (6.1)$$

A similar correlation that is developed specifically for char combustion in bubbling fluidized beds is given by LaNauze [50]:

$$Sh = \frac{h_s d_p}{D_{es}} = 2 \varepsilon_b + 0.69 Re^{\frac{1}{2}} Sc^{\frac{1}{3}} \quad (6.2)$$

The value of h_s between the two correlations does not change significantly, but a small change in h_s may require a large change in the value of k_s in order to fit the data. At time zero the core radius equals the particle radius, and Eqn. (3.55) simplifies to:

$$\frac{[SO_2]_O}{[SO_2]_I} = \frac{1}{1 + \frac{3m_{LS}}{Q\rho_{LS}r_p} \left(\frac{h_s k_s}{h_s + k_s} \right)} \quad (6.9)$$

The smaller of h_s and k_s will control sulfation initially. Using the LaNauze or the Froessling correlation, the value of h_s is determined for several particle sizes. Then k_s is adjusted to one number which provides the best fit for the lowest point of the transients. The Froessling correlation resulted in a value for k_s of 1.9 m/s. The values h_s using the LaNauze correlation were greater, and depended on the value of ε_b assumed.

The value of k_s could not be evaluated experimentally in a laboratory combustor.

Consideration was given to increasing the film mass transfer coefficient to a point where chemistry rather than film mass transfer would control the early reaction. Increasing bed velocity, decreasing particle size, and lowering the bed temperature would all have the effect of increasing the film mass transfer coefficient. Unfortunately, elutriation limited the extent that particle size and bed velocity could be varied. Temperature could not be reduced enough to impact the chemical rate constant without significantly changing the calcination process.

Values for k_s in the literature vary widely. Most investigators [5,6,24] base the value on the specific surface area of the limestone, while others base k_s on the area of grains in the particle [36]. The meaning of k_s is strongly attached to the model being used, such that values of k_s must be mathematically backed-out of initial rate data for comparison with shrinking core model k_s values. Sufficient data concerning the parameters used in the tests are not always available in the literature to convert reported values to equivalent shrinking particle core values of k_s .

The value of D_e used in the model fits shown in Fig. 6.15 is 1.7×10^{-6} m²/s. This value is lower than is used in the literature. Hartman and Coughlin [36] use a value of 7.5×10^{-6} m²/s. A larger value of D_e can be accommodated by the model when a value for the maximum local conversion, X_{mi} , is incorporated into the model by multiplying ρ_{CaO} by it in Eqn. (3.53) and ρ_{LS} by it in Eqn. (3.54) and (3.56). It is valid to add such a term because the increase in volume associated with the sulfation reaction allows only about 50% conversion without growth of the calcine grains [22]. When this addition to the model is made, the value of D_e begins to approach the larger values found in the literature.

The pore plugging time constant used in the model is empirical. Other methods are available in the literature [36, 37] to account for the decrease in pore diffusivity, but they do not lead to ordinary differential equations and time constants. They also require detailed knowledge of particle parameters such as grain size and surface area. In

Fig. 6.15, the value of τ_p is a constant 760 seconds for the four particle sizes.

Analysis using this numerical model highlights the controlling mechanism. For all particle sizes pore-plugging is ultimately the controlling mechanism. There is some mixed control at early times, however. Figure 6.16 shows the values for the resistances to reaction for the four controlling mechanisms for the 0.655 mm particle shown in Fig. 6.15. The time period shown includes the 30 to 90 second time period for which τ_s is analyzed in section 6.3.3. For this smaller particle size, both film diffusion and bed mixing provided a significant resistance to molar flux at the particle surface for early times. Figure 6.16 shows that bed mixing is somewhat more important than film diffusion for the 0.655 mm particle.

Figure 6.17 shows the change in the resistances for a larger, d_p equals 1.85 mm,

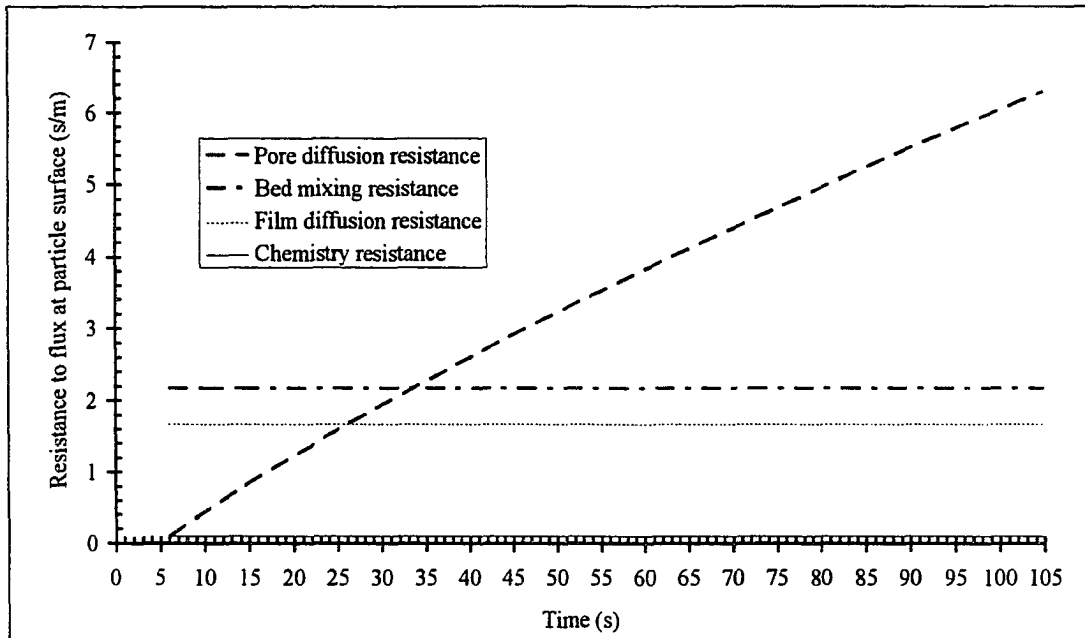


Figure 6.16 Resistances to sulfation for 0.655 mm diameter particle. ($T_{bed} = 1123$ K, $m_{LS} = 20$ grams, $U_o = 1.1$ m/s. Fit parameters are: $k_s = 500$ m/s, $D_{es} = 1.7 \times 10^{-6}$ m/s, and $\tau_p = 760$ s. La Nauze correlation used for h_s).

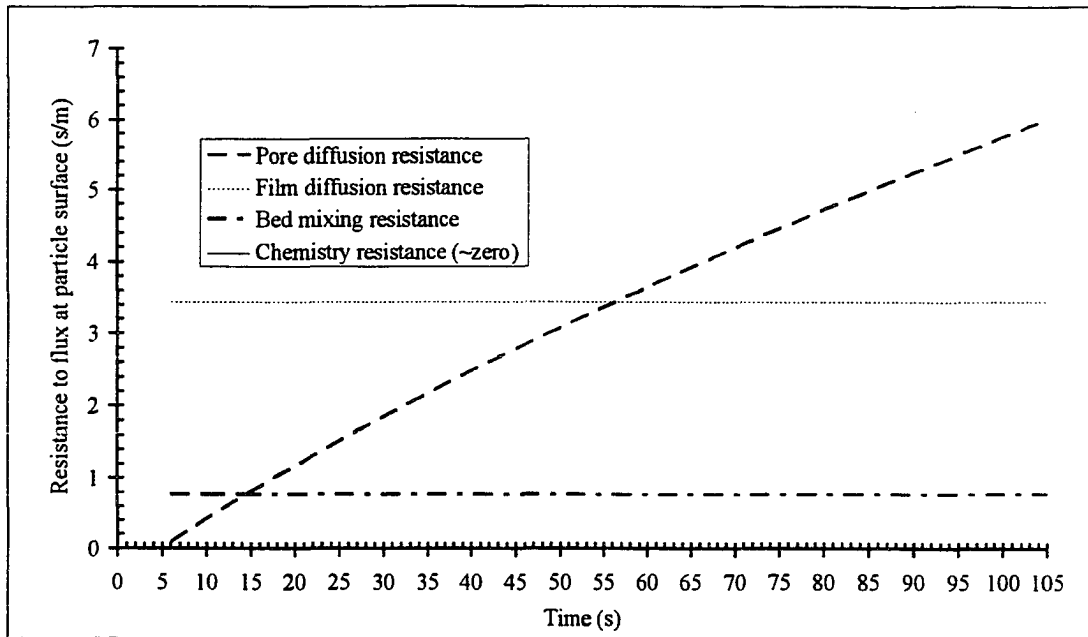


Figure 6.17 Resistances to sulfation for 1.85 mm diameter particle. ($T_{bed} = 1123$ K, $m_{LS} = 20$ grams, $U_o = 1.1$ m/s. Fit parameters are: $k_s = 500$ m/s, $D_{es} = 1.7 \times 10^{-6}$ m/s, and $\tau_p = 760$ s. La Nauze correlation used for h_s).

particle. For larger particles pore plugging is still the ultimate controlling resistance. At early times these large particles also exhibit mixed control, but film diffusion is more significant than bed mixing.

Further refinements to the numerical model are possible. The full model which was used can be converted to a shape-generalized form using Eqns. (3.56) and (3.57) to account for non-spherical particles. It is expected that this model could be refined to handle several classes of particle sizes by adding more equations. Additionally, analysis of the effect of temperature on sulfation has not been done using the full model, but would be fairly simple to do.

6.3.2 Results compared to model simplifications

Initial validation of the full sulfation model was done by fitting the model solutions to experimental SO₂ transients. Characterization of sulfation can be accomplished more directly, however, by transforming the data into the simplified forms developed in chapter three. The simplified equations were developed by assuming a variety of controlling mechanisms. Comparing the data from the transients to these simplified expressions should give some insight into the nature of sulfation. Four experiments are used to check four controlling mechanisms. These experiments are batch tests with one large (2.58 mm) and one small (0.55 mm) particles size, run at a high (1168 K) and low (1036 K) temperature. These extreme values are used to highlight differences in the controlling mechanism in sulfation.

If sulfation is controlled by the chemical reaction rate, the transient data can be changed into a form indicated by Eqn. (3.64),

$$\frac{\frac{[SO_2]_I - 1}{[SO_2]_R} - 1}{\frac{[SO_2]_I - 1}{[SO_2]_O}} = e^{-t / \tau_{sk}}, \quad (3.64)$$

where $\tau_{sk} = r_p f_{CaO} \rho_{LS} / (2k_s [SO_2]_I M_{CaO})$. A log-linear plot of the data should then yield a straight line for early times, with a slope of $1/\tau_{sk}$. In Fig. 6.18 this is done for the four extreme size and temperature experiments. The slope of the function is initially high because of a high reaction rate and a small time constant, but it continuously decreases to a lower slope, indicating lower reaction rates and a longer time constant. The non-linearity of the curve at early times suggests that chemistry is not rate limiting. Analysis of the effects of particle size and temperature are considered in The curves become straight near the end of the transient, and for the larger particles, the curve is straight for a large

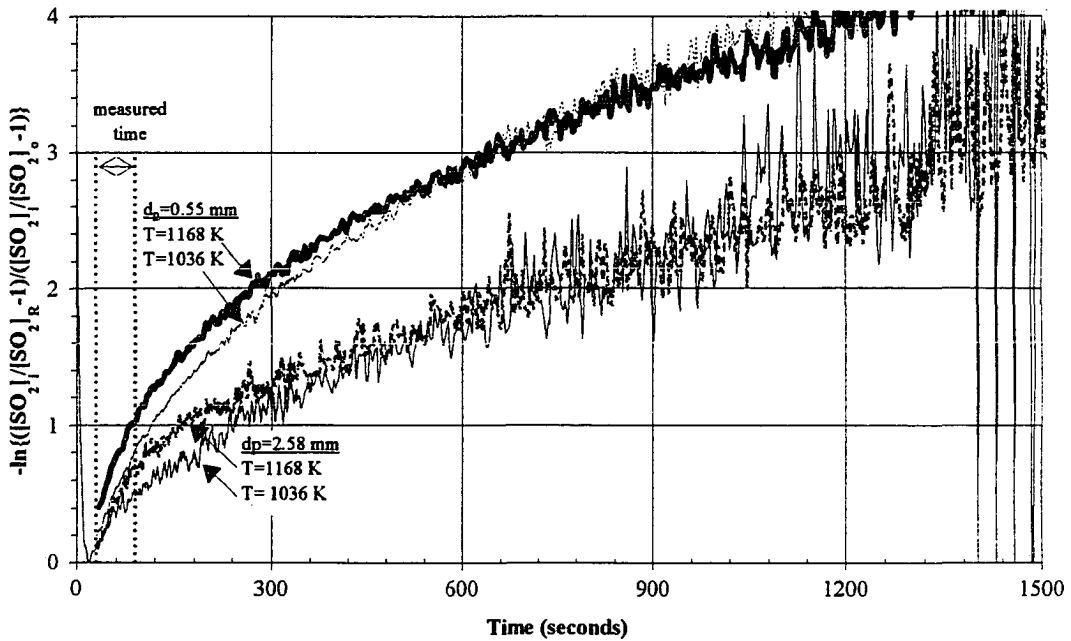


Figure 6.18 Time constant chart to evaluate chemistry control. (30 grams Gilmore City formation limestone, $U_o = 1.1$ m/s, $[\text{SO}_2]_I = 1500$ ppm)

portion of the transient, but not the initial portion. This is probably indicative of some other mechanism, which will become more apparent as the other equations are analyzed. It is also important to realize that Eqn. (3.64) is strictly valid only for short times.

Analysis of time constants determined from this function do have some meaning early in the reaction. When taken together, observed activation energies and particle size dependences give additional insight into the controlling mechanism. Since the slope is not constant, measurement of the time constant is dependent upon the time period being analyzed. The time period used for analysis in this study was from 30 to 90 seconds. This time period gives a good indication of the initial reaction rate.

Analysis in chapter three showed that film mass transfer control would result in a constant outlet concentration. This can be seen in Eqn. (3.66):

$$\frac{[SO_2]_R}{[SO_2]_I} = \frac{1}{1 + \frac{2c_2}{d_p} h_s} \quad (3.66)$$

This equation is useful, however, because the initial SO_2 concentration, $[SO_2]_0$, can provide insight into the initial controlling mechanism. Because the core and particle radii are equal at time zero, diffusion resistance is zero, and the initial outlet concentration is a function of h_s and k_s . Recognizing this, Eqn. (3.66) can be rewritten and expressed as:

$$\frac{[SO_2]_I}{[SO_2]_R} - 1 = \frac{2c_2}{d_p} \frac{h_s k_s}{(h_s + k_s)} \quad (6.10)$$

As can be seen in the Froessling and La Nauze correlations [49, 50], Eqns. (6.1) and (6.2), h_s has size dependence of $1/d_p^{1/2}$ to $1/d_p$. By plotting $1/([SO_2]_I/[SO_2]_R - 1)$ versus d_p on a log-log plot we can find the size dependence of the function of h_s and k_s . If film mass transfer provides a more significant resistance to reaction than chemistry, the slope should be close to 1.5 to 2. Since there is no size dependence on k_s , a slope close to 1.0 would demonstrate chemistry control.

The results of this analysis are plotted for four particle sizes and six temperatures in Fig. 6.19. The data points are for the minimum $[SO_2]_R$ during the reaction, since instrument time delay does not allow measurement of $[SO_2]_0$. Along with the data points, regressions are shown which show a strong consistency. The slopes of the curves are 1.37 ± 0.027 . The slopes of these lines do not appear to have any significant variation with temperature. The lack of temperature dependency, along with a value close to 1.5, supports the notion that film mass transfer provides a more significant resistance to the

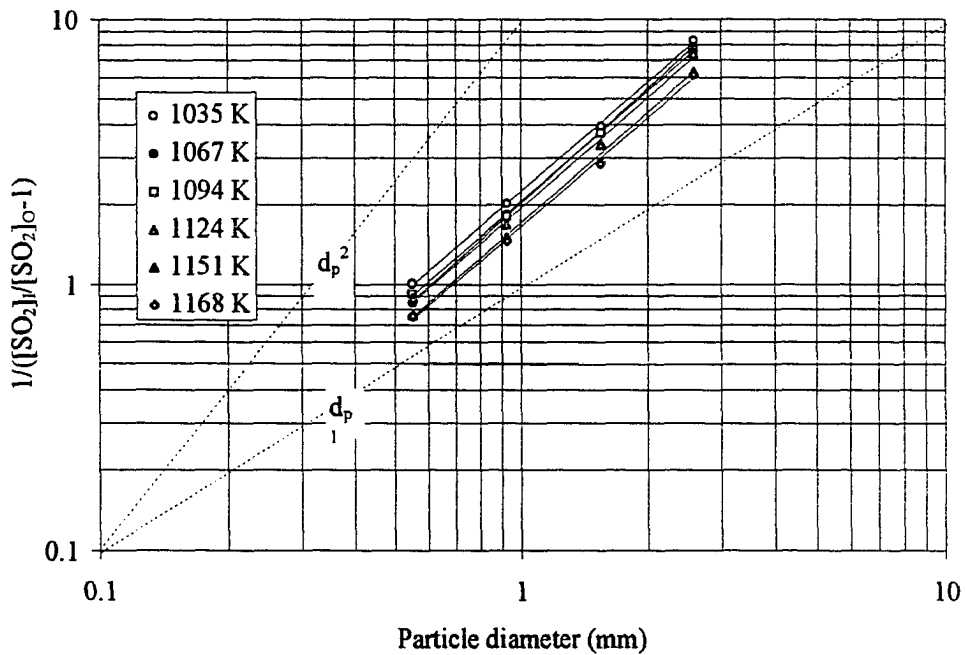


Figure 6.19 Initial concentration chart used to evaluate film mass transfer control. (30 grams Gilmore City formation limestone, $U_o = 1.1$ m/s, $[SO_2]_I = 1500$ ppm)

initial reaction than does chemistry. This also corresponds to analysis using the full model where values of k_s were determined to be somewhat larger than the values of h_s .

If pore diffusion with a constant effective diffusivity is the controlling mechanism, the transients can be plotted according to,

$$\left(\frac{[SO_2]_I}{[SO_2]_R} - 1 \right)^{-2} = \frac{1}{\tau_{sd}} t, \quad (3.76)$$

where $\tau_{sd} = c_2^2 D_{es} / 2c_{1s} L^2$. Results for the four sample transients are shown in Fig. 6.20.

For the small (0.55 mm) particles the result is a smooth curve with a continuously increasing slope. Figure 6.20 gives the appearance that a line may be drawn to determine τ_{sd} for these small particles at early times. By reducing the scale of the concentration

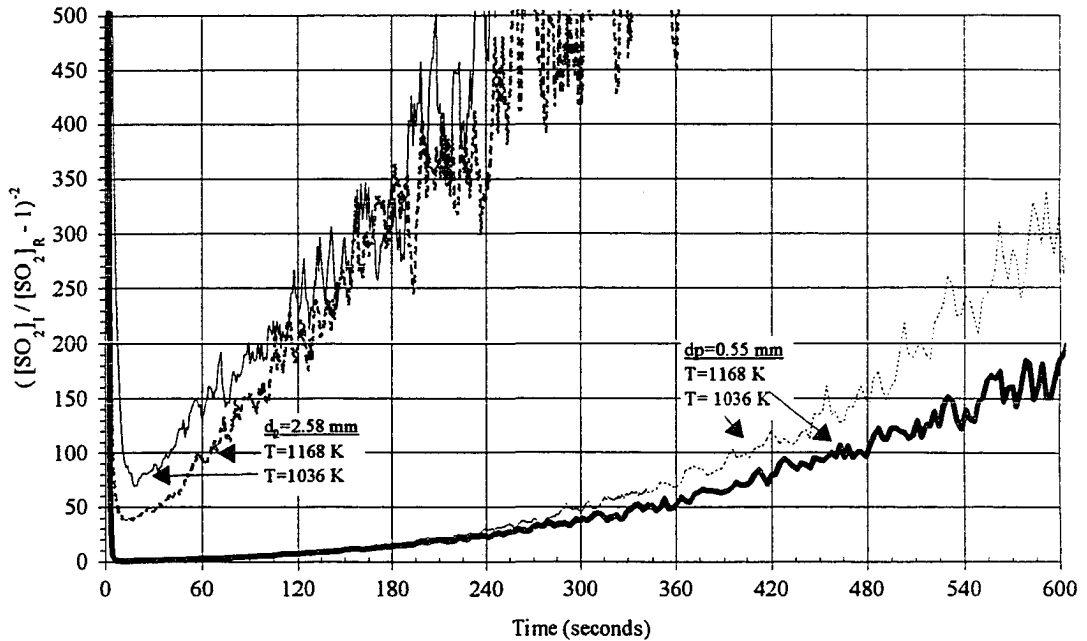


Figure 6.20 Time constant chart to evaluate pore diffusion control. (30 grams Gilmore City formation limestone, $U_o = 1.1$ m/s, $[SO_2]_I = 1500$ ppm)

function, however, it is apparent that the curve for these small particles does not yield a straight line at early times. The curve for the 2.58 mm transient shows large fluctuations, but appears to be linear, with a slope of around 1.5, making τ_{sd} equal to 0.667 seconds. From the definition of τ_{sd} in Eqn. (3.76) a value for D_{es} of 3.0×10^{-6} can be computed. This value is close to the value of D_{es} computed from theory-based correlations, and also from the full model if a maximum local concentration of 50% is applied. The linearity of the curve indicates that for larger particles pore diffusion may be controlling. For these particles, a constant diffusivity and a flat plate particle shape assumption give adequate results, at least for the early minutes of the reactions. The other possible explanation for this result is that film mass transfer is significant for larger particle sizes as shown in Fig. 6.19.

A final controlling mechanism that needs to be considered is pore-plugging. For sulfation controlled by pore-plugging, the transient should be changed into the form of Eqn. (3.83)

$$-\ln\left\{\left(\frac{[SO_2]_I}{[SO_2]_R} - 1\right)\sqrt{t}\right\} = \frac{1}{\tau_p}t - \ln\left\{\frac{c_2}{L}\sqrt{\frac{D_{es}}{2c_1S}}\right\}. \quad (3.83)$$

Results for the four cases under consideration are shown in Fig. 6.21. The transient for the larger particles is close to a constant value, corresponding to an infinite value of τ_p . This correlates with the analysis that gave a straight line slope for the analysis done with a constant value of diffusivity, that is, for pore diffusion control. The smaller particle tests result in fairly straight lines when plotted in this form. The slopes obtained from them

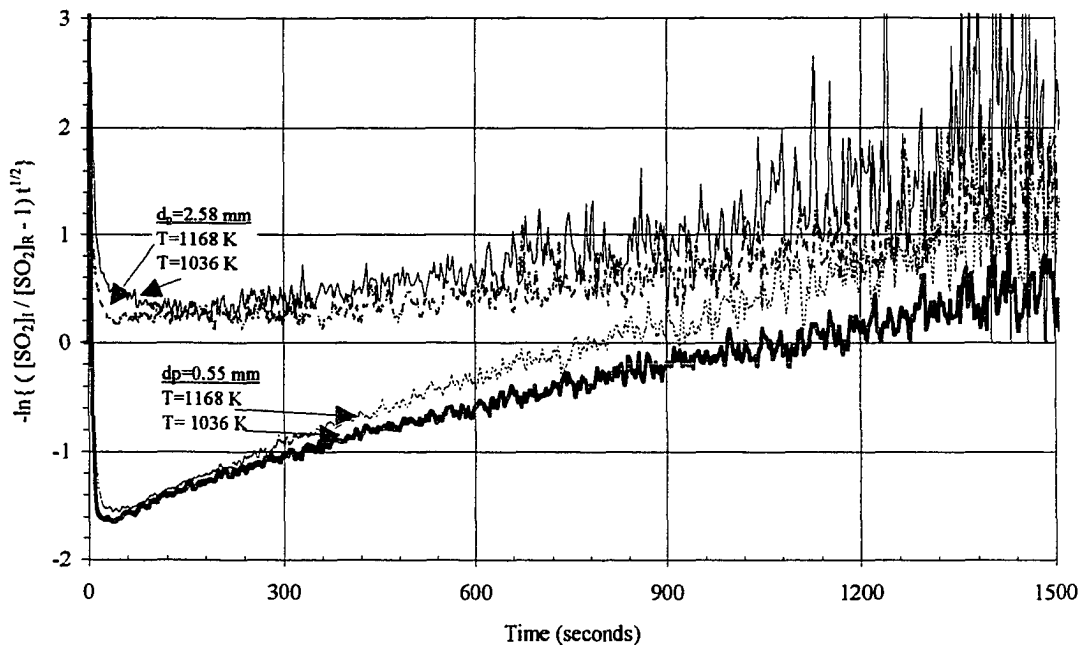


Figure 6.21 Time constant chart to evaluate pore plugging control. (30 grams Gilmore City formation limestone, $U_o = 1.1$ m/s, $[SO_2]_I = 1500$ ppm)

correspond to a value of τ_p of roughly 600 seconds. For these smaller particles it appears that pore-plugging controls sulfation from very early times in the reaction.

Examination of the controlling mechanism from these simplified expressions of the transients show a few common features. One is that particle size is a much more significant parameter than temperature. Examination of the figures for these simplified models shows that the major variations in the curve shape are due to differences in particle size. One reason for this is that chemistry is not rate limiting in any of the cases studied. Another common feature of these analyses is that near the end of the transient the slopes of the curves tend to approach a common constant value. The figures show only the first portion of the transients. In most cases the curves tend to end up with a common slope at the end. For the larger particles this is not quite as apparent since the proximity of the $[\text{SO}_2]_R$ to the background concentration leads to increased fluctuations in the data. This behavior suggests that pore plugging is the ultimate controlling mechanism in sulfation.

In some cases, such as is shown for large and small particles, the controlling mechanism for sulfation is clearly apparent over a large portion of the reaction. For particles sized between those shown, additional analysis must be done. At early times, all of the resistances are involved to some degree, and sometimes no single process dominates. To examine the sulfation reaction over a range of conditions, the effects of particle size, temperature, calcination conditions, and oxygen concentration are considered. Also tests on two other types of limestone are done for comparison with the Gilmore City formation limestone.

6.3.3 Effect of particle size on sulfation

Particle size is a major factor in the sulfation of limestone. The centers of larger particles remain unreacted, so a smaller conversion is achieved. Figure 6.22 shows extents

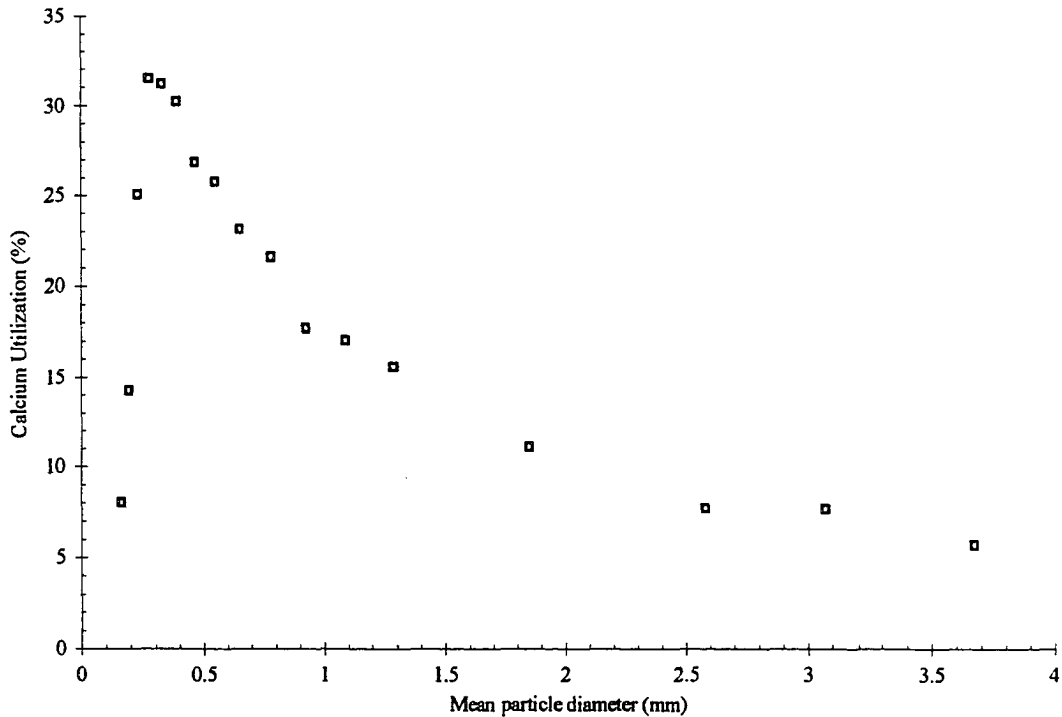


Figure 6.22 Calcium utilization for a range of 16 different particle sizes

of sulfation for a series of 18 experiments with different particle sizes. As particle size increases, the extent of sulfation decreases. The exception to this is for particles with diameters smaller than approximately 0.3 mm. These particles elutriate from the bed before they have time to react, and this elutriation leads to lower conversions.

As discussed in section 3.2.2, the sulfation time constant, τ_{sk} , should be proportional to particle radius for sulfation controlled by the chemical reaction rate. Although this analysis does not apply directly to film diffusion and pore diffusion control, the size dependence is expected to be similar to that for complete sulfation, that is $d_p^{1.5}$ - d_p^2 for film diffusion and d_p^2 for pore diffusion. Figure 6.23 plots τ_{sk} versus particle diameter for various temperatures using data plotted in the form of Eqn. (3.64):

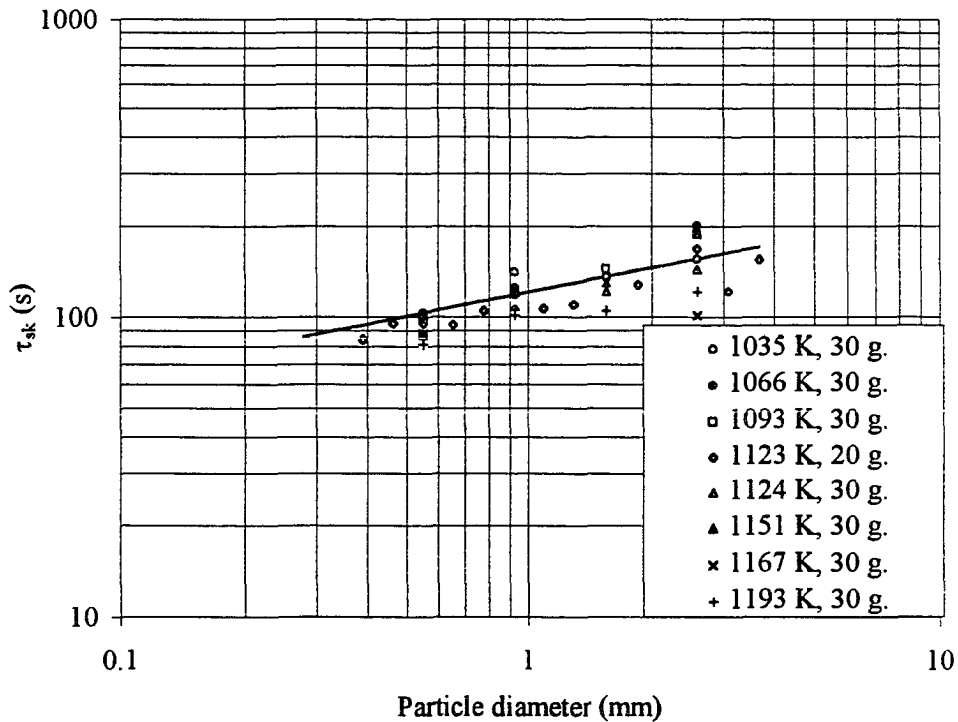


Figure 6.23 Plot of sulfation time constant versus particle diameter. (Gilmore City formation limestone, $U_o = 1.1$ m/s, τ_{sk} determined from Eqn. (3.64).)

$$\frac{\frac{[SO_2]_I - 1}{[SO_2]_R} - 1}{\frac{[SO_2]_I - 1}{[SO_2]_O}} = e^{-t / \tau_{sk}}, \quad (3.64)$$

A regression of the data on this log-log plot gives the size dependence of $\tau_s \propto d_p^{0.28}$. This correlation shows no clear controlling mechanism. One possibility is that bulk mass transfer provides a significant reaction resistance. As shown in section 3.3.2, if bulk mass transfer controls the reaction with chemistry as a secondary controlling resistance, the time constant would have no particle size dependence. Another possibility would be that significant pore plugging is taking place, since the pore plugging time constant is assumed to be independent of particle size.

6.3.4 Effect of temperature

The temperature effect on the extent of sulfation is shown in Fig. 6.24. This figure plots the extent of sulfation vs. bed temperature for four different particle sizes. The data agree in general with the commonly found result that the optimum temperature for sulfation is 1120 K, although the effect is not nearly as pronounced as is found by other researchers [56]. Lyngfelt and Leckner [56] compared the results of many investigators and found a maximum sulfation conversion closer to 1080 K when using bubbling fluidized bed boilers and laboratory FBC's, and a rapid drop-off of conversion at higher temperatures. They argue that in bubbling fluidized bed boilers, sorbent particles spend a larger percentage of their time in reducing regions. This is due to the location of the coal particles in the emulsion during combustion. The reduction in utilization at higher temperatures is not as drastic in circulating FBC's or when char is used instead of coal for

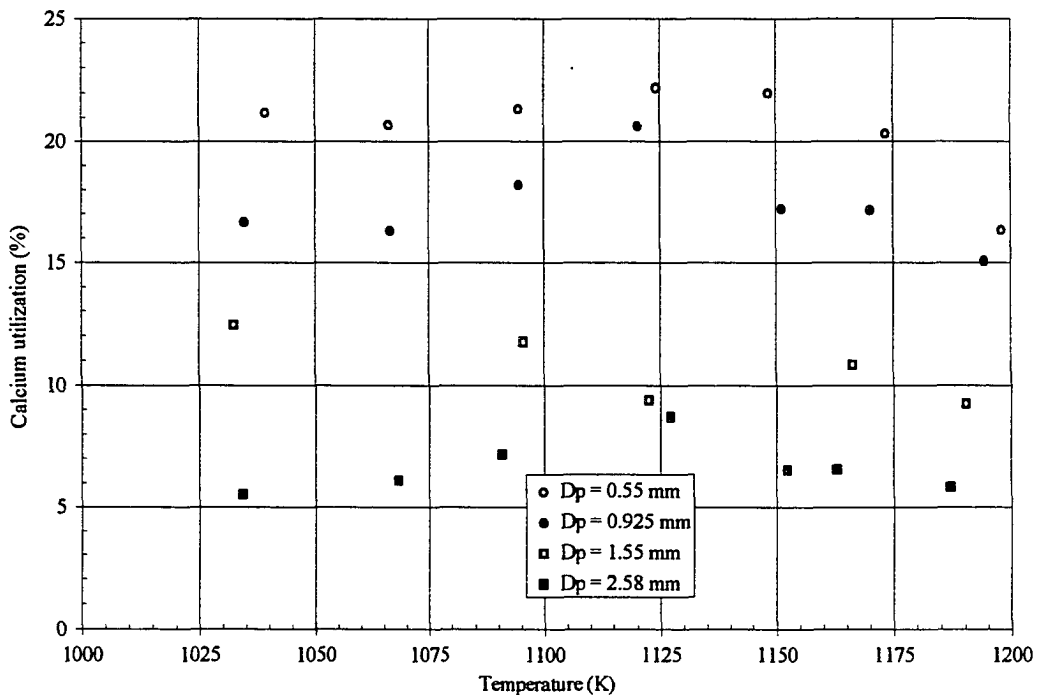


Figure 6.24 Calcium utilization as a function of temperature for four particle sizes

combustion. The laboratory experiments conducted in the present study were done with pre-mixed methane or propane as a fuel. Since reducing conditions do not exist in the emulsion phase of this laboratory FBC, a rapid drop off would not be expected by the theory of Lyngfelt and Leckner [56].

The effect of temperature on the sulfation time constant is seen in the activation energy chart (Fig. 6.25). In this figure the inverse of the sulfation time constant is plotted against the inverse temperature on a log-linear plot. The slope of this curve is proportional to the activation energy, based on an Arrhenius relationship. The values of sulfation activation energy range from 1.73 to 7.33 kcal/mol for limestone tests. These results are all substantially lower than those obtained by Mulligan *et al.* [6], who reported

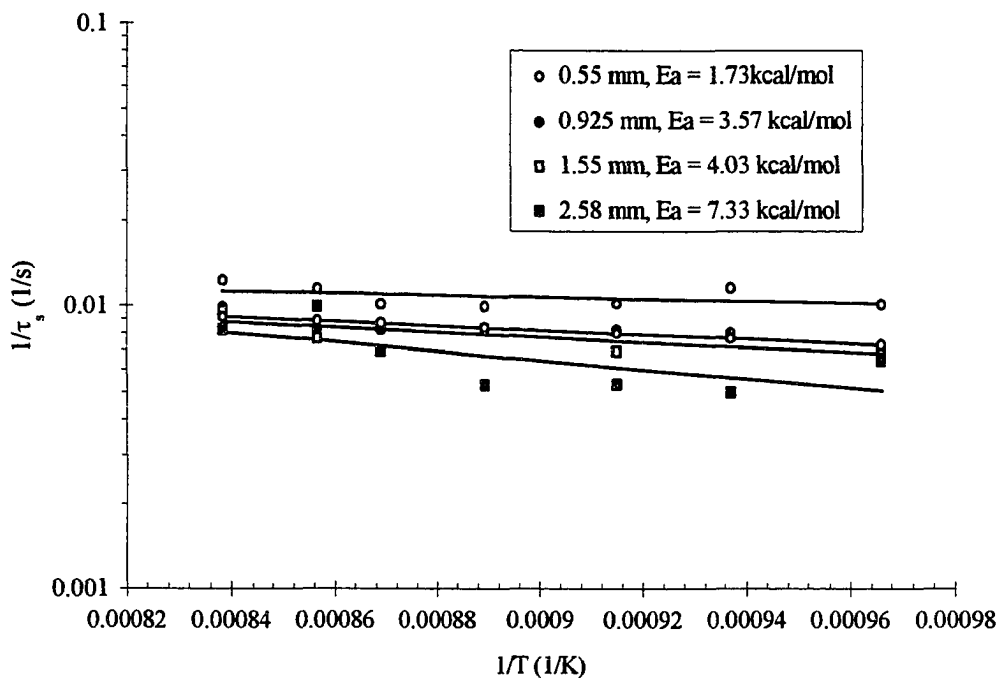


Figure 6.25 Determination of activation energy for sulfation for four particle sizes. (Gilmore City formation limestone, $m_{L,S} = 30$ g, $U_o = 1.1$ m/s, τ_s determined from Eqn. (3.64).)

17.08 kcal/mol and Wen and Ishida [57], who reported 17.48 kcal/mol. Bhatia and Perlmutter [24] analyzed data from Borgwardt [48]. They obtained an activation energy for chemical rate controlled sulfation of 13.47 kcal/mol, and for product layer diffusion controlled sulfation, an activation energy of 28.7 kcal/mol. Mulligan *et al.* [6] reported a product layer diffusion activation energy of 25.4 kcal/mol.

For chemistry limited sulfation the activation energy would be expected to have values closer to those of the researchers above. For pore diffusion limited catalytic reactions, the observed activation energy takes on a value from 1/2 to 1/4 of the chemical reaction activation energy. In the case of sulfation, however, diffusivity through the pores varies throughout the reaction because the pores get plugged by CaSO_4 as the reaction proceeds. The observed activation energy in this case would indicate the effect of temperature on pore plugging. However, pore diffusion control seems unlikely early in the reaction.

The two most likely reasons for the low activation energies are large resistances by film diffusion or bulk mass transfer. If bulk mass transfer is significant, this could also result in low initial activation energies. As shown in chapter three, bed mixing resistance, together with a secondary chemical reaction resistance, may result in a time constant which is independent of both particle size and k_s . This is especially true in the beginning of the reaction before chemistry and diffusion resistances build up.

For film diffusion control, the activation energy has a low value which corresponds to species transport (1-3 kcal/mol) [52]. The experimental values in Fig. 6.25 are consistent with this range for the smaller particles sizes. The larger particles from these experiments have higher activation energies than the smaller particles. This at first seems counter-intuitive since the smaller particles have higher film mass transfer coefficients, and might be expected to be less dominated by film diffusion. One explanation is that the larger particles are more affected by the calcination process. For the largest particles and

the lowest temperatures, the values τ_c and τ_s are approximately equal. The process and degree of calcination and sintering turn out to be very important to sulfation.

6.3.5 Effect of calcination conditions

In the shrinking particle core model, the calcination core recedes much more rapidly than does the sulfation core. It might be assumed that the two processes are independent, but this is far from the case. The extent and rate of sulfation will depend greatly on the extent of calcination, and the porosity and surface area developed during calcination. At early times, and particularly at lower temperatures, calcination and sulfation are taking place simultaneously.

In order to investigate how calcination affects sulfation, a series of tests were run with limestone which was calcined in the laboratory combustor in the absence of SO_2 . This lime was then removed from the bed and used in sulfation tests. Figure 6.26 plots the extent of sulfation vs. bed temperature for a 1.55 mm diameter particle size Gilmore City formation limestone under two conditions. In one set the sample had been pre-calcined by batching it into the combustor at $T_{\text{bed}} = 1200 \text{ K}$ with no SO_2 in the bed and extracting the particles after the CO_2 concentration returned to background. The recovered sample was then used for sulfation testing using a batch mass of 17.33 grams, which corresponds to 30 grams of uncalcined limestone. In the other set of experiments 30 grams of 1.55 mm limestone was batched using the normal procedure, which corresponded to the mass after 100% calcination.

The difference between the sulfation of lime and limestone can be seen by examining the extent of sulfation which is achieved for the two processes. Figure 6.20 shows that lime had improved extents of sulfation when compared to the original limestone. If the sample mass had been calculated to account for 80% calcination, as is justified by the calcination results shown in Fig. 6.4, the lime sample mass needed would

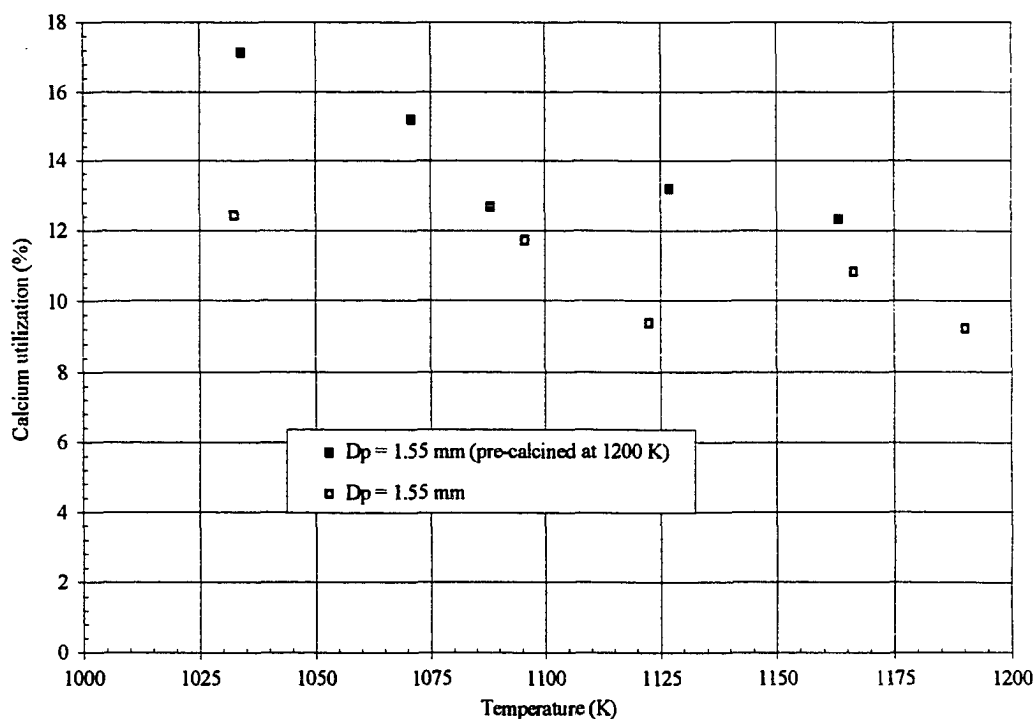


Figure 6.26 Calcium utilization as function of temperature for batch tests with lime and limestone.

be larger than 17.33 grams. This would have increased the extent of sulfation above that for limestone even more. At lower temperatures the difference in the extents of sulfation for the two cases is somewhat more pronounced. This is partially explained by the lower extents of calcination for temperatures below 1100 K, as seen in Fig. 6.7.

The effect of sulfation temperature on the lime and limestone sulfation transients is shown in Fig. 6.27. This figure shows the difference in activation energy between the 1.55 mm lime and limestone particles. The lime particles have an activation energy fairly close to that obtained by Bhatia and Perlmutter [24]. This suggests that sulfation is controlled by the chemical reaction rate at early times for pre-calcined sulfation. The absence of a convective flux of CO_2 from the particle for the lime reaction may result in a higher film

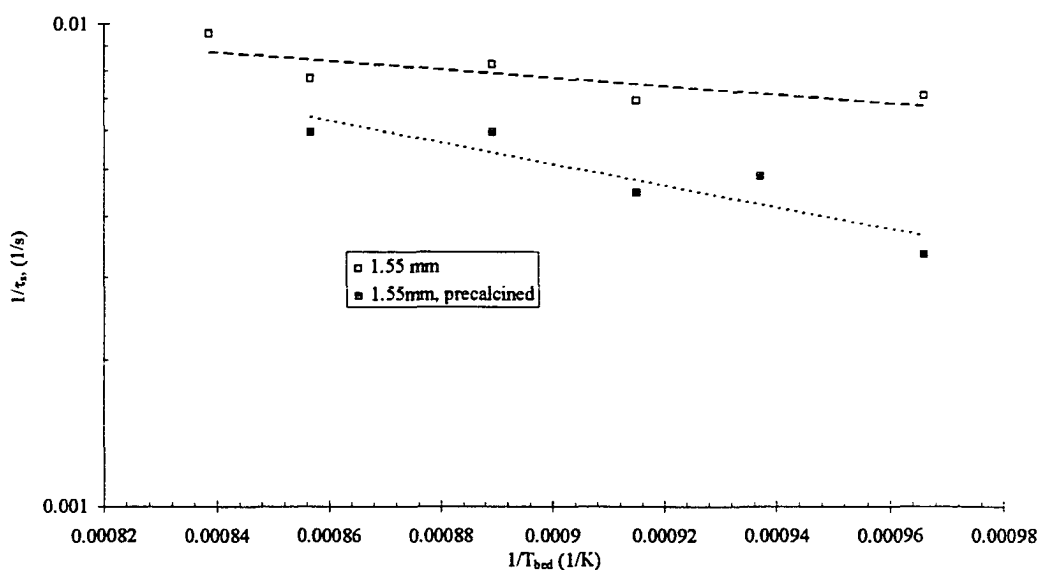


Figure 6.27 Determination of activation energy for sulfation comparing batch additions of limestone vs. lime. Activation energies are: limestone, 4.03 kcal/mol; lime, 10.3 kcal/mol

mass transfer coefficient. Preliminary calculations for particles of this size suggest that the convective flux of CO_2 away from the limestone particle is greater than the diffusion flux of SO_2 toward the particle for about one calcination time constant at 1123 K. For the larger particles, CO_2 convects away from the particle for longer durations. Figure 6.28 plots the convection flux away from the exterior of the particle vs. time based on the generation rate per particle using CO_2 transients. The resulting curves show that although the peak convective flux away from a particle is about the same for the four sizes, the flux lasts a longer time for the larger particles.

The difficulty with this explanation for lime's increased activation energy is that limestone tends to be more reactive than lime during the first few minutes of a transient. A typical comparison of transient curves for lime and limestone is shown as Fig. 6.29. This curve shows a lower initial reduction in SO_2 for the lime and a slower return to

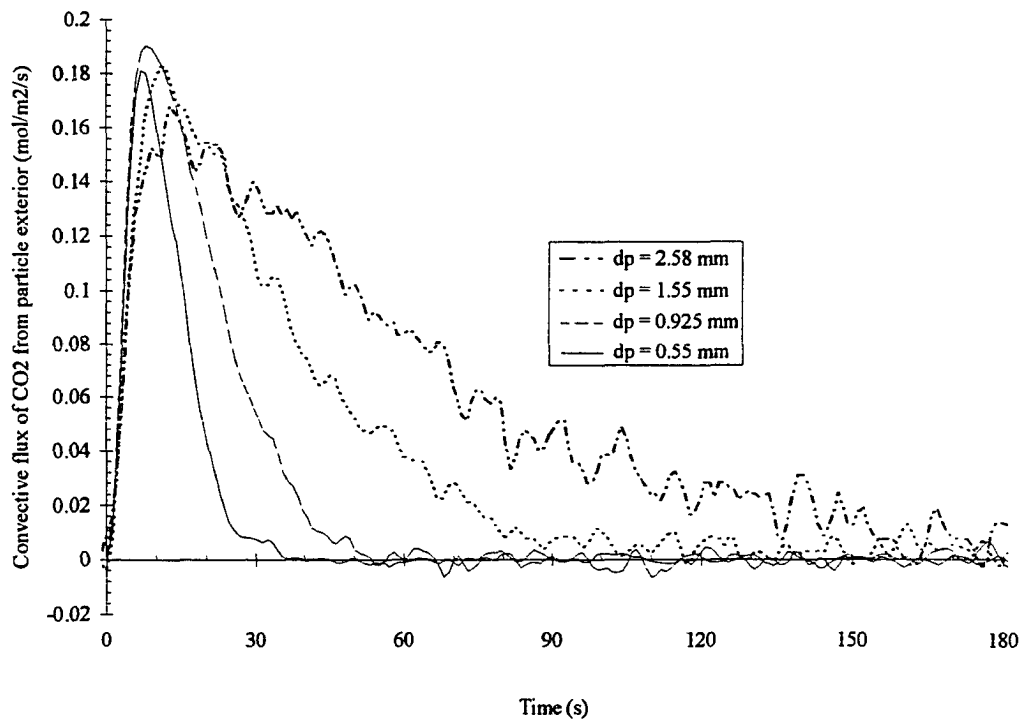


Figure 6.28 Predicted CO₂ flux from various sized particles based on CO₂ transients.

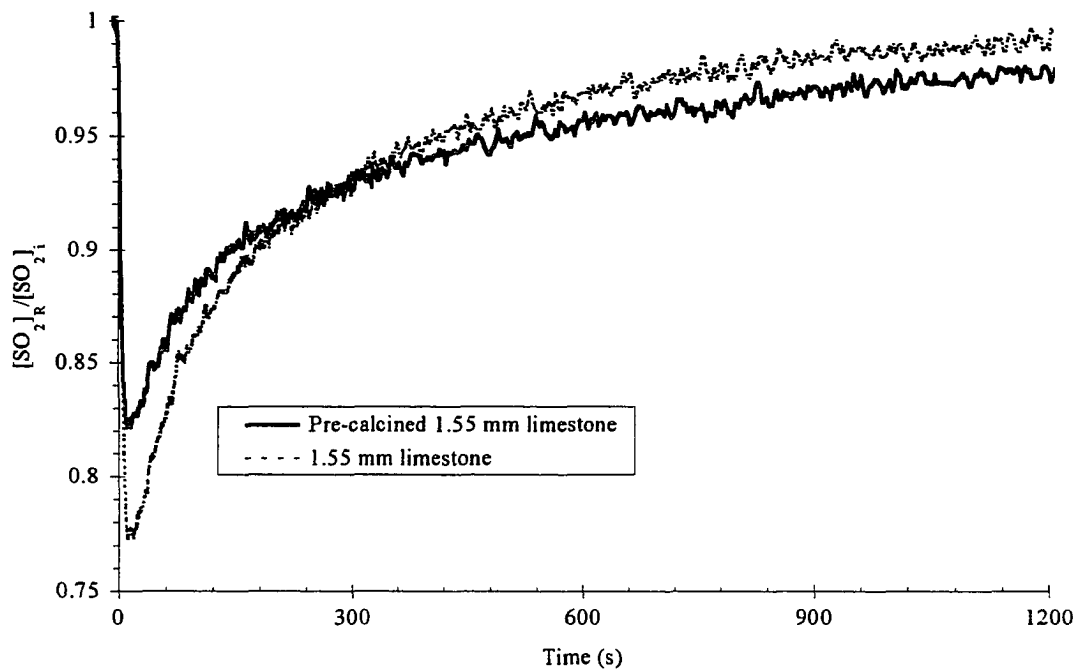


Figure 6.29 Normalized SO₂ transients for lime and limestone.

background indicative of a longer sulfation time constant. This lower initial SO₂ reduction and longer time constant were consistently observed in the transients for the five temperatures where lime and limestone performance was compared.

The fact that lime has a higher activation energy, but a lower initial reaction rate than limestone seems somewhat contradictory, but several possible explanations for this behavior exist. One reason might be that limestone may fracture upon batch addition, which would increase the initial surface area for reaction. A second involves the dust that exists on the limestone particles that is not present on the lime particles which have already been through the reactor once. Another reason may be that the assumption of complete calcination in the pre-calcining process is not valid. Finally, sintering of the calcine may give a different response for lime than is seen in the limestone tests. An examination of each of these four hypotheses is warranted in order to determine the reason for the difference in limestone and lime sulfation transients.

Some surface fracturing of the limestone does occur after a batch of limestone is added to the combustor. In the pre-calcination process calcined limestone is removed from the bed and screened to separate it from the sand. Smaller particles of limestone which are roughly the same size as the sand cannot be separated. It is estimated that the unrecovered lime is no more than a few percent of the total mass in the bed after pre-calcination. Additionally, lime may also fracture upon batch addition. The fracturing phenomenon is not considered to be significant enough to give the difference in the sulfation transients that is observed.

The second possible explanation involves dust that is present on the limestone, but is not assumed to be present on the lime. To examine this possibility tests were performed on limestone that was washed in a bucket until the water was no longer cloudy. The limestone was left to dry overnight under a fan. Figure 6.24 shows normalized SO₂ concentration vs. time for washed and unwashed Gilmore City formation limestone with a

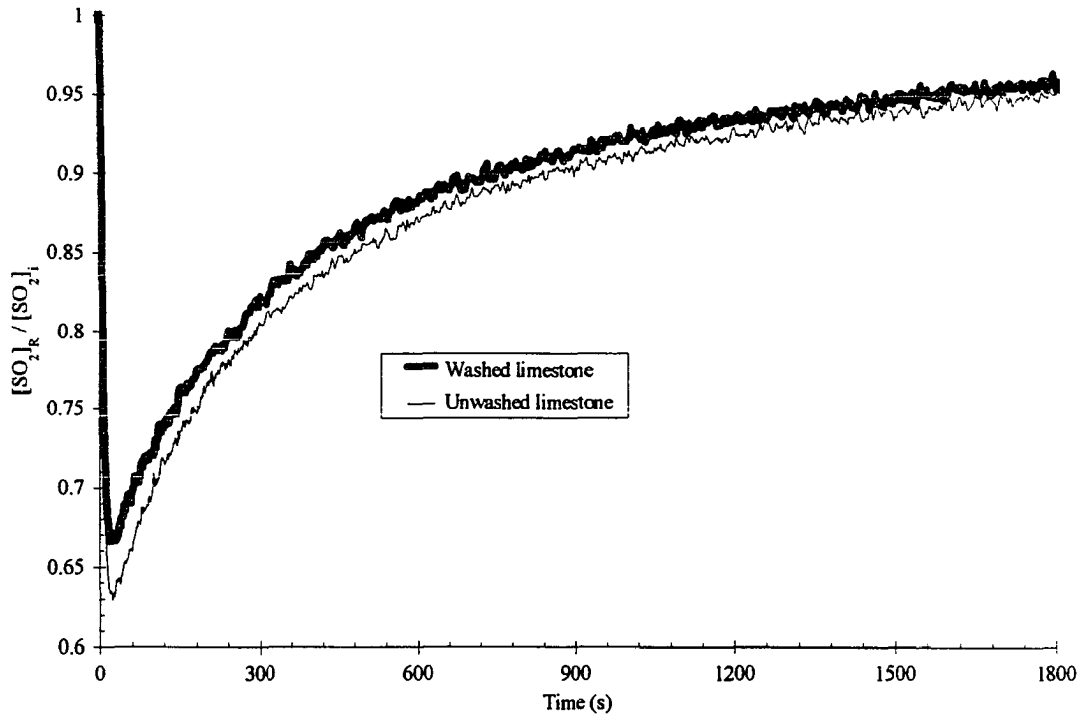


Figure 6.30 Comparison of normalized SO_2 transient for washed and unwashed limestone batch additions.

particle diameter of 2.58 mm. These tests were done with large batches of 150 grams in conjunction with other tests involving extracting particles for particle analysis. The initial reduction in SO_2 concentration is greater for the unwashed limestone. The extent of sulfation for the washed limestone is 82% of the unwashed limestone's extent of sulfation after 110 minutes. This long test period leaves room for error in the background level, however. The difficulty with this hypothesis is that the shape of the profile does not differ between the washed and unwashed limestone. Although the dust on the particles may be a consideration, especially for small particles, it does not appear to be causing the differences in the sulfation between lime and limestone.

A third hypothesis is that the mass used in the lime batches was determined incorrectly, since it assumes complete calcination of limestone. If a lower extent of calcination had taken place in the pre-calcining process, less calcium would be present in

the batch than was assumed, and the initial reduction of SO_2 concentration would be lower, as is seen in Fig. 6.30. Along with this, however, lime would have lower extents of sulfation than limestone, which it does not.

A final possible explanation involves sintering of the calcine. Calcination begins at the particle surface where it creates a large surface area consisting of small pores. Sintering begins to reduce pore surface area as soon as it is formed by calcination. In the case of the limestone addition, sulfur dioxide is present during this process to take advantage of the large surface area before it is reduced by sintering. The other effect of sintering is that in reducing the surface area by collapsing the small pores, the pores that remain are large pores. This has the effect of increasing the accessibility of the reacting species to the unreacted core. In this way larger conversions may take place, but at a slower rate. Particle analysis supports this hypothesis. In Fig. 6.6, the two outer zones of calcine in this particle may be an intermediate region which has been freshly calcined, and an outer region which has been sintered. Overall, sintering seems to be the most plausible explanation for the difference between lime and limestone sulfation transients.

6.3.6 Effect of oxygen concentration

Tests were also run to determine the effect of excess oxygen on sulfation of limestone particles. Different approaches have been used in the literature to account for the oxygen concentration. Some include oxygen in the rate equation while others incorporate it into the value of the chemical reaction rate coefficient. Figure 6.31 plots normalized SO_2 concentration vs. time for several batch tests of limestone at different oxygen concentrations. There was no discernible difference in the four transients. This is not unreasonable since there is no indication that the chemical reaction rate is limiting for sulfation under any of the conditions investigated in this study. The effect of oxygen concentration on the chemical reaction rate is therefore not measurable in this analysis.

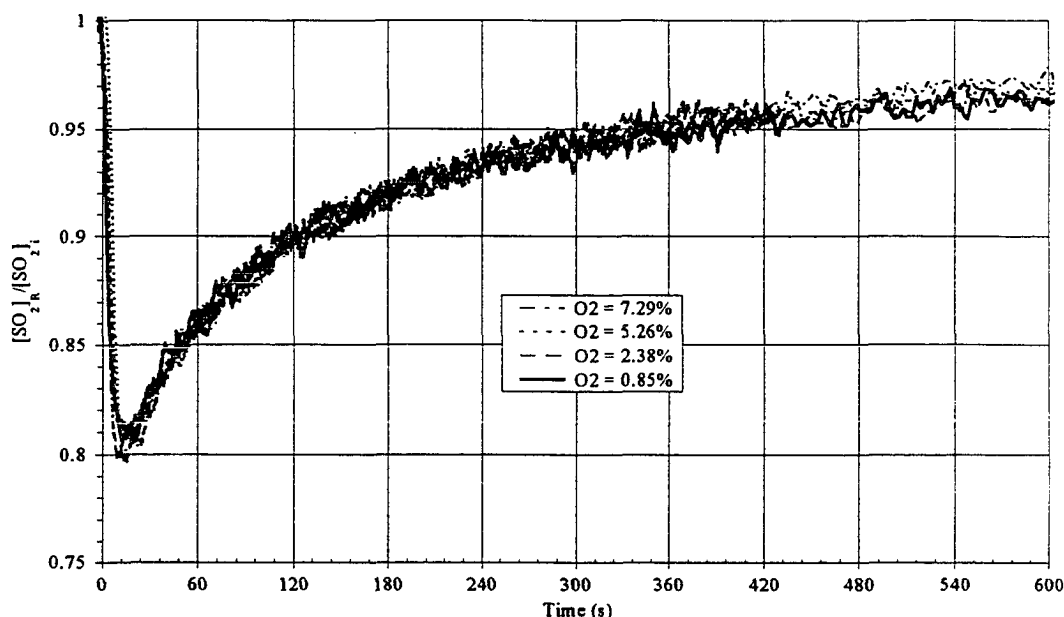


Figure 6.31 Transient SO_2 response for varying concentrations of O_2

6.3.7 Results for different limestone types

Figure 6.32 gives a comparison of sulfation transients for 0.655 mm batch tests for the three types of limestone tested. It is apparent that the Cedar Bay #1 limestone seems to give slightly better performance than the Gilmore City limestone, and the Nova Scotia limestone performs considerably worse. This might be expected due to the larger amount of impurities (mainly silicon) in the Nova Scotia limestone, as shown in Table 5.1.

The Nova Scotia limestone consists of 90.5% calcite while the others range from 96 - 98% calcite. This calcium fraction is considered in the analysis for the extent of sulfation. The performance of Nova Scotia limestone is substantially worse even with the lower calcium fraction (f_{CaCO_3}) that is used in Eqn. (5.6). Other researchers [6,2] have investigated limestones containing increased levels of SiO_2 and Al_2O_3 and found that they actually performed well. The difference is likely to be more attributable to structure than to chemical content. Results comparing the time constants and extents of calcination and sulfation for three limestones are shown in Table 6.7.

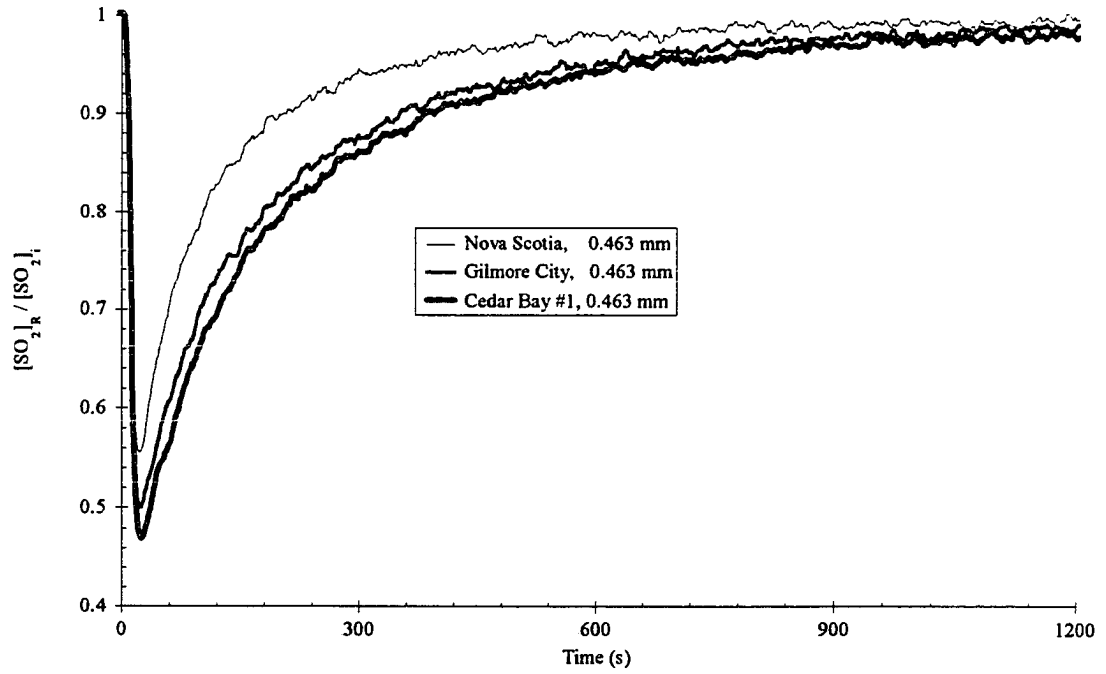


Figure 6.32 Comparison of normalized SO₂ transients for three limestones

Table 6.7 Time constants and reaction extents for three limestone types with various particle sizes. ($T_{bed} = 1123$ K, $U_0 = 1.1$ m/s, $m_{LS} = 20$ g.)

	Mean particle diameter (mm)	τ_c (s)	Extent of Calcination (%)	τ_s (s)	Extent of Sulfation (%)
Cedar Bay #1	0.231	4.59	92.8	58.8	30.2
	0.328	4.95	75.8	89.8	32.4
	0.463	5.02	77.8	91.1	31.0
	0.655	8.73	80.3	99.5	28.2
	0.925	12.3	85.3	128.	21.5
Nova Scotia	0.328	4.17	75.4	56.8	21.4
	0.463	9.83	84.4	69.7	17.0
	0.655	11.0	88.7	65.8	13.2
Gilmore City	0.165			21.14	8.02
	0.196			30.96	14.24
	0.231			43.08	25.05
	0.275			68.26	31.49
	0.328			76.09	31.18
	0.390			84.32	30.22
	0.463			95.04	26.86
	0.550			95.08	25.76
	0.655			94.08	23.10
	0.780			104.93	21.60
	0.925			105.90	17.67
	1.090			106.62	17.03
	1.290			110.09	15.57
	1.850			128.00	11.07
2.580			168.85	7.71	
3.075			121.87	7.66	
3.675			156.07	5.69	

6.4 Particle Analysis of Sulfated Particles

Particles of limestone reacted for different lengths of time were analyzed with a scanning electron microscope, as well as with polarized and reflected light microscopes. The results from this analysis show a sulfation rim which gets larger with time. Particles extracted at later times show considerable variation in the thickness of their sulfation rims.

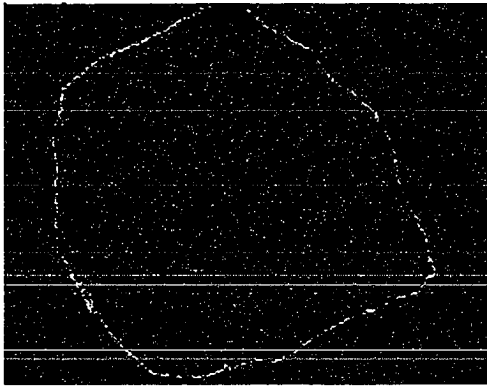
Typically, the particles that have higher magnesium content, i.e. dolomitic particles, have thicker sulfation rims. Some sample sulfur maps of particles reacted for various times are shown in Fig. 6.33.

The irregular shape to the sulfate rims for the 16-minute and 40-minute samples is due to the structure of the limestone. A significant amount of the power plant limestone consists of oolites with diameters of around 0.5 mm. The sulfate tends to diffuse into the cracks between oolites. This structure is believed to be responsible in part for the size distribution of the limestone as shown in Fig. 5.1. The hypothesis being that the particles tend crack preferentially around the size of the oolites. This causes a lack of particles from 0.5 to 1.5 microns in size. The oolitic structure may also account for the pore diffusion control observed in the larger particles as demonstrated in Fig. 6.20. The interfaces between the oolite and the cementing material may act as large pores which do not plug.

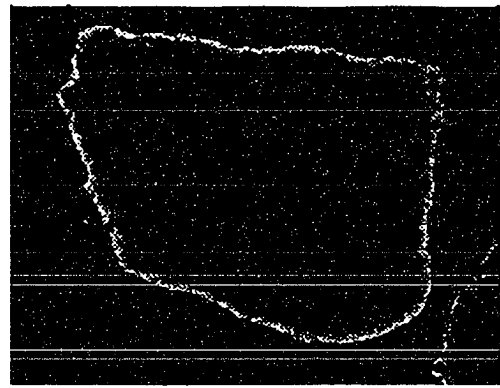
The thickness and profile of the sulfated layers were also determined by microprobe linescans. Particles with layers not affected by oolitic structure were chosen for measurement. Fig. 6.34 shows the results of these linescans. The sulfation layer was seen to have a variety of thicknesses within a given particle, and also between particles of a given sample. In general, however, samples that had been sulfated for longer times showed thicker layers of sulfate.

The linescans show a ratio of sulfur counts to calcium counts. These represent the mass ratio of sulfur to calcium. The counts ratio is not the same as a mass ratio, however. If these values were converted to molar ratios, they would give molar ratios of S/Ca greater than one. The counts ratio is assumed for this analysis to be proportional to the mass ratio, but not equal to it.

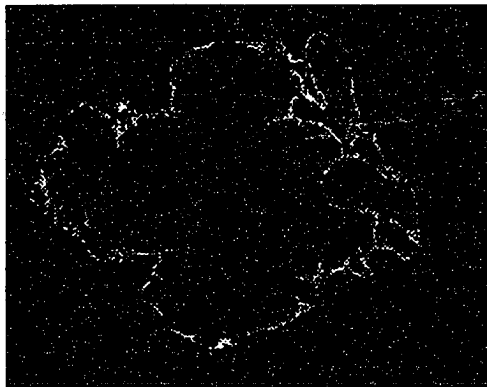
Figure 6.35 shows the relationship between the results of conversion based on transient gas analysis and results computed from the linescans. The solid line is generated



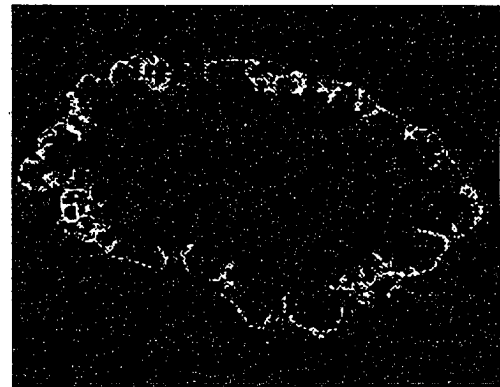
a. Sulfation layer at $t = 2$ min.



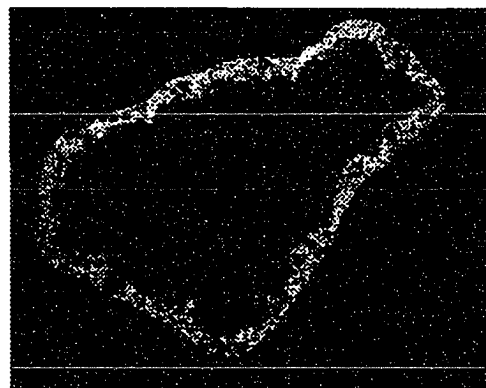
b. Sulfation layer at $t = 8$ min.



c. Sulfation layer at $t = 16$ min.



d. Sulfation layer at $t = 40$ min.



e. Sulfation layer at $t = 80$ min.

Figure 6.33 SEM maps of sulfation at various times in the reaction.

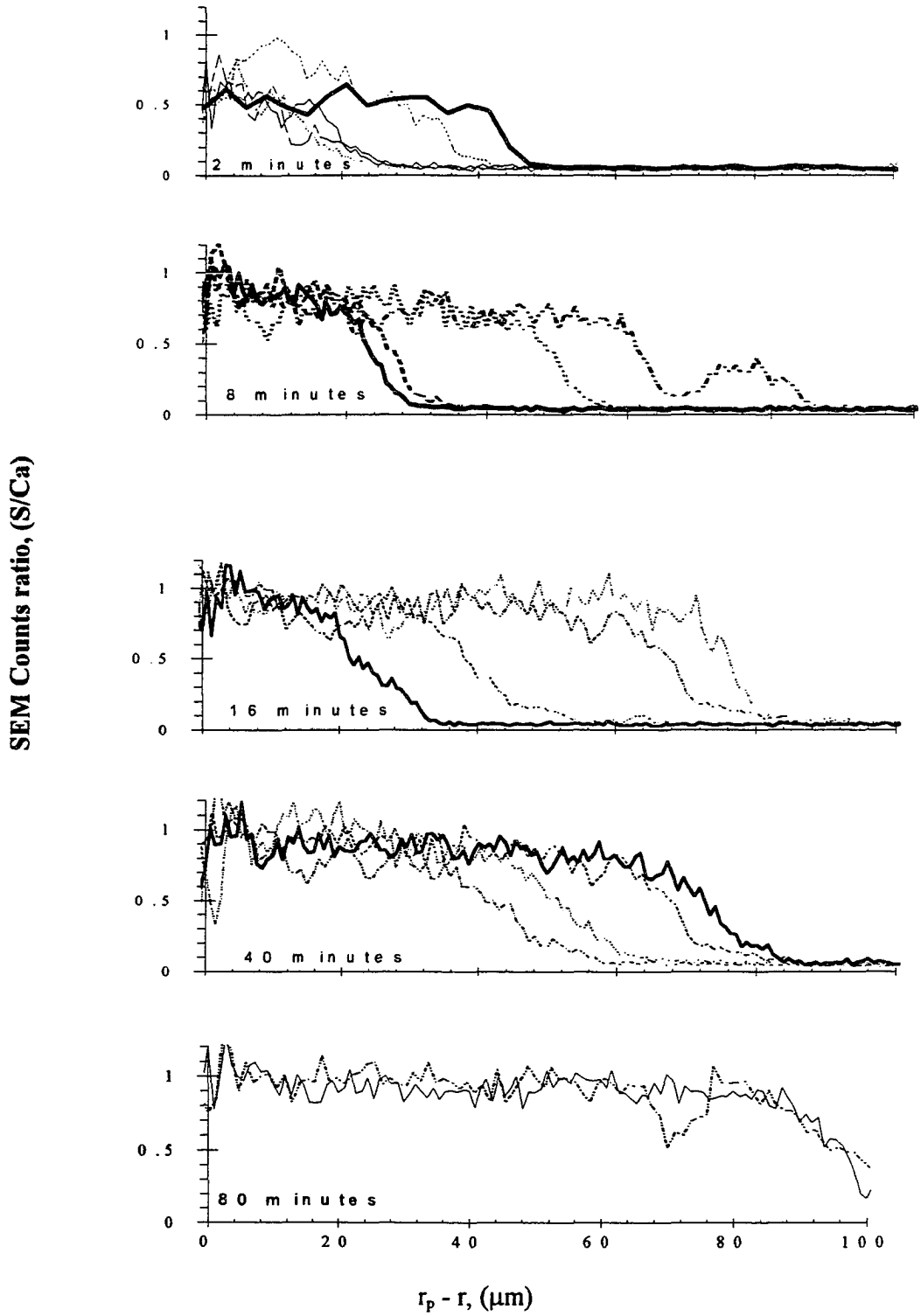


Figure 6.34 Particle linescans at various stages of reaction

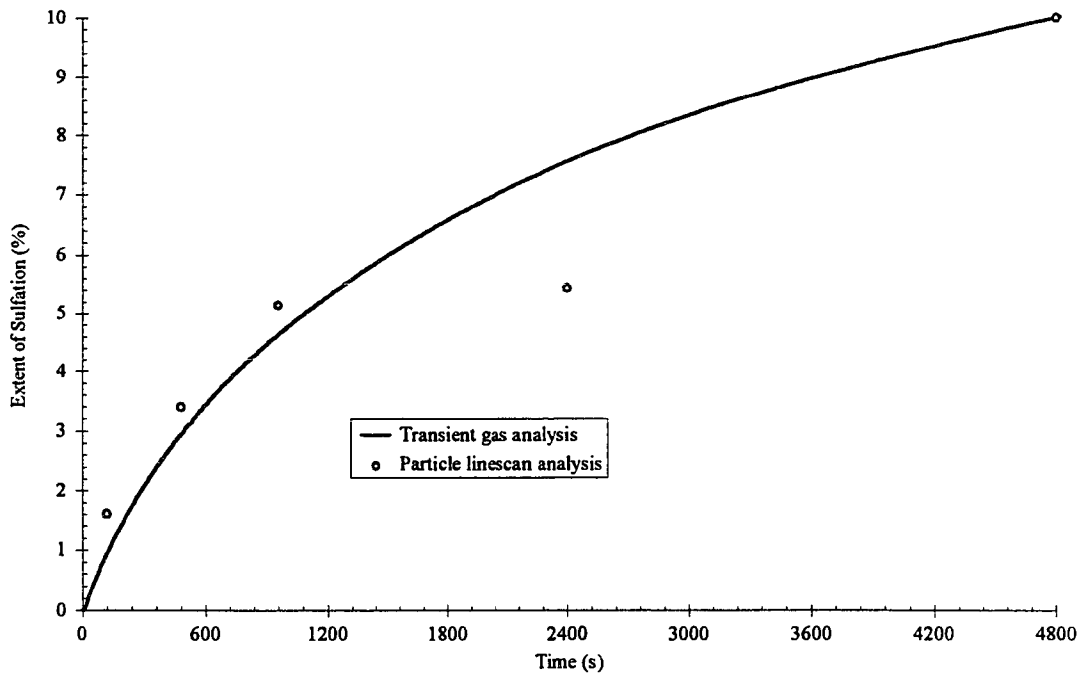


Figure 6.35 Comparison of transient gas analysis with SEM linescan analysis

by integrating the SO_2 transient from time zero at each point in time. The particle analysis conversion is computed by integrating the local conversion from the linescan data as if the particles were spherical particles of 2.58 mm diameter. The value for the linescan conversion at 80 minutes was multiplied by a factor to make it equal to the conversion based on transient gas analysis. The remaining linescan conversion values are multiplied by the same number so that the results are normalized at the 80 minute transient gas analysis conversion value. Using this method the linescan counts ratio would indicate local conversions of only 28% for the 2 minute sample, increasing to 43% for the sample sulfated for 80 minutes. The small sample size from the linescan data did not allow for a very good match between the particle analysis and gas analysis. The results do show a general consistency of shape between the two transients.

6.5 Transient Gas Analysis of Sulfation in Full-Scale Boiler

Several batch tests were run on the ISU power plant boiler, without a great deal of success. CO_2 responses were smaller than previously observed for coal batch tests. A small peak was evident, but then the CO_2 concentration was immediately lost in the background fluctuations. Additionally the data rate for the two transients could not be varied after program initiation. Analysis of calcination would require a faster data rate than was used for sulfation. For these reasons, analysis of calcination was not done on the full scale combustor.

The SO_2 response also suffered from large unsteady fluctuations in the background. Figure 6.36 plots SO_2 vs time for a 100 lb batch of 1.0 mm Gilmore City formation limestone. A background is shown as a straight line, which was determined by averaging the SO_2 readings for the first 20 minutes. The large fluctuations of $\pm 25\%$ of the

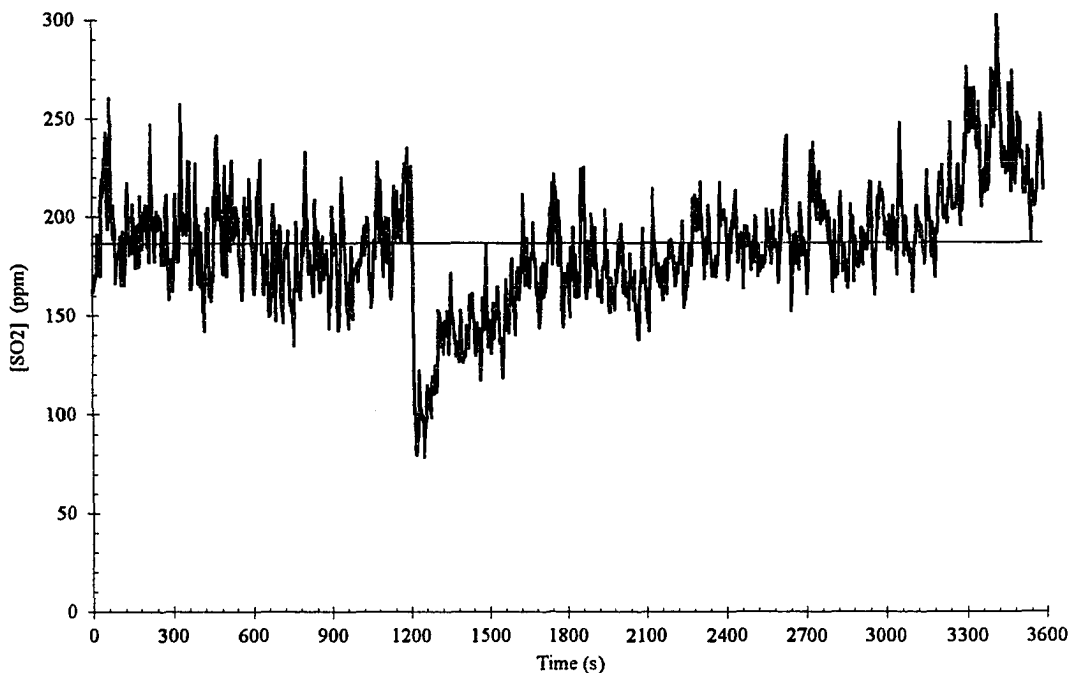


Figure 6.36 SO_2 emissions during limestone batch test ($T = 1120\text{-}1140\text{ K}$, $U_o \approx 4.5\text{ m/s}$, $m_{\text{LS}} = 100\text{ lb}$ Gilmore City formation limestone, $d_p = 1.0\text{ mm}$)

background level are believed to be caused by the unsteady coal feed. The mass of coal is intermittent because drag conveyors in the feed system provide an unsteady release of coal into the feed tubes. The SO_2 released from the coal is believed to follow this irregular pattern. Near the end of the transient there is an unexplained rise in the SO_2 concentration. This type of unpredictable behavior in the transient is common. It is unclear whether any long period changes in the SO_2 background level are occurring over the course of the reaction. A regression of the SO_2 concentration for the first 20 minutes of data results in a downward slope, which makes the increase in SO_2 level at the end of the experiment even less explainable. The results shown in Figure 6.30 represent the best of the experiments run at the power plant.

Figure 6.37 compares the results of full scale boiler testing to a test in the laboratory FBC. The full scale test used 1.00 mm limestone, while the mean size of the limestone in the laboratory FBC was 0.925 mm. The results are similar because the ratio of limestone mass to volumetric air flow between the two cases is similar. The results are

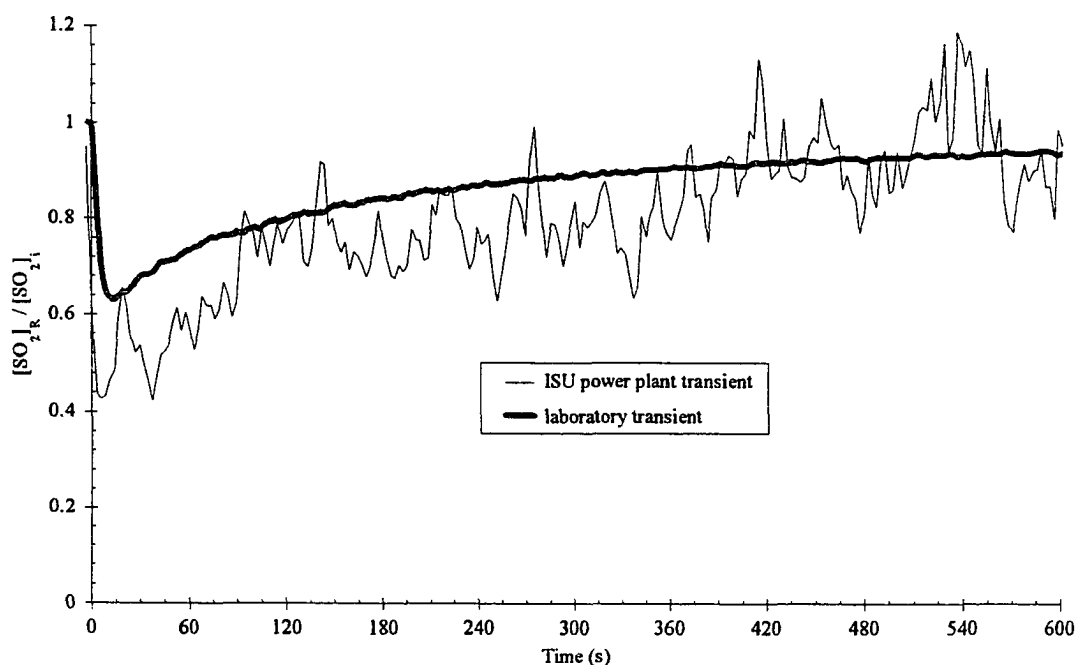


Figure 6.37 Comparison of laboratory and power plant sulfation transients

not expected to correspond exactly since the operating conditions are not the same, and because it may not be valid to model a circulating bed as a CSTR. Figure 6.37 does show, however, that the response of the full scale boiler is similar to that observed in the laboratory.

In Fig. 6.38 the normalized SO_2 difference data is plotted on a log-linear plot to determine sulfation time constants. Results from the full scale boiler seem to straddle the curve from the laboratory experiment for much of the curve. Determination of time constants from the full scale boiler using the slope of its response curve would be difficult. The similarity in the shape of the two transients in Fig. 6.38 indicates that the sulfation process in the full scale boiler may actually be quite similar to that observed in the laboratory FBC.

The shrinking core model developed to analyze the laboratory combustor may also work in modeling the full scale combustor, but several additional considerations

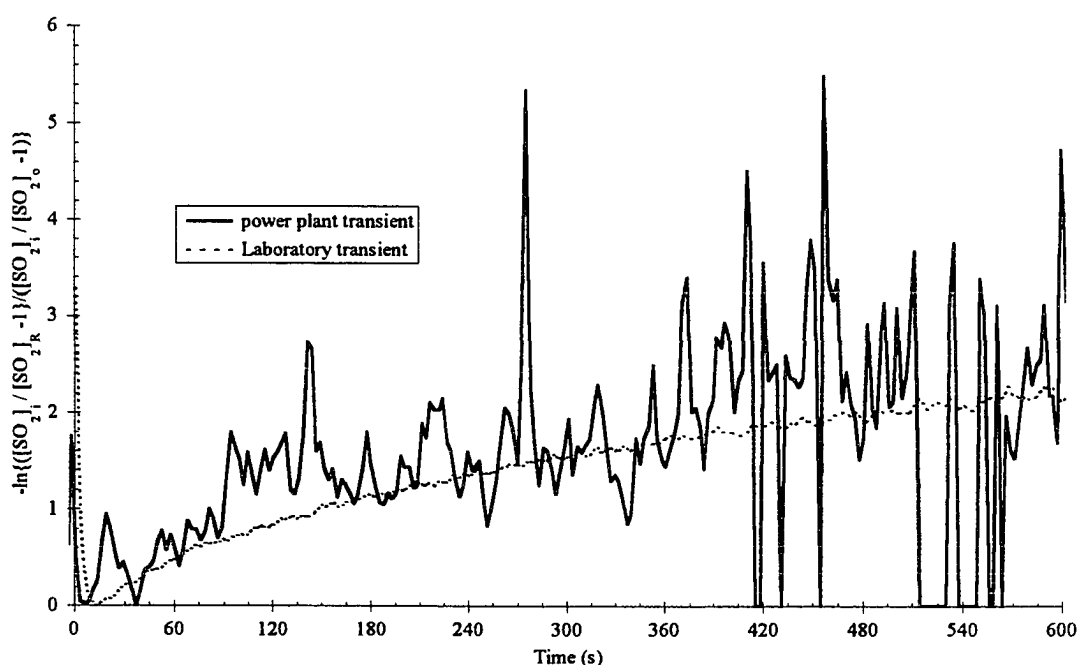


Figure 6.38 Log-linear time constant chart comparing lab and full scale combustors

should be made. The first is that a circulating bed may not behave like a CSTR. Although there is significant mixing of the solid particles, a gradient in $[\text{SO}_2]_R$ along the length of the combustor may be significant. Another consideration is that the use of primary and secondary air results in regions near the bottom of the bed where reducing conditions exist. Calcium sulfide formation may occur instead of CaSO_4 in this region. CaS does not have the high molar volume that CaSO_4 has and may penetrate into the particle. A final consideration is that much of the limestone in the full scale unit is smaller than was analyzed in the lab scale FBC. Thus chemistry control for the early portion of the transient is more likely. More detailed consideration of elutriation and cyclone efficiency is necessary for this analysis. Additionally, a diffuse interface model may be useful for the small particle sizes present in the full-scale boiler.

6.6 Particle Analysis of Particles from Full Scale Boiler

In Fig. 6.39, SEM sulfur maps from power plant bottom ash show a sulfate rim similar to that which was seen in the samples from laboratory experiments. This suggests that the sulfidation reaction is not of major importance in the full scale circulating FBC. Chemical analysis of FBC ash from the ISU physical plant has been conducted by Dawson *et al.* [58] in a study of the feasibility of controlling ash chemical content for further use in cement. Table 6.8 was extracted from that study. This table shows that larger bottom ash particles have a lower percentage of SO_3 , a higher percentage of SiO_2 , and a higher loss on ignition (LOI).

The larger percentage of CaO in the larger particles is balanced to some degree by the increased LOI, which is the weight percent of CO_2 driven off prior to the analysis. The higher LOI gives some evidence of a lower extent of calcination for the larger particles, but its reduction is not as severe as was seen in the laboratory tests. The particle size effect on sulfation, as determined by the fraction of SO_3 , is similar to that observed in

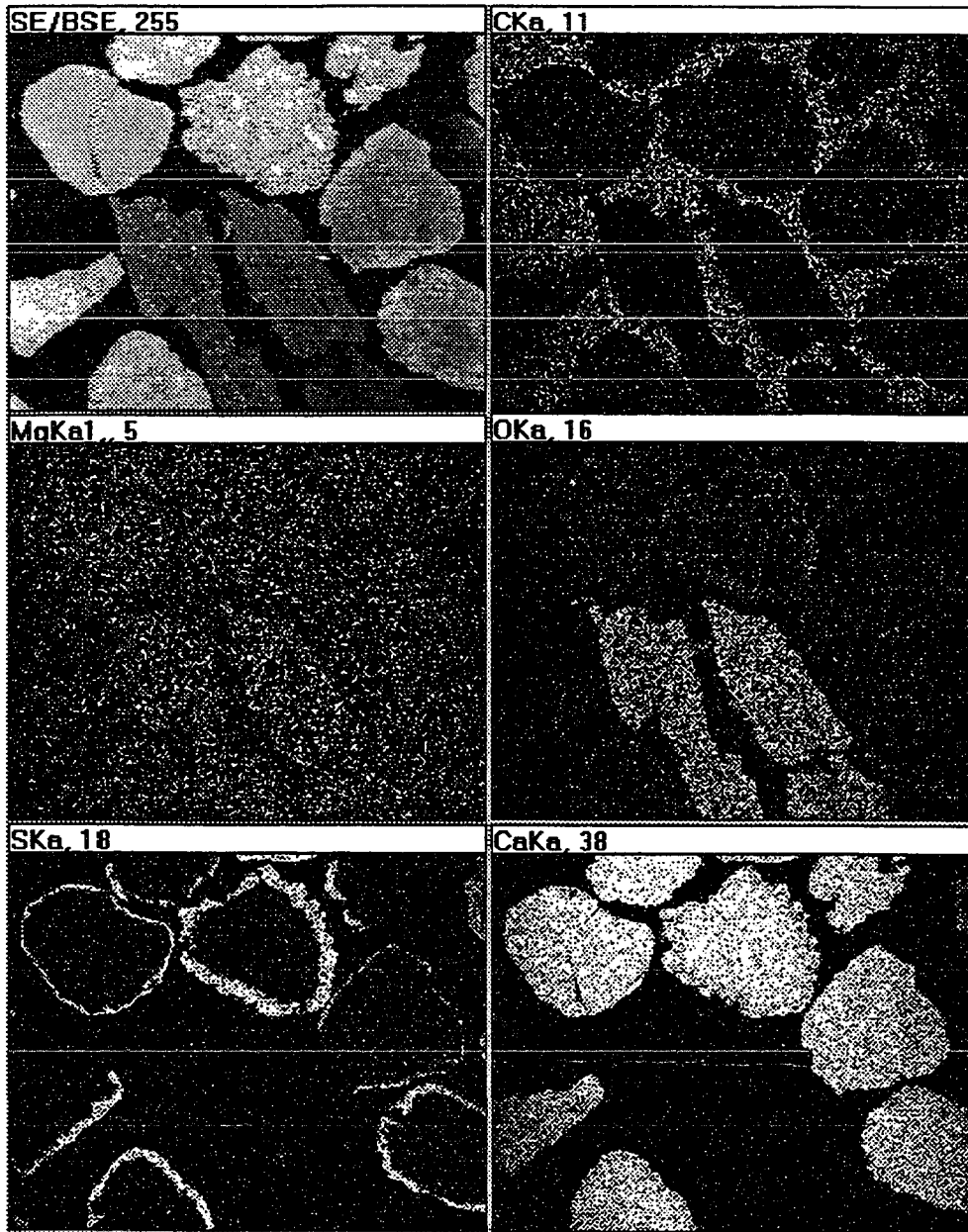


Figure 6.39 SEM component maps of power plant bottom ash showing sulfur rims (lower left map)

Table 6.8 XRF chemical analysis of ISU boiler ash. [58]

	Bag house Ash	Bottom Ash	Bottom Ash (+12)	Bottom Ash (12x20)	Bottom Ash (20x60)	Bottom Ash (60x100)	Bottom Ash (-100)
SiO ₂	33.39	9.83	11.07	11.01	9.73	6.76	7.01
Al ₂ O ₃	15.22	3.01	3.14	3.44	3.01	1.68	2.12
Fe ₂ O ₃	8.21	1.23	1.65	1.36	1.04	1.04	2.08
MgO	0.61	0.50	0.56	0.56	0.46	0.37	0.42
CaO	20.92	58.94	65.58	64.01	57.61	57.20	55.00
Na ₂ O	0.00	0.00	0.27	0.27	0.00	0.19	0.00
K ₂ O	1.56	0.27	0.35	0.39	0.35	0.14	0.06
TiO ₂	0.84	0.17	0.18	0.17	0.14	0.12	0.22
P ₂ O ₅	0.08	0.04	0.05	0.03	0.03	0.03	0.03
SO₃	8.26	27.49	8.58	15.49	30.05	37.16	37.49
SrO	0.08	0.07	0.07	0.07	0.08	0.08	0.08
BaO	0.03	0.00	0.00	0.00	0.00	0.00	0.00
LOI	10.90	3.00	10.00	4.30	1.30	0.60	0.40
Total	100.11	104.54	101.51	101.10	103.81	105.36	104.89

the lab. The probable cause for this is limited penetration of SO₂ into the particle resulting in sulfate rims as seen in the particle maps. The larger particles have a larger unreacted CaO core.

7. CONCLUSIONS

7.1 Calcination

Calcination is largely controlled by the chemical reaction rate. This is demonstrated by the agreement in activation energies with previous literature for chemistry rate controlled calcination. The size dependence for the calcination time constant was greater than one. Size dependence increases as temperature increases. This is shown by reduced activation energies. Particles were tested under isothermal conditions and it is assumed that heat transfer is not limiting in this reaction. However, when a large sample mass is used a greater drop in temperature occurs, and the reaction time is longer. Temperature appears to have little effect on the extent of calcination, except at low temperatures and with large particles. In most cases the extent of calcination was close to 80%.

The chemical reaction rate is a function of the partial pressure and equilibrium partial pressure. This is apparent from the slight change in the calcination time constant with increasing inlet CO₂ concentration. The calcination time constant is inversely proportional to the difference between the equilibrium concentration and the inlet concentration. Calcination is not controlled by film diffusion. Samples reacted at different velocities had little difference in calcination time constants.

The shrinking core model for calcination describes the mechanisms involved in calcination. Although validation of the full scale model needs to be done using a numerical solution, the simplified equations generated by the model help to explain calcination. The use of transient gas analysis is useful to observe how pore diffusion may play a role in calcination of larger particles at higher temperatures. The ability to validate this mechanism in an actual combustion environment is an improvement to existing laboratory procedures.

There are indications of a loss of surface area during the calcination process as suggested by the literature [18-20]. This sintering phenomenon is shown in particle analysis by two distinct CaO rims around some of the particles. Surface area loss may present itself by an increased sulfation reaction rate early in the transient, when the outer edge of the particle is undergoing calcination. Surface area testing shows that at higher temperatures, surface area and pore volume are reduced. The mean pore diameter is greater for Gilmore City formation limestone when calcined at higher temperatures. SEM and reflected light photographs show a possible change in structure over the radius of a particle after reacting for 2 minutes in a 150 gram batch addition of 2.58 mm limestone.

7.2 Sulfation

The sulfation reaction is dependent upon the type of limestone in use and its properties after calcination. The limestone used in this study exhibited a sulfation layer around a shrinking unreacted particle core. Testing in laboratory conditions revealed pore plugging as the dominant controlling mechanism for sulfation of the Gilmore City formation limestone. At early times, however, external mass transfer provided a significant resistance to reaction in the fluidized bed combustor. The reaction was not controlled by the chemical reaction rate at any condition tested in the laboratory scale FBC. This is due in large part to the limitations on particle size that can be examined in the bubbling bed before particles are entrained. Had operating conditions allowed for reaction of smaller particles without elutriation, the chemical reaction resistance may have been more substantial. For larger particles pore plugging is delayed, possibly due to the existence of larger pores and cracks in the larger oolitic particles. Grain-level product layer diffusion resistance was not included in the model that was used in this study. The existence of an unreacted particle core supports the conclusion that pore plugging and not product layer diffusion is the major controlling mechanism.

Temperature did not have a large influence on the extent of sulfation in this study. There may be a small peak in the extent of sulfation at approximately 1123 K, but it is much less pronounced than is reported in the literature [12,56]. Part of this may be the lack of a reducing region in the emulsion phase, as exists in coal combustion [56].

No clear controlling mechanism can be deduced from the relationship between the sulfation time constant and the particle diameter. A power relationship of 1.0 would indicate chemistry control and a larger value may indicate pore diffusion control. The value of 0.28 for the power relationship indicates that pore-plugging, film diffusion and bulk mass transfer all may contribute to the reaction resistance early in the reaction. Activation energy analysis for early times supports film diffusion, bulk mass transfer, and pore plugging as possible significant resistances early in the reaction.

Analysis of two other limestones showed a better sulfation performance for the Cedar Bay #1 limestone when compared to the Gilmore City limestone and a considerably worse performance for the Nova Scotia limestone. The reduction in the extent of sulfation for the Nova Scotia limestone was more than could be accounted for by the smaller amount of CaCO_3 in its chemistry. The reduction in performance for this high SiO_2 content limestone is in contradiction to the findings of Mulligan *et al.* [6] and Dam-Johansen and Ostergaard [2].

Overall, modeling sulfation as a shrinking core with decaying diffusivity well describes the results seen in the laboratory. The model can be fit with reasonable values for effective diffusivity and chemical reaction rate constant to effectively simulate the gas transient which results from a batch test. Moreover, simplifications of the model show that transient gas analysis is an effective means for determining the controlling mechanism in sulfation and for characterizing the reaction.

7.3 Full Scale Testing

Full scale tests at the Iowa State University (ISU) power plant highlight the difficulties in using transient gas analysis at full scale units, but show similarities to the results obtained in the lab. The large fluctuations associated with the coal feed system makes obtaining a steady background concentration extremely difficult. Interpretation in the midst of large fluctuations is also unreliable when analyzing time-series data.

Spectral analysis was not used in the analysis as had been hoped for two reasons. The non-linear nature of the sulfation reaction does not allow for interpretation of the frequency plots. Furthermore, the large amount of correlated noise masks the signals of interest. It is hoped that some method similar to spectral analysis can be developed to characterize sorbent reactions. The use of time series data developed from batch tests does lend itself to use in the full scale, however.

7.4 Suggestions for Future Tests

In the laboratory setting, much of the work has been completed. There are some limitations due to operating conditions required for combustion. For example, film diffusion control seems inevitable for early times in the reactor because of elutriation of small particles at higher velocities. Much could be learned from testing of a larger variety of limestones than has been considered. It is clear that some limestones behave quite differently and modeling could be done more generally. The current model for sulfation should work well for compact limestone of an older geological age. The shrinking core model may not work well with highly porous limestones and chalks because of a significant reaction zone. Incorporation of a three zone model into the current method may be useful.

A more complete series of tests comparing lime and limestone batch additions may provide a better understanding of the important features of calcination and sintering. Also

the effect of SO₂ on calcination is yet undetermined.

Much remains to be done in the area of full-scale testing. The biggest problem is the difficulty in getting a steady baseline SO₂ signal. Full scale units with smoother operating coal feed systems may be an alternative. Instrumentation of the full scale unit was inadequate. The gas analysis equipment was of outstanding quality, but boiler parameters needed for full scale modeling, such as bed density, are not available on the full scale unit used in this study.

APPENDIX: PROGRAM CODE

1. CALCINE.f

*
 * CALCINE.F is a program to operate the full model calcination
 * shrinking particle core. It uses a numerical integrator from the NAG
 * library resident on Project Vincent at Iowa State Univeristy.
 * The routine d02eaf is found in the NAG lrary that is
 * resident on the Vincent work stations. For further help
 * on how to use the subroutine 'add nag' on Vincent and then
 * type 'naghelp'. Further documentation may be found in
 * room 191 Durham.

* This simulation models the limestone calcination process in
 * batch tests in a laboratory fluidized bed.

* COMPUTATIONAL PARAMETERS

* Declare variables used as double precision
 implicit double precision (a-h, o-z)
 * Declare primary integers
 integer neq, iw
 * Specify working parameters (neq = number of equations)
 parameter (neq=6,iw=(12+neq)*neq+50)
 * Declare secondary integers and arrays
 integer ifail, istep
 dimension y(neq+1),w(iw)
 * Declare external routines and common variables
 external d02eaf, fcn
 common dp, TK, CO2E, CO2i, corr

* VARIABLE DEFINITION

* y(1) = CO2 concentration in bed (mol/m³)
 * y(2) = CO2 concentration at particle surface (mol/m³)
 * y(3) = CO2 concentration at CO2 reaction core (mol/m³)
 * y(4) = radius of particle core
 * y(5) = CO2 concentration at CO2 instrument(mol/m³)

* Initial values of variables
 CO2i=8.510d0
 * Temperature (deg F)
 TF=1562.0d0
 * Temperature (K)

```

TK=(TF+459.67)*5.0d0/9.0d0
* Equilibrium CO2 concentration
  CO2E=10**(-8308.0d0/TK+7.079d0)/(.00008205*TK)
* Correction factor for instrument temperature and water vapor
* removal and change of units from mole fraction
  corr=1.0d-2*(1/1+1.0d-2*CO2i)*1/.00008205/TK

```

```

dp = 550.0d-6
y(1) = CO2i*corr
y(2) = y(1)
y(3) = y(2)
y(4) = dp/2.0d0*.99999d0
y(5) = y(1)
y(6) = y(1)
y(7) = y(1)

```

```

i = 0
time = 2.0d0

```

```

* tolerance of integration
  tol = 1.0d-35

```

```

*
* -----
* CREATING OUTPUT FILES AND FORMAT
*
* -----

```

```

  open (unit=10, name='cal550.out', status='unknown')

```

```

* START OF ITERATION
*
* -----

```

```

  ifail = 0
  do istep = 1,1000
  tend = 2.0d0+dfloat(istep)/20.0d0

```

```

* CALLING INTEGRATION SUBROUTINE
*
* -----

```

```

  call d02eaf(time,tend,neq,y,tol,fcn,w,iw,ifail)

```

```

* Write to file and screen every 20th step

```

```

  i = i + 1
  if (i.eq.20) then
    i = 0

```

```

* Send data to output
  write (10,99998)time,y(5)/corr,y(1)/corr,y(3)/corr,y(4)

```

```

write (*,99998)time,y(5)/corr,y(1)/corr,y(3)/corr,y(4)
endif

```

```

end do

```

```

close unit=10

```

```

99998 format (1x,f7.1,'e12.5','e12.5','e12.5','e12.5)

```

```

10 stop
end

```

```

*
* -----
* Subroutine fcn is called by d02eaf internally. This routine
* contains the system of differential equations to be integrated
  subroutine fcn(time,y,f)
  implicit double precision (a-h, o-z)
  integer neq
  parameter (neq=6)
  dimension y(neq+1), f(neq)
* Declare common variables
  common dp, TK, CO2E, CO2i, corr
*

```

```

* Pi
  pi = 3.14159d0
*

```

```

* PARAMETERS
*

```

```

* THERMODYNAMIC PARAMETERS

```

```

* Air inlet temperature
  Tin=300.0d0
* Air density
  rhoair= .30354d0*1123.0d0/TK
* Air viscosity (kg/m/s)
  vmuair= 449.0d-7*(TK/1100.0d0)**0.5
* Air flow (scfm inlet temp)
  Qairfm=18.2
* Air flow (m^3/s at temp.)
  QairmT=Qairfm*0.3048**3/60*1.1614/rhoair
*

```

```

* BED PARAMETERS

```

```

* Bed depth (m)
  bl = 0.1524d0
* Bed diameter (m)

```

```

    dbed = 0.2032d0
*   Bed area
    abed = pi*dbed**2/4.0d0
*   Bed volume
    vbed = bl*abed
*   Superficial bed velocity (m/s)
    u = QairmsT/abed*1.054d0
*   Intrinsic bed parameter (1/s)
    cbed = u/bl
*   Bubble void
    vb = 0.75d0
*


---


*   LIMESTONE PARAMETERS
*   Limestoned mass (g)
    sm = 30.0d0
*   Limestone density
    rhol = 2700.0d3
*   Number of limestone particles
    pnum = sm/(pi*dp**3/6.0d0*rhol)
*   Particle volume
    vpar = pi*dp**3/6.0d0
*   Particle external area
    ap = pi*dp**2
*   Particle area at CaCO3 radius
    acs = 4.0d0*pi*(y(4)**2)
*


---


*   FILM MASS TRANSFER COEFFICIENT (m/s)
    Re=rhoair*dp*u/vmuair
    Db=2.0d-4
    Sc=vmuair/rhoair/Db
*   Froessling correlation
    Sh=2.0d0+0.6d0*Sc**(1.0d0/3.0d0)*Re**(0.5d0)
*   LaNauze correlation
    Sh=2.0d0*vb+0.69d0*Sc**(1.0d0/3.0d0)*Re**(0.5d0)
    hc=Sh*Db/dp
*


---


*   REACTION RATE COEFFICIENT (m/s)
*   Calcination (m/s)
    rc = 1.05d-1
*


---


*   EFFECTIVE DIFFUSIVITY OF CO2 (m^2/s)
    deffc = 1.4d-4
*


---



```

* VOLUMES IN DIFFERENTIAL EQUATIONS (ARTIFACTS)

$$vl=pi/6.0d0*(dp**3-2.0d0*y(4)**3)$$

$$vl=pi*dp**2*1.0d-6$$

$$vf=pi*dp**2*dp/100.0d0$$

*

* SAMPLING SYSTEM PARAMETERS

$$taui = 3.0d0$$

*

* DIFFERENTIAL EQUATIONS

*

* MODEL EQUATIONS

$$f(1) = cbed*(CO2i*corr - y(1)) - hc*ap*pnum/vbed*(y(1)-y(2))$$

$$f(2) = hc*ap/vf*(y(1)-y(2)) - 4.0d0*pi*deffc/$$

$$\& (1/y(4)-2.0d0/dp)/vf*(y(2) - y(3))$$

$$f(3) = 4.0d0*pi*deffc/(1.0d0/y(4)-2.0d0/dp)/vl$$

$$\& *(y(2) - y(3)) + rc*acs/vl*(CO2E-y(3))$$

$$f(4) = -rc*100.0d0/rhol*(CO2E-y(3))$$

* SAMPLING SYSTEM

$$f(5) = 1.0d0/taui*(y(1)-y(5))$$

*

return

end

2. SULFATE.f

*
*
* SULFATE.f is a program to operate the full sulfation shrinking
* particle core with exponentially decaying diffusivity
* model. It uses a numerical integrator from the NAG
* library resident on Project Vincent at Iowa State Univeristy.
* The routine d02eaf is found in the NAG linary that is
* resident on the Vincent work stations. For further help
* on how to use the subroutine 'add nag' on Vincent and then
* type 'naghelp'. Further documentation may be found in
* room 191 Durham.

* This simulation models the limestone sulfation process in
* batch tests in a laboratory fluidized bed.

* COMPUTATIONAL PARAMETERS

* Declare variables used as double precision
 implicit double precision (a-h, o-z)
* Declare primary integers
 integer neq, iw
* Specify working parameters (neq = number of equations)
 parameter (neq=6,iw=(12+neq)*neq+50)
* Declare secondary integers and arrays
 integer ifail, istep
 dimension y(neq+1),w(iw)
* Declare external routines and common variables
 external d02eaf, fcn
 common dp

* VARIABLE DEFINITION

* y(1) = SO2 concentration in bed (mol/m³)
* y(2) = SO2 concentration at particle surface (mol/m³)
* y(3) = SO2 concentration at SO2 reaction core (mol/m³)
* y(4) = radius of particle core
* y(5) = SO2 conc. of stuck portion of sampling system(mol/m³)
* y(6) = SO2 conc. of clear portion of sampling system (mol/m³)
* y(7) = SO2 conc. at SO2 instrument

* Initial values of variables

```

dp = 925.0d-6
y(1) = 1520.1d0*1.004d-5
y(2) = 0.0d0
y(3) = 0.0d0
y(4) = dp/2.0d0*.99999d0
y(5) = y(1)
y(6) = y(1)
y(7) = y(1)

```

```

i = 0
time = 5.0d0

```

```

* tolerance of integration
  tol = 1.0d-35

```

```

*

```

```

*

```

```

* CREATING OUTPUT FILES AND FORMAT

```

```

*

```

```

*

```

```

open (unit=10, name='sred1820.out', status='unknown')
write (10,99998) time,y(1)/1.004d-5,y(7)/1.004d-5,y(3),y(4)
write (*,99998) time,y(1)/1.004d-5,y(7)/1.004d-5,y(3),y(4)

```

```

*

```

```

*

```

```

* START OF ITERATION

```

```

*

```

```

*

```

```

ifail = 0
do istep = 1,3000
* Subdividing step for initial integration time
  if (istep.le.2000) then
    tend = 5.0d0+dfloat(istep)/20.0d0
  else
    tend = 5.0d0+100.0d0 + dfloat(istep-2000)*3.0d0
  endif

```

```

*

```

```

*

```

```

* CALLING INTEGRATION SUBROUTINE

```

```

*

```

```

call d02eaf(time,tend,neq,y,tol,fcn,w,iw,ifail)

```

```

* Write to file and screen every 20th step

```

```

i = i + 1
if (i.eq.20) then

```

```

      i = 0
*   Send data to output
      write (10,99998)time,y(1)/1.004d-5,y(7)/1.004d-5,y(3),y(4)
      write (*,99998)time,y(1)/1.004d-5,y(7)/1.004d-5,y(3),y(4)
      endif
      end do
      close unit=10

```

```

99998 format (1x,f7.1,'e12.5','e12.5','e12.5','e12.5)

```

```

      stop
      end

```

```

*

```

```

*

```

```

*   Subroutine fcn is called by d02eaf internally. This routine
*   contains the system of differential equations to be integrated

```

```

      subroutine fcn(time,y,f)
      implicit double precision (a-h, o-z)
      integer neq
      parameter (neq=6)
      dimension y(neq+1), f(neq)

```

```

*   Declare common variables
      common dp

```

```

*

```

```

*

```

```

*   Pi

```

```

      pi = 3.14159d0

```

```

*

```

```

*

```

```

*   PARAMETERS

```

```

*

```

```

*

```

```

*   THERMODYNAMIC PARAMETERS

```

```

*   Temperature (deg F)

```

```

      TF=1550.0d0

```

```

*   Temperature (K)

```

```

      TK=(TF+459.67)*5.0d0/9.0d0

```

```

*   Air inlet temperature

```

```

      Tin=300.0d0

```

```

*   Air density

```

```

      rhoair= .30354d0*1123.0d0/TK

```

```

*   Air viscosity (kg/m/s)

```

```

      vmuair= 449.0d-7*(TK/1100.0d0)**0.5

```

```

*   Air flow (scfm inlet temp)

```

```

      Qairfm=18.21

```

```

* Air flow (m^3/s at temp.)
  QairmsT=Qairfm*0.3048**3/60*1.1614/rhoair
*
*
* FILM MASS TRANSFER COEFFICIENT (m/s)
  Re=rhoair*dp*u/vmuair
  Db=1.4d-4
  Sc=vmuair/rhoair/Db
* Froessling correlation
* Sh=2.0d0+0.6d0*Sc**(1.0d0/3.0d0)*Re**(0.5d0)
* LaNauze correlation
  Sh=2.0d0*vb+0.69d0*Sc**(1.0d0/3.0d0)*Re**(0.5d0)
  hs=Sh*Db/dp
*
*
* REACTION RATE COEFFICIENT (m/s)
* Sulfation (m/s)
  rs = 1.9d2
*
*
* EFFECTIVE DIFFUSIVITY OF SO2 (m^2/s)
  deffs = 1.7d-6*dexp(-time/(760.0d0))
*
*
* SO2 INLET CONCENTRATION (mol/m^3)
* Straight line adjustment to background from [SO2]i, 0 to end
  SO2ii = 1520.12d0
  SO2if = 1529.04d0
  timef = 3300.0d0
  SO2i = 1.004d-5*(SO2ii+time/timef*(SO2if-SO2ii))
*
*
* BED PARAMETERS
* Bed depth (m)
  bl = 0.1524d0
* Bed diameter (m)
  dbed = 0.2032d0
* Bed area
  abed = pi*dbed**2/4.0d0
* Bed volume
  vbed = bl*abed
*
* Superficial bed velocity (m/s)
  u = QairmsT/abed*1.054d0

```

* Intrinsic bed parameter (1/s)

$$cbed = u/bl$$

* Bubble void

$$vb = 0.75d0$$

*

*

* LIMESTONE PARAMETERS

* Limestoned mass (g)

$$sm = 20.0d0$$

* Limestone density

$$rhol = 2700.0d3$$

* Number of limestone particles

$$pnum = sm/(pi*dp**3/6.0d0*rhol)$$

* Particle volume

$$vpar = pi*dp**3/6.0d0$$

* Particle external area

$$ap = pi*dp**2$$

* Particle area at CaO radius

$$acs = 4.0d0*pi*(y(4)**2)$$

*

*

* VOLUMES IN DIFFERENTIAL EQUATIONS (ARTIFACTS)

$$vl=pi/6.0d0*(dp**3-2.0d0*y(4)**3)$$

$$vl=pi*dp**2*1.0d-6$$

$$vf=pi*dp**2*dp/100.0d0$$

*

*

* SAMPLING SYSTEM PARAMETERS

$$frstk = 0.04d0$$

$$frclr = 1-frstk$$

$$taustk = 200.0d0$$

$$tauclr = 6.5d0$$

*

*

* DIFFERENTIAL EQUATIONS

*

* MODEL EQUATIONS

$$f(1) = cbed*(SO2i - y(1)) - hs*ap*pnum/vbed*(y(1)-y(2))$$

$$f(2) = hs*ap/vf*(y(1)-y(2)) - 4.0d0*pi*deffs/$$

$$\& (1/y(4)-2.0d0/dp)/vf*(y(2) - y(3))$$

$$f(3) = 4.0d0*pi*deffs/(1.0d0/y(4)-2.0d0/dp)/vl$$

$$\& *(y(2) - y(3)) - rs*acs/vl*y(3)$$

$$f(4) = -rs*56.0d0/(0.56d0*rhol)*y(3)$$

*

SAMPLING SYSTEM

$$f(5) = 1.0d0/taustk*(y(1)-y(5))$$

$$f(6) = 1.0d0/taucrlr*(y(1)-y(6))$$

$$y(7) = frstk*y(5)+frclr*y(6)$$

*

return
end

REFERENCES

- 1 Cooper, C. D. and Alley, F. C., Air pollution control: A design approach, Waveland Press, Prospect Heights, IL, 1994.
- 2 Dam-Johansen, K. and Ostergaard, K., *Chem. Eng. Sci.*, **46**, No. 3, 827-837, 1991.
- 3 Dixon, D., The practical geologist, Quarto, New York, 104, 1992.
- 4 Trudgill, S., Limestone geomorphology, Longman, New York, 8-9, 1985.
- 5 Borgwardt, R. H. and Harvey, R. D., *Env. Sci. and Tech.* **6**, No. 4., 350-360, 1972.
- 6 Mulligan, T., Pomeroy, M. and Bannard, J. E., *Journal of the Inst. of Energy* **62**, 40-47, 1989.
- 7 Carello, S. A. and Vilila, A. C. F., *Ind. Eng. Chem. Res.*, **32**, 3135-3142, 1993.
- 8 Desai, N. J. and Yang, R. T., *Ind. Eng. Chem. Process Des. Dev.*, **22**, 119-123.
- 9 Potter, A. E., *Ceram. Bull.* **48**, 855-858.
- 10 Khraisha, Y. H. and Dugwell, D. R., *Chem. Eng. Res. and Des.*, **67**, 52-58, 1989.
- 11 Hills, A. W. D., *Chem. Eng. Sci.*, **23**, 297, 1968.
- 12 Dennis, J. S. and Hayhurst, A. N., *Proceedings of the Fifth Engineering Foundation Conference on Fluidization*, Elsinore, Denmark, K. Ostergaard and A. Sorensen, Ed. 1986.
- 13 Christofides, N. J., Ph. D. dissertation, Iowa State University, 1993.
- 14 Ingraham, T. R. and Marier, P., *Can. Journal of Chem. Eng.*, **41**, 170, 1963,
- 15 Rajeswara Rao, T., Gunn, D. J. and Bowen, J. H., *Chem. Eng. Res. and Des.*, **67**, 38-47, 1989.
- 16 Prater, C. D., *Chem. Eng. Sci.*, **8**, 284, 1958.
- 17 Turkdogan, E. J., Physical chemistry of high temperature technology, Academic, New York (1980).

18. Milne, C. R., Silcox, G. D., Pershing, D. W. and Kirchgessner, D. A., *Ind. Eng. Chem. Res.* **29**, 144, 1990.
19. Mai, M. C. and Edgar, T. F., *AIChE Journal* **35**, No. 1, 34-35, 1989.
20. Stouffer, M. R. and Yoon, H., *AIChE Journal* **35**, No. 8, 1253-1262, 1989.
21. Borgwardt, R. H., EPA Paper AEERL-P-398; Air and Energy Engineering Research Laboratory, U.S. Environmental Protection Agency: Research Triangle Park, NC, May 3, 1988.
22. Dam-Johansen, K. and Ostergaard, K., *Chem. Eng. Sci.*, **46**, No. 3, 839-845, 1991.
23. Dam-Johansen, K. and Ostergaard, K., *Chem. Eng. Sci.*, **46**, No. 3, 855, 1991.
24. Bhatia, S. K. and Perlmutter, D. D., *AIChE Journal*, **27**, 2, 1981.
25. Hsia, C., St. Pierre, G. R., Raghunathan, K. and Fan, L.-S., *AIChE Journal*, **39**, No. 4, 698-700, 1993.
26. Hsia, C., St. Pierre, G. R. and Fan, L. -S., *AIChE Journal*, **41**, No. 10, 2337-2340, 1995.
27. Bradley, B. and Doraiswamy, L. K., Modeling of gas-solid reactions, unpublished notes, 1993.
28. Yagi, S. and Kunii, D., *5th Symposium (International) on Combustion*, Reinhold, New York, 231, 1955
29. Levenspiel, O., *Chemical reaction engineering*, John Wiley and Sons, New York, 361-377. 1972.
30. Ishida, M. and Wen, D. Y., *AIChE Journal*, **14**, 311, 1968.
31. Mantri, V. B., Gokarn, A. N., and Doraiswamy, L. K., *Chem. Eng. Sci.*, **31**, 779-785, 1976.
32. Bowen, J. H., Khan, A. R. and Mutasher, E. I., *Chem. Eng. Res. Des.*, **67**, 58-65, 1989.
33. Bowen, J. H. and Cheng, C. K., *Chem. Eng. Sci.*, **24**, 1829-1831, 1969.
34. Khan, A. R. and Bowen, J. H., *Chem. Eng. Res. Des.*, **70**, 265-275, 1992.
35. Szekely, J. and Evan, J. W., *Chem. Eng. Sci.*, **25**, 1091-1107, 1970.

36. Hartman, M. and Coughlin, R. W., *AIChE Journal*, **22**, No. 3, 490-498, 1976.
37. Dam-Johansen, K., Hansen, P. F. B. and Ostergaard, K., *Chem. Eng. Sci.* **46**, 847-853, 1991.
38. Heesink, A. B. M., Prins, W. and van Swaaij, W. P. M., *Chem. Eng. Journal*, **53**, 25-37, 1993.
38. Heesink, A. B. M., Prins, W., and van Swaaij, W. P. M., *Chem. Eng. Journal*, **53**, 25-37, 1993.
39. Georgakis, C., Chang, C. W. and Szekeley, J., *Chem. Eng. Sci.* **34**, 1072-1075, 1979.
40. Sotirchos, S. V. and Zarkanitis, S., *Chem. Eng. Sci.*, **48**, No. 8, 1487-1502, 1993.
41. Sotirchos, S. V. and Zarkanitis, S., *AIChE Journal*, **38**, No. 10, 1536-1550, 1992.
42. Zheng, J., Yates, J. G., Rowe, J. G., *Chem. Eng. Sci.*, **37**, No. 2, 167-174, 1985.
43. Basu, P., Greenblatt, J., Wu, S. and Briggs, D., *10th International Conference on Fluidized Bed Combustion*, San Francisco, CA, 1989.
44. Baker, E. H., *Journal Chem. Soc.*, 464. 1962.
45. Christofides, N., and Brown, R.C. *Tenth Annual International Pittsburgh Coal Conference*, Pittsburgh, PA, 1993.
46. Miller, D., O'Donnel, J. and Tomberlin, G., *10th International Conference on Fluidized Bed Combustion*, San Francisco, CA, 1989.
47. Raines, T. S., PhD dissertation, Iowa State University, 1996.
48. Borgwardt, R. H., *Env. Science Tech.*, **4**, 59, 1970.
49. Froessling, N., *Gerland Beitr. Geophys.*, **52**, 170, (1938)
50. La Nauze, R. D., *Fluidization (2nd Ed.)*, Academic Press, London, 1985, pp. 648-674.
51. Kennedy, J. B. and Neville, A. M., *Basic statistical methods for engineers and scientists*, Harper and Row, New York, 1976.
52. Doraiswamy, L. K., *Heterogeneous reactions: Analysis, examples, and reactor design*, Wiley, New York, 143, 1984.

53. Powell, E. K. and Searcy, A. W., *Metallurgical Transactions*, **11B**, 427, 1980.
54. Khraisha, Y. H. and Dugwell, D. R., *Chem. Eng. Res. and Des.*, **67**, 48-51, 1989.
55. Colakyan, M. and Levenspiel, O., *Powder Technology*, **38**, 223, 1984.
56. Lyngfelt, A. and Leckner, B., *Journal of the Inst. of Energy*, **62**, 62-72, 1989.
57. Wen, C. Y. and Ishida, M., *Env. Sci. Tech.*, **7**, 703, 1973.
58. Dawson, M. R., Chriswell, C. D., Smeenk, J., Buttermore, W. H., O'Donnell, J. A., and Gensch, A. C., "Controlling the chemical composition of bag house ash from a circulating fluidized bed boiler for use in cement," submitted to *Fuel*.